UNESP – UNIVERSIDADE ESTADUAL PAULISTA “Júlio de Mesquita Filho”
CAMPUS DE ARARAQUARA
PROGRAMA DE PÓS-GRADUAÇÃO EM QUÍMICA

Andressa Trentin

PhD Thesis

Structure and electrochemical properties of PMMA-silica hybrid coatings modified with cerium and lithium ions

Araraquara
2019

ANDRESSA TRENTIN

Structure and electrochemical properties of PMMA-silica hybrid coatings modified with cerium and lithium ions

Thesis in a Joint PhD submitted in fulfillment of the requirements for the degree of Doctor in Chemistry

Supervisors: Prof. Dr. Peter Hammer
Prof. Dr. ir. Tom Hauffman

Araraquara
2019

FICHA CATALOGRÁFICA

T795s

Trentin, Andressa
Structure and electrochemical properties of PMMA-silica hybrid coatings modified with cerium and lithium / Andressa Trentin. – Araraquara : [s.n], 2019
127 f. : il.

Thesis (doctor) – Universidade Estadual Paulista, Instituto de Química
Advisor: Peter Hammer
Co-advisor: Tom Hauffman

1. Protective coatings. 2. Nanocomposites (Materials). 3. Sol-gel process. 4. Corrosion and anticorrosives. 5. Electrochemistry. I. Título.

Bibliotecária Responsável: Valéria Aparecida Moreira Novelli - CRB/8

UNIVERSIDADE ESTADUAL PAULISTA

Câmpus de Araraquara

CERTIFICADO DE APROVAÇÃO

TÍTULO DA TESE: "Structure and electrochemical properties of PMMA-silica hybrid coatings modified with cerium and lithium ions"

AUTORA: ANDRESSA TRENTIN
ORIENTADOR: PETER HAMMER

Aprovada como parte das exigências para obtenção do Título de Doutora em QUÍMICA, pela Comissão Examinadora:

Prof. Dr. PETER HAMMER
Departamento de Físico-Química / Instituto de Química - UNESP - Araraquara

Prof. Dr. TOM HAUFFMAN
Departamento de Materiais e Química / Vrije Universiteit Brussel - VUB - Bruxelas

Prof. Dr. GERMANO TREMILIOSI FILHO
Departamento de Físico-Quimica / Universidade de São Paulo - USP - São Carlos

Profª. Drª. MARIE GEORGES OLIVIER
Departamento de Clência dos Materiais / Université de Mons - UMONS - Mons

Prof. Dr. DANNY VAN HEMELRIJCK
Mechanics of Materials and Constructions (MeMC) / Vrije Universiteit Brussel – VUB - Bruxelas

Prof. Dr. ASSIS VICENTE BENEDETTI
Departamento de Físico-Química / Instituto de Química - UNESP - Araraquara

Dr. BENNY WOUTERS
Departamento de Materiais e Química / Vrije Universiteit Brussel - VUB - Bruxelas

Araraquara, 08 de outubro de 2019

UNIVERSIDADE ESTADUAL PAULISTA

Câmpus de Araraquara

CERTIFICADO DE APROVAÇÃO

TÍTULO DA TESE: "Structure and electrochemical properties of PMMA-silica hybrid coatings modified with cerium and lithium ions"

AUTORA: ANDRESSA TRENTIN
ORIENTADOR: PETER HAMMER

Aprovada como parte das exigências para obtenção do Título de Doutora em QUÍMICA, pela Comissão Examinadora:

Prof. Dr. PETER HAMMER
Departamento de Físico-Química / Instituto de Química - UNESP - Araraquara

Prof. Dr. TOM HAUFFMAN
Departamento de Materiais e Química / Vrije Universiteit Brussel - VUB - Bruxelas

Prof. Dr. GERMANO TREMILIOSI FILHO
Departamento de Físico-Quimica / Universidade de São Paulo - USP - São Carlos

Profª. Drª. MARIE GEORGES OLIVIER
Departamento de Clência dos Materiais / Université de Mons - UMONS - Mons

Prof. Dr. DANNY VAN HEMELRIJCK
Mechanics of Materials and Constructions (MeMC) / Vrije Universiteit Brussel – VUB - Bruxelas

Prof. Dr. ASSIS VICENTE BENEDETTI
Departamento de Físico-Química / Instituto de Química - UNESP - Araraquara

Dr. BENNY WOUTERS
Departamento de Materiais e Química / Vrije Universiteit Brussel - VUB - Bruxelas

Araraquara, 08 de outubro de 2019

Institute of Chemistry – Department of Physical Chemistry
Physical Chemistry of Materials Group

Faculty of Engineering – Department of Materials & Chemistry
Research Group Electrochemical and Surface Engineering

Structure and electrochemical properties of PMMA-silica hybrid coatings modified with cerium and lithium ions

Members of the jury

Prof. Dr. Assis Vicente Benedetti	President of the jury São Paulo State University Department of Physical Chemistry
Prof. Dr. ir. Rik Pintelon	Vice-president of the jury Vrije Universiteit Brussel Department of Electricity
Dr. ing. Benny Wouters	Secretary of the jury Vrije Universiteit Brussel Department of Materials & Chemistry
Prof. Dr. Marie-Georges Olivier	External member of the jury University of Mons Department of Materials Science
Prof. Dr. Germano Tremiliosi Filho	External member of the jury University of São Paulo Department of Physical Chemistry
Prof. Dr. Peter Hammer	Supervisor São Paulo State University Department of Physical Chemistry
Prof. Dr. ir. Tom Hauffman	Co-supervisor Vrije Universiteit Brussel Department of Materials & Chemistry

PERSONAL DATA

IDENTIFICATION

Name: Andressa Trentin

Name in bibliographic citations: Trentin, A; Trentin, Andressa.

ADDRESS

Group of Physical Chemistry of Materials (GFQM) located in the Department of Physical Chemistry of the Institute of Chemistry (UNESP), Rua Professor Francisco Degni, 55, Quitandinha, CEP 14800-060 - Araraquara, SP.

EDUCATION

M.Sc. in Chemistry, Jul 2015

São Paulo State University (UNESP), Brazil

Supervisor: Prof. Dr. Elisete A. Batista

“Effects of the presence of cerium oxide on palladium electrocatalysts supports”

B.S in Chemistry, Dec 2011

Regional Integrated University of High Uruguay and Missions (URI), Brazil

PUBLICATIONS

Submitted:

Harb, Samarah V.; Uvida, Mayara C.; **Trentin Andressa**; Lobo, Anderson; Webster, Thomas; Pulcinelli, Sandra H.; Santilli, Celso V.; PMMA-silica nanocomposite coating: Effective corrosion protection and biocompatibility for a Ti6Al4V alloy. Submitted to Materials Science & Engineering C.

Harb, Samarah V.; **Trentin, Andressa**; Uvida, Mayara C.; Magnani, Marina.; Pulcinelli, Sandra H.; Santilli Celso V.; Hammer, Peter. A comparative study on PMMA-TiO2 and PMMA-ZrO2 protective coatings. Submitted to Progress in Organic Coatings.

Accepted:

Trentin Andressa; Harb, Samarah V.; Uvida, Mayara C.; Pulcinelli, Sandra H.; Santilli, Celso V.; Marcoen Kristof, Pletincx Sven, Terryn Herman, Hauffman Tom, Hammer Peter. Dual role of lithium on the structure and self-healing ability of PMMA-silica coatings on AA7075 alloy. ACS Applied Materials & Interfaces. doi: 10.1021/acsami.9b13839.

Harb, Samarah V.; **Trentin, Andressa**; Souza, Thiago A. C.; Magnani, Marina; Pulcinelli, Sandra H.; Santilli Celso V.; Hammer, Peter. Effective corrosion protection by eco-friendly self-healing PMMA-cerium oxide coatings. Chemical Engineering Journal. doi: 10.1016/j.cej.2019.123219.

Published:

Trentin, Andressa; Gasparini, Andressa de L.; Faria, Flávio A.; Harb, Samarah V.; Dos Santos, Fábio C.; Pulcinelli, Sandra H.; Santilli Celso V.; Hammer, Peter. Barrier properties of high performance PMMA-silica anticorrosive coatings. Progress in Organic Coatings, v. 138, p. 105398, 2020.

Torrico, Ruben F.A.O.; Harb, Samarah V.; **Trentin, Andressa**; Uvida, Mayara C.; Pulcinelli, Sandra H.; Santilli, Celso V.; Hammer, Peter. Structure and properties of epoxy-siloxane-silica nanocomposite coatings for corrosion protection. Journal of Colloid and Interface Science, v. 513, p. 617-628, 2018.

Harb, Samarah V.; **Trentin, Andressa**; Torrico, Ruben F. O.; Pulcinelli, Sandra H.; Santilli, Celso V.; Hammer, Peter. Organic-Inorganic Hybrid Coatings for Corrosion Protection of Metallic Surfaces. In: Dr. Carlos Giudice; Guadalupe Canosa. (Org.). New Technologies in Protective Coatings. 1ed.: InTech, 2017, p. 19-51.

CONFERENCES AND PRESENTATIONS

Smart Materials & Surfaces, SMS 2019. Lisbon, Portugal, October 24th – 26th 2019.

European Technical Coatings Congress, ETCC 2018. Amsterdam, The Netherlands, June 26th – 29th 2018.

European Corrosion Congress, EUROCORR 2018. Cracow, Poland, September 9th – 13th 2018.

Smart Coatings 2017. Orlando, USA, February 22th – 24th 2017.

XVI Brazilian Materials Research Society meeting, XVI SBPMat. Gramado, Brazil, September 10th – 14th 2017.

European Corrosion Congress, EUROCORR 2016. Montpellier, France, September 11th – 15th 2016.

XV Brazilian Materials Research Society meeting, XV SBPMat. 2016. Campinas, Brazil, September 25th – 29th 2016.

Brazilian Chemistry Society annual meeting, XXXVIII RASBQ. Águas de Lindóia, Brasil, May 25th – 28th 2015.

AWARDS

Best Young Scientist Contribution at the European Technical Coatings Congress (ETCC 2018 - Amsterdam, The Netherlands) by the presentation “Increased durability and corrosion protection of PMMA-siloxane hybrid coatings modified with cerium and lithium”.

ACKNOWLEGMENTS

Firstly, I would like to thank God Almighty for giving me the opportunity, healthy and mainly life to undertake this research study. Without his blessings, this achievement would not have been possible.

I have great pleasure in acknowledging my supervisor Prof. Peter Hammer for the all the instruction and knowledge, for the patience with my “beginner” questions, for all the weekends working on manuscripts and for being constantly present and helpful. I own to him a very special thanks for all these reasons.

I would like to thank the people who hardly worked in this project, with the data collection, treatment and interpretation: Samarah, Mayara and Victoria who are deeply involved in this work. I also thank my labmates from the Physical Chemistry of Materials Group (GFQM) for the stimulating discussions, friendship and support, in particular Marina and Danubia for atomic force microscopy and thermogravimetry measurements.

I would like to acknowledge Prof. Celso Santilli and Prof. Sandra Pulcinelli for the scientific collaboration.

My sincere thanks also goes to Prof. Tom Hauffman and Prof. Herman Terryn who welcomed me in the Research Group Electrochemical and Surface Engineering (SURF) in 2018, for teaching me in many scientific and personal aspects.

I would like to thank the special friends I met in the SURF Group: Camila, Monika, Alex, Kristof, Jorge, Stephan, Ali, Donovan, Xinhua, Francesca, Thomas, Reynier, Koushik and also to the technical support and friendship of Priya, Kitty, Bart, Carine, Annette, Katrien, Marc, Oscar, Marnix. It was a pleasure to be with them during my internship abroad.

And I would also like to thank the friends I met in Brussels: Luiza, Leonardo, Luciana, Vinicius, Keisy, Igor, Jean, José, Lucas, Cleide, Ricardo, Michele, Ricardo P., Eder, Vanusa. I will always remember our amazing time together!

Next, I thank my special friends who I consider as my family in Araraquara: Joice, Rogério, Luiza, Maciel, Julieti, Jhone, Jaqueline, Guilherme, Sandro, Mateus, João Augusto, Kesia, Douglas, Charles, Denise, Maria, Adriel and Maurício, you are all amazing people!

I thank the São Paulo State University (UNESP), the Institute of Chemistry, GFQM and the Brazilian center for Research in Energy and Materials (CNPEM) for the disposal of infrastructure and the Brazilian Synchrotron Light Laboratory (LNLS) for the use of SAXS equipment.

I would like to thank the funding agency Fundação de Amparo à Pesquisa do Estado de São Paulo (FAPESP), for the scholarships No. 2015/11907-2 and No. 2017/14061-2 received in the period between September 1st, 2015 and November 10th, 2019, and for all the support in Brazil and abroad.

Last but not least, I would like to thank my family: my mom Celia, my dad Geraldo, my brother Cassiano, for their unconditional love and affection, thank you for believing in me. Finally, my deepest consideration to my husband, Victor. Without your support we would be much far from this point. Thank you for being my inspiration, my everlasting love.

ABSTRACT

This work reports on a detailed investigation of the structural and electrochemical properties of poly(methyl methacrylate) (PMMA)-silica coatings. Raman spectroscopy and thermal analysis showed that the fine-tuning of the benzoyl peroxide (BPO) amount, as a critical synthesis parameter, improves the polymerization efficiency of methyl methacrylate (MMA), leading to a highly cross-linked hybrid structure. Electrochemical impedance spectroscopy (EIS) showed for coatings deposited on carbon steel (A1020) and Al alloy (AA7075) a quasi-ideal capacitive impedance response, maintaining the low frequency impedance modulus of up to 10 GΩ cm^2 essentially unchanged during 19 months of immersion in 3.5% NaCl. Although high performance passive coatings have been developed, pitting can significantly affect their durability. Hence, active corrosion inhibition induced by lithium and cerium ions in PMMA-silica sol-gel coatings was investigated. The addition of lithium carbonate yielded coatings with improved connectivity of nanometric silica cross-link nodes and stronger adhesion to the aluminum substrate. EIS results showed that higher lithium concentrations result in an increased impedance modulus and induce the self-healing ability, extending significantly the service life of the coatings. Time-of-flight secondary ion mass spectrometry (ToF-SIMS) and X-ray photoelectron spectroscopy (XPS) suggest that the regeneration process occurs by means of lithium ions leaching from the adjacent coating towards the corrosion spot, which is restored by a protective layer of Li containing aluminum hydroxide species. Finally, coatings loaded with Ce(III) and Ce(IV) provided long term protection for aluminum alloy, however only Ce(IV) imparts active inhibition due to the passivation of cathodic sites by forming highly insoluble Ce oxides and hydroxides. Intermediate Ce(IV) concentrations proved to be more effective in improving the barrier property combined with active protection of intact and damaged coatings over immersion time. In brief, this study found a close relationship between optimized structure, anticorrosive effectiveness and self-healing activity induced by lithium and cerium ions in PMMA-silica coatings, highlighting their high potential of the material for the effective protection of metallic surface.

Keywords: Organic-inorganic coatings, PMMA-silica hybrid, lithium carbonate, Ce(IV), Ce(III), self-healing

RESUMO

Este trabalho relata uma investigação detalhada das propriedades estruturais e eletroquímicas de revestimentos de polimetilmetacrilato (PMMA)-sílica. Espectroscopia Raman e análise térmica mostraram que o ajuste da quantidade de peróxido de benzoíla (BPO), como um parâmetro crítico de síntese, melhora a eficiência de polimerização do metilmetacrilato (MMA), levando a uma estrutura híbrida altamente reticulada. A espectroscopia de impedância eletroquímica (EIS) mostrou para revestimentos depositados sobre aço carbono (A1020) e liga de Al (AA7075) uma resposta de impedância capacitiva quase ideal, mantendo o módulo de impedância de baixa frequência de até 10 GΩ cm^2 essencialmente inalterado durante 19 meses de imersão em NaCl 3,5%. Embora revestimentos passivos de alto desempenho tenham sido desenvolvidos, pites de corrosão podem afetar significativamente sua durabilidade. Assim, a inibição da corrosão ativa induzida por íons lítio e cério em revestimentos de sílica sol-gel de PMMA foi investigada. A adição de carbonato de lítio produziu revestimentos com melhor conectividade dos nós de sílica nanométricos e forte adesão ao substrato de alumínio. Os resultados de EIS mostraram que as concentrações de lítio mais altas resultam em um aumento no módulo de impedância e induzem a autorregeneração que aumenta significativamente sua vida útil dos revestimentos. *Time-of-flight* secondary ion mass spectrometry (ToF-SIMS) e a espectroscopia de fotoelétrons excitados por raios-X (XPS) sugerem que o processo de regeneração ocorre por meio de íons lítio lixiviados do revestimento adjacente em direção ao pite de corrosão, que é restaurado por uma camada de espécies de hidróxidos de alumínio contendo Li. Finalmente, os revestimentos contendo Ce(III) e Ce(IV) forneceram proteção de longo prazo para a liga de alumínio, porém somente Ce(IV) confere inibição ativa devido à passivação de sítios catódicos pela formação de óxidos e hidróxidos de Ce altamente insolúveis. As concentrações intermediárias de Ce(IV) mostraram-se mais eficazes para melhorar a propriedade de barreira combinada à proteção ativa de revestimentos intactos e danificados durante o tempo de imersão. Em resumo, este estudo encontrou uma relação íntima entre estrutura otimizada, eficácia anticorrosiva e atividade de *self-healing* induzida por íons lítio e cério em revestimentos PMMA-sílica, demostrando o alto potencial do material para eficiente proteção de superfícies metálicas.

Palavras-chave: Revestimentos orgânico-inorgânicos, híbrido PMMA-sílica, carbonato de lítio, Ce(IV), Ce(III), *self-healing*.

SAMENVATTING

In dit werk worden de structurele en elektrochemische eigenschappen van PMMA-silica coatings gedetailleerd bestudeerd. Raman spectroscopie en thermische analyses toonden aan dat door de fine-tuning van het gehalte aan de kritische synthese parameter BPO, de polymerisatie efficiëntie van MMA werd verbeterd. Dit leidde tot sterk vernette hybride structuren. Elektrochemische impedantie spectroscopie (EIS) toonde een quasi-ideale capacitieve impedantie respons aan, waarbij de laagfrequentie impedantie modulus van 10 GΩ cm^2 onveranderd bleef gedurende 19 maanden onderdompeling in 3.5% NaCl. Hoewel hoog performante passiverende coatings ontwikkeld werden, kan pitting hun duurzaamheid drastisch beïnvloeden. Het toevoegen van lithium carbonaat resulteerde in coatings met verbeterde connecties tussen de nanometer geschaalde, vernette silica nodules en een verbeterde adhesie met het aluminium substraat. EIS toonde aan dat hogere lithium concentraties leidden tot een verhoogde impedantie modulus en dat de lithium geïnduceerde zelf-herstelling op een significante wijze de levensduur van de gecoate substraten verlengde. Time-of-flight secundaire ionen mass spectrometrie (ToF-SIMS) en X-stralen foto-elektronen spectroscopie (XPS) wijzen erop het regeneratieproces gebeurt door dat de lithium ionen uitlogen vanuit de naburige coating naar de corrosie plaats, die op zijn beurt dan hersteld wordt door de vorming van een beschermende laag bestaande uit Li bevattende aluminium hydroxide bestanddelen. Tenslotte hebben ook de Ce(III) en Ce(IV) bevattende coatings een langetermijns bescherming voor de aluminium legering iopgeleverd. Echter, alleen Ce(IV) resulteerde in een actieve inhibitie door passivatie van de kathodische sites door de vorming van onoplosbare oxides en hydroxides na migratie van Ce ionen vanuit de coating. Gemiddelde concentraties aan Ce(IV) bewezen meer effectief te zijn in het verbeteren van de barrière eigenschappen gecombineerd met actieve bescherming van intacte en beschadigde coatings gedurende de onderdompelingstijd. Kortom, deze studie vond een hechte relatie tussen geoptimaliseerde structuur, anti-corrosie effectiviteit en zelf-herstellings activititeit van lithium en cerium ionen in PMMA-silica coatings.

Sleutelwoorden: Organisch-anorganische hybride coatings, lithiumcarbonaat, Ce (IV) en Ce (III), zelfherstellend.

FIGURES

TABLES

Abbreviations and symbols

AA	Aluminum alloy
AFM	Atomic force microscopy
at.%	Atomic concentration
BE	Binding energy
BPO	Benzoyl peroxide
Ce(III)	Cerium nitrate hexahydrate ($Ce(NO_3)_3.6H_2O$)
Ce(IV)	Cerium ammonium nitrate ($(NH_4)_2Ce(NO_3)_6$)
CPE	Constant phase element
Cr(VI)	Hexavalent chromium
DTA	Differential thermal analysis
DTG	Derivative of the thermogravimetry
EIS	Electrochemical impedance spectroscopy
EEC	Electrical equivalent circuit
EDS	Energy dispersive X-ray spectroscopy
FWHM	Full-width at half-maximum
GDP	Gross Domestic Product
Li	Lithium
LNLS	National Synchrotron Light Laboratory
Li-PB	Lithium intercalated pseudo boehmite
MMA	Methyl methacrylate
MPTS	3-methacryloxy propyltrimethoxysilane
NACE	National Association of Corrosion Engineers
NaCl	Sodium chloride
NMR	Nuclear magnetic resonance
NSS	Neutral salt spray test
OCP	Open circuit potential
ORR	Oxygen reduction reaction
PMMA	Poly(methyl methacrylate)
REACH	Registration, Evaluation, Authorization and Restriction of Chemicals
RMS	Root mean square
SAXS	Small angle X-ray scattering
SEM	Scanning electron microscopy
SiO_2	Silica oxide

STEM	Scanning transmission electron microscopy
TEM	Transmission electron microscopy
TEOS	Tetraethyl orthosilicate
TG	Thermogravimetry
ToF SIMS	Time-of-flight secondary ion mass spectrometry
Wt %	Weight percent
XPS	X-ray photoelectron spectroscopy
α	Porod exponent
C_d	Degree of condensation
C_f	Film capacitance
d	Average distance between particles
δ	Inner layer thickness
E_c	Corrosion potential
E_{SHE}	Standard hydrogen electrode potential
ε_0	Permittivity of vacuum
ε_w	Permittivity in the wet zone
i_c	current density
$I(q)$	Scattering intensity
κ_f	Conductivity at the metal/coating interface
λ	Sharpness of the conductivity decay
R_f	Film resistance
R_g	Radius of gyration
R_s	Electrolyte resistance
P	Porosity
ρ_b	Bulk density
ρ_s	Skeletal density
θ	Scattering angle
τ	Time-constant
Z_Y	Young impedance

TABLE OF CONTENTS

RESUMO EXPANDIDO

Atualmente, a proteção contra corrosão de ligas de aço e alumínio é obtida principalmente pela anodização em combinação com o processo de conversão de cromo hexavalente. Esse método, amplamente aplicado na indústria aeroespacial, está sendo banido por regulamentações dos EUA e da União Européia, como REACH (Registro, Avaliação, Autorização e Restrição de Produtos Químicos) devido aos altos riscos da exposição laboral ao tóxico cromo hexavalente e sua liberação no meio ambiente. Nesse contexto várias estratégias alternativas foram desenvolvidas para substituir os revestimentos de conversão de cromato como proteção contra corrosão de componentes metálicos. Uma das alternativas mais promissoras é a utilização de barreiras físicas de difusão na forma de revestimentos que dificultam a permeação de espécies agressivas.

Os revestimentos híbridos orgânico-inorgânicos são considerados muito promissores para cumprir o papel de proteção contra corrosão eficiente, econômica e ambientalmente compatível. Poucos micrômetros de revestimentos híbridos apresentam desempenho comparável ou até melhor do que os sistemas convencionais combinando primer e acabamento. Quando adequadamente preparado, o material híbrido exibe forte sinergismo entre as fases como consequência do ajuste cuidadoso da composição, proporções e tipo de interação destas. Mais especificamente, nanocompósitos híbridos combinam propriedades como processabilidade, flexibilidade e hidrofobicidade de polímeros com alta estabilidade térmica, química e mecânica de materiais cerâmicos. Esses materiais multifuncionais são de particular interesse para o desenvolvimento de revestimentos anticorrosivos de alto desempenho devido à possibilidade de sintetizar uma rede interconectada, ligando covalentemente ambas as fases na escala molecular e assim formando uma barreira de difusão eficiente.

Estudos recentes sobre a estrutura do sistema híbrido PMMA-sílica mostraram que a fase inorgânica em forma de nódulos nanométricos de sílica-siloxano tem o importante papel de aumentar a estabilidade térmica e mecânica, promover forte adesão ao substrato metálico e principalmente contrair as cadeias de PMMA covalentemente reticuladas as quais vedam hermeticamente a estrutura e, assim,

promovem a formação de revestimentos densos e homogêneos que proporcionam proteção eficiente a longo prazo de superfícies metálicas em contato com ambientes salinos e salinos/ácidos.

Para avaliar a eficiência da proteção contra corrosão de um revestimento, a espectroscopia de impedância eletroquímica (EIS) é a técnica mais aplicada, fornecendo informações detalhadas sobre a evolução sistema eletroquímico eletrólito/revestimento/metal durante a permeação do eletrólito. Na análise padrão dos dados de EIS, um revestimento que sofre absorção de água em contato com uma solução agressiva pode ser descrito por um circuito elétrico equivalente (EEC) composto por uma combinação paralela de resistência e capacitância do filme combinada com uma resistência de transferência de carga e capacitância da dupla camada elétrica na interface revestimento/metal, definindo assim duas constantes de tempo.

No entanto, no estágio inicial de imersão de revestimentos altamente resistivos, as quantidades elétricas da camada não são constantes ao longo da direção normal à superfície. Essa característica leva a um desvio de um comportamento simples do circuito RC devido a uma distribuição contínua de constantes de tempo, resultando em características de ângulo de fase capacitivo na faixa de frequência média e alta. Este comportamento pseudo capacitivo é em geral considerado substituindo o capacitor por um elemento de fase constante (CPE), amplamente utilizado na modelagem EEC para levar em conta a não-idealidade do capacitor. Embora a modelagem de curvas EIS pelo uso de CPE forneça, na maioria dos casos, uma excelente concordância com os dados experimentais, é difícil estabelecer uma relação entre CPE e as propriedades físicas do filme durante a permeação, ou seja, a variação de resistividade e constante dielétrica ao longo a espessura do filme pela absorção não homogênea do eletrólito.

Assim, para fornecer um modelo eficaz que identifique de forma confiável os perfis dos parâmetros físicos e sua evolução durante a progressão dos eletrólitos, alguns autores propuseram um sistema de duas camadas usando o modelo de Young. Essa abordagem é baseada em uma camada externa na interface eletrólito/ revestimento mostrando uma absorção de eletrólitos não homogênea, levando à uma

queda exponencial da condutividade em relação ao volume, dada pelo termo Young, e uma camada de alta impedância essencialmente não afetada na interface metal/revestimento. O ajuste dos dados do EIS, de acordo com este modelo, fornece perfis de parâmetros físicos e sua evolução temporal e, assim, permite uma visão mais profunda do processo de permeação e sua relação com as propriedades estruturais do revestimento.

Na primeira etapa da investigação, foi estudada a influência da estrutura de híbridos de PMMA-sílica modificada por uma variação sistemática do iniciador térmico de polimerização (peróxido de benzoíla) nas propriedades de barreira a longo prazo do aço carbono revestido em contato com o ambiente salino. A alta estabilidade eletroquímica dos revestimentos, investigada por EIS, foi modelada de acordo com o modelo CPE e comparado com a abordagem de duas camadas de Young, esta última envolvendo uma zona de permeação em expansão com condutividade decaindo exponencialmente, a qual explica o desvio das curvas EIS do comportamento capacitivo quase ideal.

Embora revestimentos híbridos de alta-proteção passiva tenham sido desenvolvidos, em caso de danos mecânicos ou corrosivos da camada protetora, o ataque na área afetada leva à perda rápida da integridade estrutural do componente metálico, eventualmente com consequências drásticas. A incorporação de inibidores de corrosão pode melhorar a eficiência de proteção dos revestimentos retardando ou, em alguns casos, até mesmo interrompendo o processo de corrosão pela formação de uma camada inerte na zona defeituosa. Essa inibição de corrosão ativa é capaz de restaurar as áreas danificadas e, assim, reduzir efetivamente o acesso de espécies agressivas na interface revestimento/metal.

Com esse propósito, foi investigado o potencial inibidor do lítio nas propriedades estruturais e a inibição ativa da corrosão de revestimentos de PMMA-sílica modificados com diferentes quantidades de carbonato de lítio. Os resultados demonstram uma melhora significativa na vida útil do revestimento induzida pela lixiviação preferencial do Li em locais afetados pela corrosão, proporcionando melhor proteção ao substrato. Ambas, a estrutura híbrida densa com distribuição homogênea de nanopartículas de sílica altamente reticulados na matriz de PMMA formadas na

presença de lítio e a formação de uma camada protetora induzida por íons de lítio após falha local (pite) e cortes artificiais contribuem para as notáveis propriedades de barreira dos revestimentos. Com base nos resultados de análises estruturais e eletroquímicas, é proposto um mecanismo para a autorregeneração (*self-healing*) induzida pelo lítio.

Entre os inibidores de corrosão inorgânicos, os sais de cério têm sido relatados como os mais eficientes quando adicionados em soluções aquosas. Os íons de cério adicionados no material, incorporados em reservatórios ou diretamente em soluções agem como inibidores catódicos através da precipitação de óxidos e hidróxidos insolúveis em áreas defeituosas. Embora os mecanismos e as mudanças estruturais por cério em revestimentos sol-gel tenham sido amplamente discutidos, uma comparação entre nitrato de amônio cério (Ce(IV)) e nitrato de cério hexahidratado (Ce(III)) na estrutura de revestimentos híbridos de PMMA-sílica depositados em AA7075 ainda não foi realizada.

Os estudos de híbridos modificados com lítio e cério foram realizados por espalhamento de raios-X a baixo ângulo (SAXS), microscopia de força atômica (AFM) e análise termogravimétrica (TGA). Após deposição em alumínio, a atividade dos íons de Li, Ce(III) e Ce(IV) nos revestimentos foi investigada por EIS e teste de névoa salina (revestimentos riscados). O mecanismo inibidor foi estudado usando espectrômetro de massa de íon secundário (SIMS) em um pite de corrosão e microscopia eletrônica de varredura com espectroscopia de energia dispersiva de raios-X (SEM-EDX) para defeitos artificiais. Os resultados revelaram que os íon de Li e Ce(IV) são mais eficiente que o Ce(III) como inibidor de corrosão, conferindo proteção ativa para a liga de alumínio.

Part I

1 Introduction

1.1 Steel and aluminum alloys: fundamentals and applications

Steel is the most used and recycled metal on Earth. From stainless to low carbon steel, it is found in countless applications in our daily lives because of unique properties such as high mechanical and structural strength, low temperability, low cost, ductility and high tensile strength [1]. The development of efficient production techniques in the late 20th century accounted for the basis of construction, transportation, energy, packaging and electronics industries based on different mechanical properties achieved by the variation of carbon content in the composition between 0.2% and 1.8% (Table 1) [1]. Examples of its versatility include more than 50% of the vehicles weight, 75% of appliances such as refrigerators, washing machines, ovens, food and beverage factories and principal component of heavy industries, offshore platforms and pipelines exposed to aggressive environments [1,2].

Similarly, the low cost and availability of aluminum had a significant impact on its metallurgy and applications. Advances in the manufacturing process have enabled the globalization of aluminum alloys in the last 150 years, particularly in the last 10 years, becoming the second most used metal after steel. The sharp increase in aluminum consumption in regions such as China, USA, Japan, India and UK has doubled aluminum production between 2005 and 2015 from 32 to almost 58 million tons [3] owing to its use in aircrafts, packaging and mainly vehicles. More precisely, currently an average of 152 kg of aluminum is present in every car manufactured, with vehicle production increasing from 67 million in 2005 to almost 91 million in 2015 [3].

Materials such as steel and aluminum can have their structure modified with metallic, ceramic or nonmetallic phases that represent unlimited possibilities for modern materials science in the development of light, cheap and highly resistant metals [4]. The main advantages of metal alloys are a favorable cost-performance relation, increased lifespan and the possibility to combine different components providing unique properties for the alloy. Metal reinforcement has many goals, such as weight reduction, improvement of physical and chemical properties, increase of Young's modulus and reduction of thermal expansion [4]. For applications such as

medical technology, extreme resistance to corrosion, low degradation and biocompatibility are required [4]. In addition, it is well known that the CO_2 emissions of a vehicle or aircraft is proportional to its weight, with a direct impact on greenhouse effect. It has been estimated that aviation contributes with about 4.9% to global warming due to emission of greenhouse gases [5]. To reduce emissions, joint efforts by the international community have led to global energy-saving measures and policies that involve research and development of lighter alloys and polymer composites in the aeronautics and automotive industry [3–5].

The incorporation of metallic components into aluminum is driven by its low density (2.7 g/cm^3) relative to steel (7.83 g/cm^3) associated with high resistance and low cost that allow the design lightweight and durable structures. When properly alloyed and treated, aluminum exhibit some degree of corrosion resistance in contact with water, salt and others environmental conditions. This due to the presence of an inert nanometric oxide layer that prevents the advance of corrosion [6]. The modern aluminum alloys of the 7000 series have Mg and Zn as main constituents, used as reinforcers. Cu and other elements are also added to improve hardness and resistance to stress corrosion (Table 1) [3]. Major applications include navy, automotive and aviation sectors besides appliances as climbing equipment, bicycle components, chassis boards, etc. [1]. Aluminum alloys have been gradually replaced by new alloys such as Al-Cu-Li and Al-Cu-Li-Mg, however they are still widely used in many products due to the excellent cost-benefit relation, low melting point for recycling and high mechanical stability [4].

Table 1. Metal composition of steel A1020 and aluminum A7075 used in this work.

Metal	**Composition (wt %)**								
Steel A1020	C		Mn		Si		P		S
	0.2		0.45		0.14		0.01		0.015
Aluminum A7075	Mn	Si	Cr	Ni	Cu	Mg	Fe	Zn	Ti
	0.3	0.09	0.24	0.05	1.48	2.6	0.37	5.64	0.2

1.2 Localized corrosion of A1020 steel and A7075 aluminum

1.2.1 Steel corrosion

Although steel is the most recycled metal, currently two major drawbacks urge the development of new materials and protective systems due to its (i) high weight for transportation and (ii) susceptibility to corrosion, which have a direct impact on CO_2 emissions as well as economical losses and safety issues. Corrosion of steel decreases the service life of a specific component and may cause mechanical failure of the entire structure. Consequently, huge economic losses of $ 2.5 trillions were estimated for 2016 by the National Association of Corrosion Engineers (NACE), equivalent to 3.4% of the Gross Domestic Product (GDP) (2013), in addition to the large number of accidents caused by failures of bridges, pipelines, trains and cars. Apart from this, it was estimated [2] that corrosion control could save 15-35% ($ 375-875 billions) annually in reposition, beyond individual safety and environmental consequences. The A1020 steel, one extensively used alloy, is by nature prone to corrosion because when exposed to humid atmosphere, aqueous systems or soil, it undergoes a severe oxidative process transforming it to its natural ore [1,7]. This makes the search for high performance, inexpensive protective systems imperative.

Steel corrosion results from contact with humid, saline or acidic atmosphere since the involved species act as oxidizing agents in the redox process that corrodes unprotected metals. When steel is exposed to water and oxygen, iron is oxidized to Fe^{2+} and oxygen from air is reduced to hydroxyl ions, reactions that occur separately but simultaneously (Reactions 1 and 2) [1,8]. Fe^{2+} and OH^- ions can combine to produce solid hydroxides such as $Fe(OH)_2$, which reacting further with oxygen and water forming $Fe(OH)_3$, the so-called rust (Reactions 3 and 4) [8,9].

$$Fe \rightarrow Fe^{2+} + 2e^- \quad (1)$$

$$O_2 + 2H_2O + 4e^- \rightarrow 4OH^- \quad (2)$$

$$Fe^{2+} + 2OH^- \rightarrow Fe(OH)_2 \quad (3)$$

$$2Fe(OH)_2 + \frac{1}{2}O_2 + H_2O \rightarrow 2Fe(OH)_3 \quad (4)$$

Some other factors are determining on the kinetics of corrosive process of steel such as presence of salts, pH, amount of oxygen and temperature. A particular relationship is found between salinity and corrosion rate due to hygroscopic chloride

ions which react with metallic ions producing hydrolysable products and hydrochloric acid (HCl) (Reaction 5) [8]. This, in turn, increases the acidity of the electrolyte (the pH drops from 6 to 2-3) and accelerates the corrosion rate in an autocatalytic process [8,10]. In short, Cl^- (i) favors the formation of electrolytes at low relative humidity and (ii) forms soluble corrosion products (e.g. $ZnCl_2$, $CuCl_2$, $FeCl_2$, $FeCl_3$) promoting the electrochemical corrosives processes [8].

$$FeCl_2 + 2H_2O \rightarrow Fe(OH)_2 + 2HCl \qquad (5)$$

When localized corrosion occurs (pitting, crevice or filiform corrosion), the native oxide layer of steel fails, allowing charge transfer reactions by electron transport from the anode (site at which the metal atoms lose electrons) towards the cathode sites (where electrons are transferred to reducing species) until the electrical potential equilibrium is reached. Finally, the formed corrosion layer grows covering the unprotected surface [8,10].

1.2.2 Aluminum corrosion

Although protected by a thin layer of oxide, aluminum alloys are also susceptible to corrosion after dissolution and/or failure of the passive layer, leading to structural failure of the material. Corrosion in form of pitting is particularly favored in aluminum by some parameters such as alloy composition, electrolyte concentration, temperature and potential (relative to the standard hydrogen electrode - E_{SHE}) [11]. Here, anodic and cathodic electrochemical reactions occur separately as the base of the pit is essentially anodic with oxygen depletion (cathodic reagent). After Cl^- adsorption in the micro-flaws of the oxide film, the oxygen reduction reaction slowly occurs in the cathodic sites (Reaction 6) and soluble chlorine and oxychloride complexes are produced at the bottom (inside the pit) [12]. The abundance of metallic cations and anionic species (e.g. chloride) at the base ensures the charges neutrality and lowers the pH due to the formation of aggressive hydrochloric species inside the pit (Reactions 8 and 9) [11–13]. Meanwhile, the electrons from aluminum are transferred to the cathodic sites (outside the pit) where the reduction of water occurs leading to local alkalinization at the cathode (Reaction 10) [14].

$$O_2 + 2H_2O + 4e^- \rightarrow 4OH^- \quad (6)$$

$$Al \rightarrow Al^{3+} + 3e^- \quad (7)$$

$$Al^{3+} + H_2O + Cl^- \rightarrow H^+ + AlOHCl^+ \quad (8)$$

$$Al + 3H^+ + 2Cl^- \rightarrow 3/2H_2 + AlCl_2^+ \quad (9)$$

$$2H_2O + 2e^- \rightarrow H_2 + 2OH^- \quad (10)$$

The composition and microstructure of an alloy may favor the formation of pits as consequence of the different reactivities of intermetallic particles in the electrochemical series of the metals [1]. The more distant in the series of the elements, the greater is the electric potential difference and the tendency to form a redox pair. In the A7075 alloy, Cu used to improve hardness has major influence on the formation of pits. In neutral and aerated solutions, Cu-rich sites have a cathodic role increasing (i) the oxygen reduction reaction (ORR) and (ii) the pH in the vicinity of the pit through the formation of OH^-. Meanwhile, the hydrolysis of aluminum forms corrosion products which may partially or completely obstruct the anodic sites (Reaction 8) [13,15]. In this initial step, the balance between the dissolution of the metal and the mass transfer in the electrolyte controls the kinetics of the pit propagation since the cathodic reaction is limited by the slow oxygen transportation [12]. Then Cu-rich particles are detached from the matrix and scattered in the adjacent cathodic areas further favoring the ORR and the dissolution of aluminum, also called pit propagation [15,16].

Throughout the pitting formation and growth, a porous cover is often formed at the walls of the cavity by cathodic products (oxides and hydroxides) which under neutral-alkaline pH precipitate, filling the pit (Figure 1a) [11]. Next, the pit expansion, underneath a coating for instance, causes delamination and generalized corrosion of aluminum, as can be seen in Figure 1b.

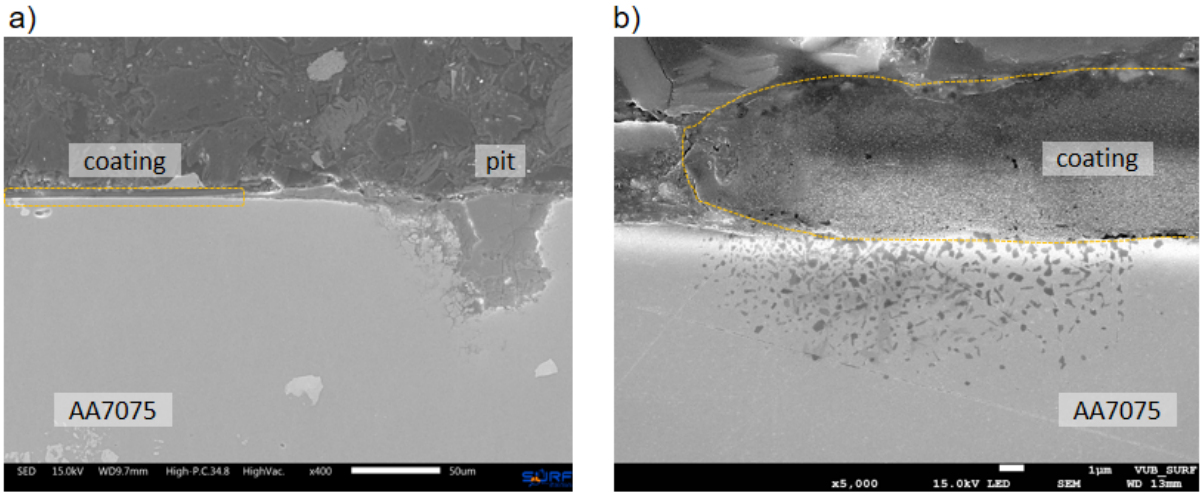

Figure 1. a) Pit filled with corrosion products observed for a AA7075 sample coated with lithium doped PMMA-silica hybrid after 310 days of immersion in 3.5% NaCl and b) corrosion propagation at the coating/aluminum interface. Source: author.

1.3 Behavior of steel and aluminum alloys under variations of the potential (E_{SHE}) and pH

Before proceeding with the complex mechanisms of pitting formation, one should take into account the electrochemical behavior of steel and aluminum under changes of E_{SHE} and pH, important variables of the systems. The regimes for passivation or metallic solubilization are summarized in the Pourbaix diagrams, or E-pH diagram. Carbon steel alloys are poorly corrosion resistant and degrade easily within Fe^{2+} and Fe^{3+} the potential-pH domains, represented by the iron-water Pourbaix diagram (Figure 2a), under formation of corrosion products of iron (Fe_3O_4, $Fe(OH)_2$, and Fe_2O_3) [9]. Concerning the aluminum alloys, they present higher corrosion resistance due to the formation of a native oxide passive layer (~2 to 4 nm thick layer of alumina), stable in the pH range from 4 to 9, ESHE > -1.8 V (Figure 2b) [12]. Hydrargillite ($Al_2O_3.3H_2O$), the most stable hydrated alumina, has been chosen for drawing the equilibrium diagram [17].

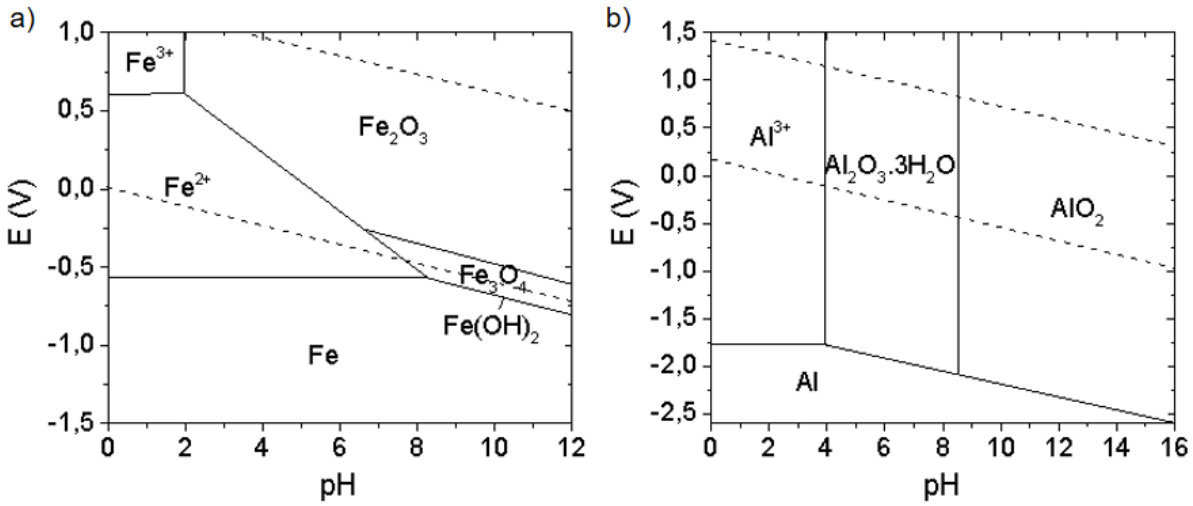

Figure 2. Pourbaix diagrams of systems a) iron-water and b) aluminum-water. Adapted from [17,18].

The main difference between aluminum and steel alloys stems from the presence of a native oxide layer that assigns a superior protection to aluminum which requires a high electrical field for the film breakdown and pitting (in the order of 10^6 to 10^7 V/cm) [11,12]. Furthermore, the passive regime varies in the presence of Cl^- ions for both metals, with significant increase of iron solubility (~175 mmol/L) for Cl^- concentrations above 15 mmol/L at pH 12 – 13. For Al alloys a shift of pitting potential to more negative values (-0.6 to -0.8 V) is observed when immersed in 0.01 – 1 mol/L NaCl [11,12,19,20].

Although Pourbaix diagrams do not report on kinetics of the reaction, they are extremely valuable for mapping the thermodynamic stability of the corrosion products. Outside of the passive region (strong acids and/or alkaline solutions), the probability of steel and aluminum pitting corrosion increases because in these conditions, the metal is stable as an ionic specie (e.g. Fe^{3+}, Fe^{2+}, Al^{3+}) [8]. It is worth mention that in alkaline solutions (pH > 9), aluminum has a strong tendency to corrode in form of aluminate (AlO_2^-), which is not soluble in water, but in strong acids and bases [17]. Hence, using Pourbaix diagrams in practice, corrosion protection strategies and critical tests can be planned more efficiently [18].

Two main conditions accelerate the pitting dissolution reaction in the presence of chlorine ions: the high concentration of iron and aluminum cations inside the pit that favors the migration of chlorine for the charge equilibrium and the ratio of the anodic /

cathodic areas (where metal atoms are ionized and electrons conducted through the metal to reduction reactions, respectively) [1]. Carbon steel exposed to saline solution undergoes pitting corrosion initiated mainly by (i) access of the Cl^- ions through defects in the native layer of oxide or (ii) by dissolving sulfide inclusions of steel under deposited NaCl particles [7]. During the process, at the base of the pit the presence of chlorides (Reaction 5) increases and oxygen scarcity directs the reduction of oxygen to the top, creating a chloride-oxygen gradient [7]. Similarly, corrosion of aluminum alloys, especially those of 2000 and 7000 series, is also known as a microgalvanic process triggered by potential differences between the intermetallic particles and the matrix and other heterogeneities as inclusions faults, displacements, grain contours, etc. [21]. Both processes are summarized in Figure 3.

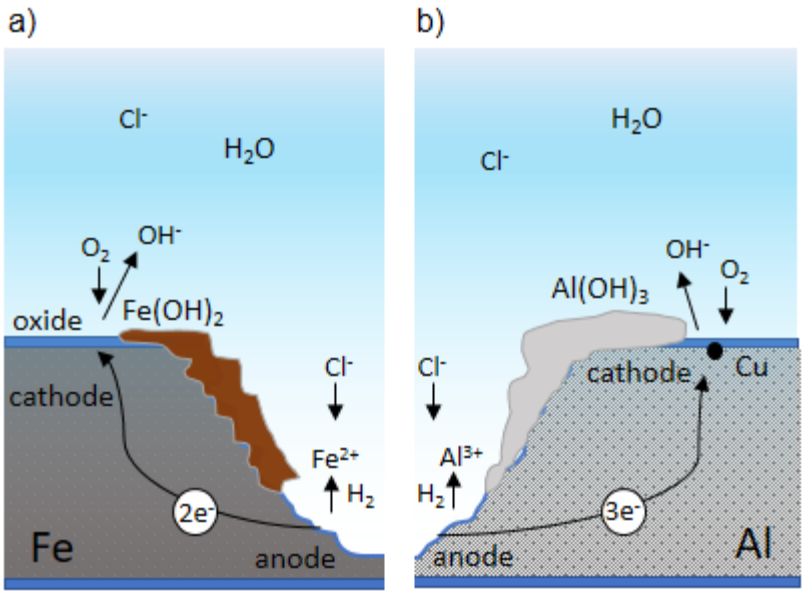

Figure 3. Representative pitting processes of a) iron and b) aluminum upon immersion in aerated neutral saline solution. Adapted from [8,12,13].

1.4 State-of-the-art protection of metallic surfaces

The most prominent and widely used strategy to prevent or delay corrosion on metallic alloys is the application of protective coatings. A very efficient method consists in application of a chromate conversion layer, in combination with a primer (usually an epoxy layer of about 15-25 µm loaded with anti-corrosion inhibitors) and an organic topcoat, mostly in form of a 50-100 µm thick polyurethane topcoat, combining barrier,

decorative, hydrophobic and UV resistant features [22]. Ensembled, these layers provide active and passive protection for the underlying alloy, as represented in Figure 4. The inner chromate layer is applied by immersing the metal component into an acid bath containing chromates, whose excess of non-reduced ions is capable of efficiently protect damaged surfaces exposed to corrosive environments by reduction of Cr^{6+} ions, blocking the dissolution reaction [11,14]. This process produces an extremely corrosion-resistant film composed of mixed Cr(III) and Al(III) oxides [14], as depicted in the Reaction 11:

$$2Al + Cr_2O_7^{2-} + 2H^+ + H_2O \rightarrow +2CrOOH \downarrow +2AlOOH \downarrow \qquad (11)$$

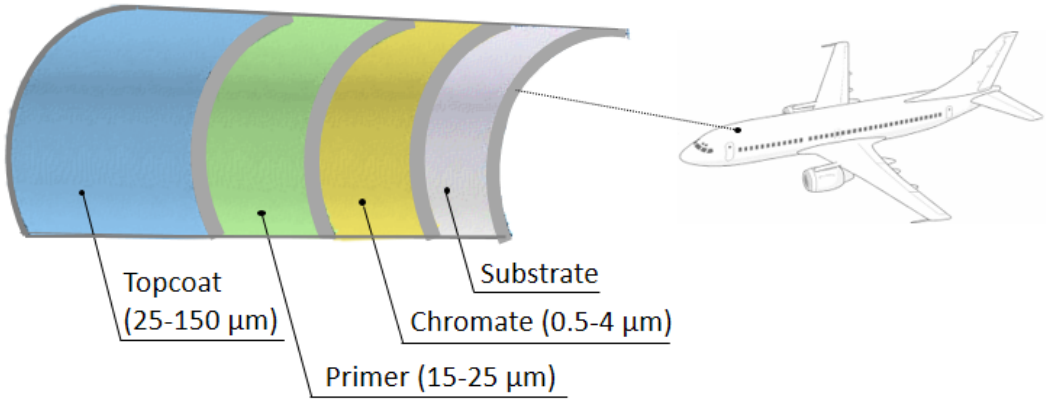

Figure 4. Current system to protect metallic surfaces. Adapted from [23].

Chromates are considered as the most efficient oxidizing inhibitors by passivating the substrate subjected to corrosive attack. As already mentioned, Cr(VI) ions are able of leaching from the coatings and passivate the surface by the chemical conversion process, however the production, storage and use of Cr(VI) compounds in the form of chromate anions (CrO_4^{2-}) and dichromate ($Cr_2O_4^{2-}$) cause occupational health problems due to toxic, carcinogenic and mutagenic effects. Studies indicate that if inhaled, chromium affects the lungs by obstructing the airways and increases the risk of developing lung, nasal or sinusal cancer in workers exposed to Cr(VI) [24]. Among the mechanisms involved, DNA damages, oxidative stress and aneuploidy lead to cellular transformation and consequent carcinogenesis [24].

The high risk involved in the use of toxic hexavalent chromium species, still extensively used in the aeronautic industry, makes it imperative to look for

environmentally compliant alternatives. In the last decade, environmental laws and restrictions around the world have become stricter about the use of chromates and have prompted considerable effort to develop equally effective substituents. Nonetheless despite the emergence of promising materials, the deadline settled for Jan 2019 by US and European regulations as REACH (Registration, Evaluation, Authorization of Chemicals) has not been yet addressed by industry [25]. This is because an effective substituent must inhibit corrosive processes with the same performance as chromate anions [26], that in practice means:

- Formation of an insoluble passive layer in damaged areas;
- Blocking the adsorption of Cl^- into the oxide (passive) layer;
- Increased pH in neutral solutions preventing pitting corrosion;

All of these requirements led to intense search for high performance chromium-free coatings that can passively and actively protect metallic surfaces in harsh environments. To ensure a long-term protection of metallic components, the coating systems must combine (i) a dense and effective passive barrier with a very low permeation rate and, after failure (ii) active protection of metallic surfaces by self-healing ability.

1.4.1 Methodology of preparation and evaluation of high-performance hybrid coatings

Studies addressing the first requirement point out that acrylic, epoxy and polyurethane-based nanocomposites are promising candidates for long-term passive protection [23,27,28]. These coatings represent a class of materials formed by the combination of polymeric and ceramic phases whose final properties are unique and different from the characteristics of the individual components. When properly prepared, a homogeneous hybrid material exhibits synergism between both phases, related to the chemical nature, size, morphology and interfacial properties of the components [29,30].

The corrosion protection reported for inorganic-organic acrylic hybrids have inspired a number of studies to vary the nature and composition of the polymer and inorganic nanophases [27]. The high corrosion resistance achieved by few micrometer thick (< 10 μm) acrylic nanocomposite coatings [27,31,32], results from a

homogeneous combination of organic and inorganic phases using a covalent coupling agent. These agents are molecules whose functional similarities with both phases allow a covalent linking, thus creating a cross-linked network containing inorganic nodes that anchor the coating on the metallic surface and compact the polymer chain segments, while the polymeric phase hermetically seals the coating [33,34]. Organosilanes are the most common coupling agents used in hybrid acrylic coatings because they guaranty a high homogeneity between the acrylic organic moiety and the inorganic phase [35]. They are also known as adhesion promoters, since the organofunctional groups interact with the organic material whereas the inorganic functionality (silica) is compatible with the hydroxide groups of the substrate [34].

The incorporation of an inorganic phase at the nanoscale bypasses the limitations of the purely polymer systems, such as lack of thermal and mechanical stability, swelling of the polymer chains and poor adhesion to the substrate [34,36]. Nanofillers addition also addresses the drawbacks of inorganic coatings, which although highly adherent have residual porosity and stress-induced cracks [27]. For example, the addition of silica into the polymer on the nanoscale is able to fill in the interstitial voids and covalently link to the coupling agent and substrate [37], consequently entangling the polymer chains in a dense configuration limiting the uptake of water and anion molecules to a very low rate.

A promising class of organic-inorganic acrylic materials recently developed as anticorrosive coatings is based on PMMA (poly(methyl methacrylate))-silica hybrids. In a first approach, by changing the MMA/3-methacryloxy propyltrimethoxysilane (MPTS) ratio in the organic phase, Hammer et al. have shown that PMMA-silica nanocomposites with thicknesses between 1.5 and 3 μm are able to increase the corrosion resistance, in terms of low frequency impedance modulus, to 1 GΩ cm^2 during 18 days in 3.5 wt % NaCl solution, a value about five orders of magnitude higher than that of uncoated steel [38]. Subsequently, by varying the ethanol/H_2O ratio of the inorganic phase, dos Santos et al. have related the high connectivity of the silica phase (~83%) to the excellent corrosion resistance, with an almost unchanged impedance modulus of 1 GΩ cm^2 during more than 6 months in saline solution and more than 3 months in saline/acid medium [31]. The multifunctionality of this system was explored

by adding lignin [39], carbon nanotubes/graphene oxide [32] and cerium (IV) salts [40,41], which reinforce the thermal, mechanical (scratch resistance and hardness) resistance, and extend the protection after pitting in 3.5% NaCl solution, respectively. The possibility of incorporating corrosion inhibitors, while maintaining the high passive barrier properties and strong adhesion, makes PMMA-silica hybrid coatings a potential alternative for the primers market.

A key factor for the adjustment of these characteristics is the methodology of preparation that is based on the combination of MMA radical polymerization with the hydrolysis and condensation of the silica phase. In the case of MMA, free radicals from benzoyl peroxyde (BPO) (thermal initiator) can undergo a homolytic breakdown of the oxygen-oxygen bonds under heating, initiating the polymerization reaction at positively charged unsaturated carbons [42]. The final molar mass of the polymer chains depends on the conditions as temperature and initiator concentration, making it possible to control the polymeric structure on a molecular scale. In addition, the coupling molecule must be incorporated in the appropriate ratio to the monomer and inorganic domains to ensure a homogeneous, well-integrated structure. Among various organosilanes used [35], MPTS has been successfully employed without compromising the structure of the nanocomposite thanks to its acrylic and silica functional groups, producing class II hybrids (covalent bonds - Figure 5) [30,31,33].

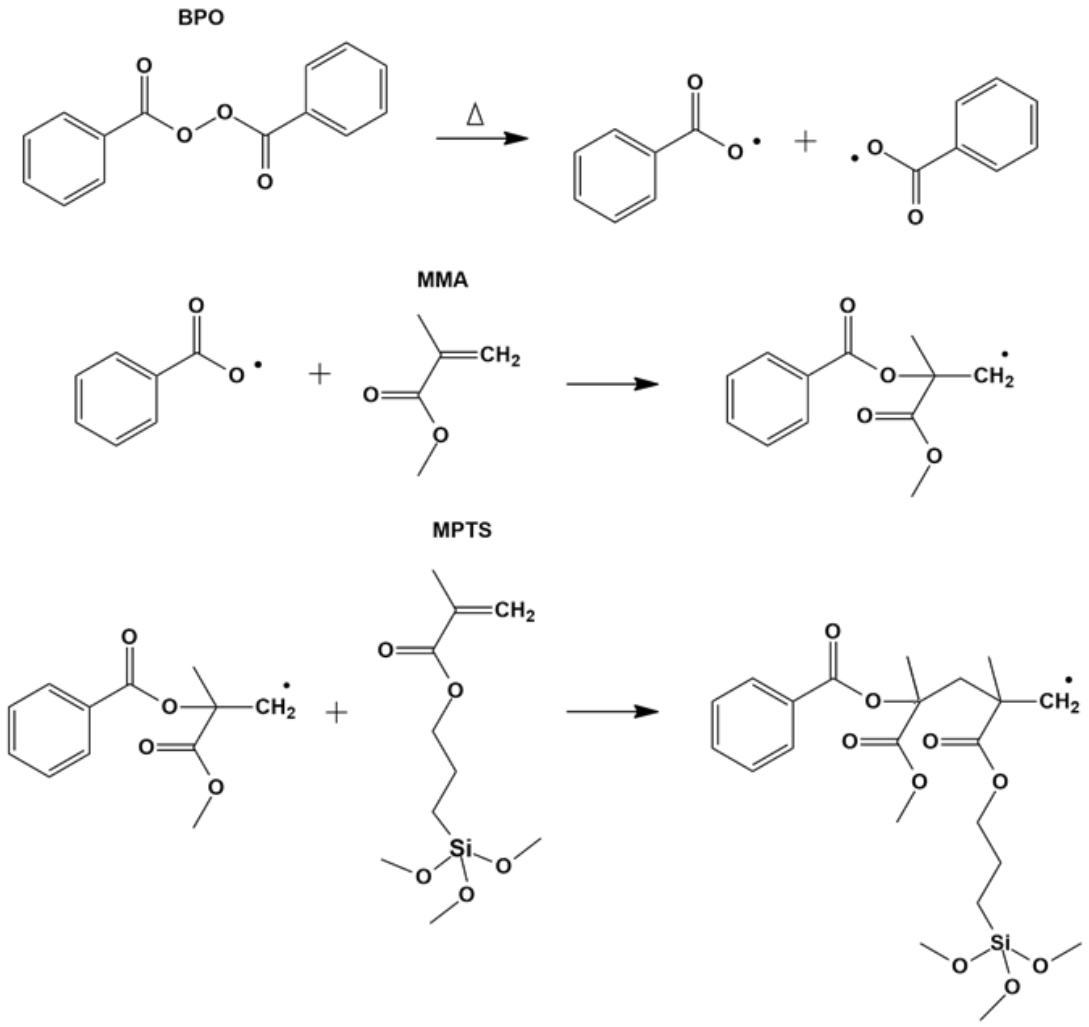

Figure 5. Radical polymerization reaction of MMA and MPTS monomers, using BPO as thermal initiator. Source: Author.

Recent studies on the structure of the PMMA-silica system have shown that the inorganic phase has the important role in increasing the thermal and mechanical stability and promotes strong adhesion to the metallic substrate contributing to long-term protection of metallic surfaces in contact with saline and saline/acid environments [31,38,41]. According to Brinker et al. the main advantages of the silicon alkoxides in relation to the other transition metals are [43,44]:

- Lower electronegativity;
- In polar solvents no oligomerization or association with alcohol is observed;
- Lower reactivity, allowing better control of the reaction processing;

Structural investigation evidenced that the barrier properties of PMMA-silica coatings were achieved by optimizing the formulation of the hybrid in terms of enhancing PMMA polymerization efficiency and silica polycondensation degree. The results indicate that the covalent conjugation of both phases leads to a contraction of the organic phase by the polycondensed silica nodes, thus forming an efficient diffusion barrier, which extends the coating lifetime [27]. This is demonstrated in the Figure 6 by the unaffected surface of the PMMA-silica coating after long-term exposure to saline solution (583 days) in contrast to the corroded surfaces of bare steel and pure PMMA coating, after 1 day of immersion.

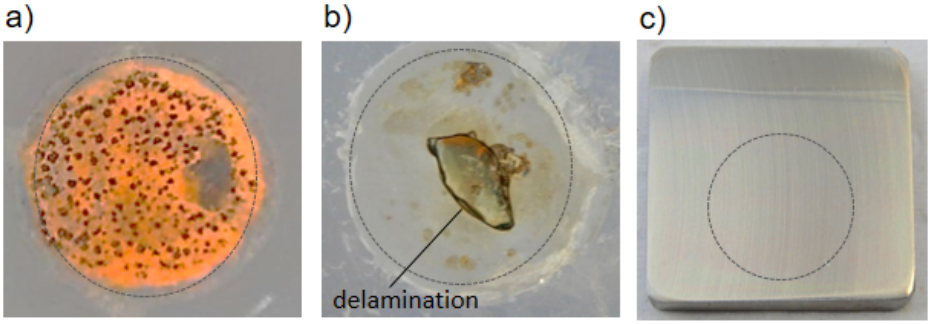

Figure 6. Images of a) bare steel, b) PMMA neat coating after 1-day exposure and c) PMMA-silica coating after 583 days of immersion in 3.5% NaCl. Source: Author.

The synthesis by the sol-gel process consists of four main stages: (i) hydrolysis reaction replacing alkoxide groups (-OR) by hydroxyls (-OH), (ii) hydroxyl condensation reaction forming clusters and silica particles (nucleation), (iii) growth of the particles and (iv) gelling into three-dimensional networks M-O-M [35]. Although the kinetics of hydrolysis and condensation of silicon alkoxides are slower compared to the aluminum, zirconium and titanium alkoxides, they are strongly influenced by the pH that controls the size and shape of the formed structures and reaction kinetics. A clear pH influence is observed by the formation of branched structures under alkaline medium relative to linear structures obtained by acid catalysis [43].

The sol-gel methodology does not require high temperatures or pressures and provides a homogeneous material with particles in the range from <1 nm to 1 μm in the sol, whereas in the gel, rigid structures are formed after hydrolysis and condensation immobilizing the liquid phase in the interstices [44]. Hydrolysis and

condensation occur simultaneously producing hydroxyl and alcohol groups until all alkoxides are substituted. The condensation process can occur via oxolation or olation forming M-O-M or M-OH-M species confirmed through T^J or Q^J species (Figure 7) by silicon Nuclear Magnetic Ressonance (^{29}Si-NMR) [27,33]. The notations Q^J e T^J are usually adopted for orthosilicates ($0 \leq j \leq 4$) and for organosilanes ($0 \leq j \leq 3$) as polycondensation products of tetraethyl orthosilicate (TEOS) and MPTS, respectively, where j indicates the number of Si-O-Si oxygen bridging bonds attached to each silicon atom [27]. The predominance of Q^4 and T^3 species evidences a higher degree of connectivity of the silica phase yielding a more reticulated nanostructure. A homogeneous distribution of these silica nodes in the organic phase is an important issue in the synthesis of dense and highly reticulated hybrids.

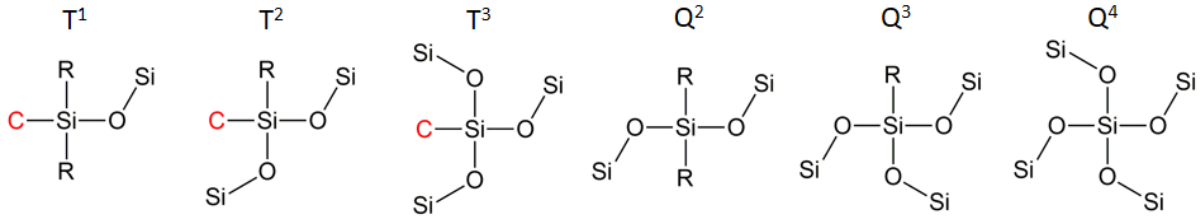

Figure 7. Schematic representation of the T^J ou Q^J species where R indicates OH, OCH_2 or OCH_2CH_3. Adapted from [27,31].

Detailed information on the hybrid nanostructure in terms of the form, size and distribution of silica clusters in the PMMA matrix can be obtained by small angle X-ray scattering (SAXS). This technique is based on X-rays scattering on objects with different electronic densities, such as of silica nanoparticles (higher density) embedded in a polymeric (lower density) matrix. Hence, the modeling of the scattering intensity profiles allows to obtain information of the arrangement (diluted or concentrated set of scatterers) and form (compact or fractal) of silica nanoparticles and defines whether they form a monomodal or a hierarchical structure. These features have a direct impact on the barrier properties of the coatings, showing high corrosion resistance for a diluted monomodal distribution of nanometric silica nodes, contrasting to a heterogenous structure of large (> 10 nm) and/or agglomerated particles [27,31,40,45].

The basic principle for the synthesis of PMMA-silica hybrids is relatively simple, as it combines the hydrolytic condensation of TEOS and the inorganic part of MPTS

with the radical polymerization of MMA. However, the right choice of a large number of variables (about 15) of the synthesis (temperature, time, solvent and molar ratios of: MMA/MPTS, TEOS/MPTS, ethanol/H_2O, H_2O/Si and pH), deposition (withdraw speed, immersion time, drying time, number of dips) and thermal curing (temperature, time, heating rate) makes it quite challenging to establish conditions which allow to obtain an nanostructure that acts as an efficient corrosion barrier. After establishing several of the cited variables [27,31,38], one focus of this doctoral work was to evaluate the effect of critical synthesis parameters, which lead to a high performance barrier. In addition, an exploratory study in the modeling of the electrochemical impedance spectroscopy (EIS) data with equivalent electrical circuits and the two-layer permeation model enabled to access electrochemical parameters (capacitances and polarization resistance) and time evolution of physical quantities, such as thickness of the uptake zone conductivity profiles and variation of the dielectric constant.

1.4.1.1 Evaluation of the coating barrier properties by Electrochemical Impedance Spectroscopy (EIS)

The most widely applied technique for evaluation of the corrosion protection efficiency of a coating system is electrochemical impedance spectroscopy (EIS), which can provide detailed information about the impedance response during electrolyte permeation [46]. In the standard analysis of EIS data, a coating that suffers water uptake when in contact with an aggressive solution can be described by an equivalent electrical circuit (EEC) (Figure 8a) composed of a parallel combination of film resistance and capacitance, combined with a charge transfer resistance and electrical double layer capacitance at the coating/metal interface, thus defining two time constants [46]. However, in the initial stage of immersion, or in the case of coatings with high barrier properties, such as reported for the PMMA-silica hybrids [31], the electrical quantities of the layer are not constant along the direction normal to the surface. This leads to deviation from a simple RC circuit behavior, due to a continuous time constant distribution, resulting in capacitive phase angle characteristics in the medium and high frequency ranges. This pseudo-capacitive behavior is in generally accounted by substituting the capacitor, by a constant phase element (CPE), which is widely used in EEC modeling in order to take into account the non-ideality of the

capacitor [31,46,47]. Although the modeling of EIS curves by the use of a CPE usually pro- vides a very good agreement with the experimental data, a relation between the CPE and the physical film properties during film permeation is difficult to establish, in terms of the variation of resistivity and dielectric constant along the film thickness for an inhomogeneous electrolyte uptake [47,48]. The time evolution of these physical quantities is of particular importance for the understanding of the electrochemical behavior of high performance protective coatings, presenting electrolyte permeation over long time scales [31,49].

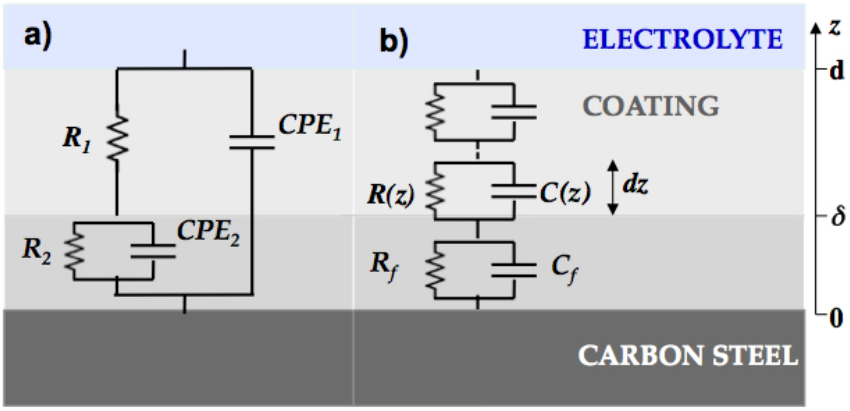

Figure 8. Schematic representation of a) equivalent electrical circuit (EEC) model containing constant phase elements (CPE), and b) two-layer model based on exponential conductivity decay (Young model) in the water uptake zone [48,50].

To obtain an effective model that reliably identifies the profiles of physical parameters and their evolution during the progress of electrolyte uptake, some authors have proposed a two-layer system, using the Young model (Figure 8b) [47,48,50,51]. This approach is based on an external layer at the electrolyte/coating interface, with an inhomogeneous electrolyte uptake, leading to an exponential decay of the conductivity towards the bulk, given by the Young term, and an unaffected high impedance layer at the coating/metal interface. The fitting of the EIS data, according to this model, provides profiles of physical parameters and their time evolution, hence allowing deeper insights about the permeation process and its relation to the structural properties of the coating. Recently, this model was applied to study the immersion time dependence of the physical properties of high impedance organic coatings based on marine epoxy deposited on Q-panel [52] as well as epoxy-polyaminoamide waterborne

films on AA2024 aluminum alloy [50]. The present work investigates the influence of the structure of PMMA-silica hybrids, modified by systematic variation of the polymerization thermal initiator (benzoyl peroxide), on the long-term barrier properties of PMMA-silica coatings on carbon steel in contact with a saline environment.

1.4.2 Active protective coatings: corrosion inhibitors

To replace chromium conversion layers, the second requirement for an effective protection of metallic surfaces in aggressive environments relies on intrinsically active coatings, which dynamically restore their functionally after failure. This can be realized using corrosion inhibitors defined as agents that effectively decrease the rate of corrosion of the metal surface by their chemical activity, thus extending service life of metallic components [53]. When using low cost substances as corrosion inhibitors this approach represents the most economical strategy to prevent or control corrosion of metals. Typically, the inhibition occurs by the formation of an absorption layer or protective film which inhibits or delays electrochemical reactions that lead to the deterioration of the material. It is worth noting that its efficacy is conditioned to the concentration of the inhibitor, solution pH, nature of the aggressive species and type of substrate, making mandatory the appropriate selection of the inhibitor [53]. In practice, inhibitors are chosen by their classification (anodic, cathodic), efficiency, safety of use, costs, environmental issues and compatibility with the system [53].

It is common to classify the inhibitors as cathodic, anodic or mixed, selectively reacting in cathodic, anodic regions or entire surface. In the case of anodic inhibitors, a decrease in the metal dissolution process is observed by a negative displacement in the corrosion potential (E_c) and a reduction of the corrosion current density (i_c), detected by the changes in the slope of Tafel [53]. Similarly, inhibitors capable to displace the E_c positively reducing the i_c and the concentration of the species involved in the cathodic reaction are named cathodic inhibitors. Other substances simultaneously reduce the rates of anodic and cathodic reactions, also known as mixed and ohmic inhibitors. In this case, the combination of decreasing rates and inhibition mechanisms results in further i_c decrease [53].

Table 2 presents a summary of some substances applied as inhibitors and their classifications.

Table 2. Species, type, mechanism, substrates and minimum effective concentration of some substances used as corrosion inhibitors. Adapted from [53–61].

Species	**Type**	**Mechanism**	**Substrate**	**Conc.**
Polyphosphates	Cathodic	Film-forming	Steel, Cu, Mn	10^{-2} mol/L
Tannins and lignins	Cathodic	Film-forming	Steel, Al, Zn, Cu	10^{-3} mol/L
Zinc salts	Cathodic	Film-forming	Steel, non-ferrous	10^{-2} mol/L
Cerium ions	Cathodic	Film-forming	Steel, Al	100 ppm
Orthophosphates	Anodic	Nonoxidizing passivator	Steel, Al	10 ppm
Benzoates	Anodic	Nonoxidizing passivator	Steel, Al, Zn, Cu	10^{-2} mol/L
Chromates	Anodic	Oxidizing passivator	Steel, Al	10^{-3} mol/L
Nitrites and nitrates	Anodic	Oxidizing passivator	Steel, Ti	10^{-3} mol/L
Molybdates	Anodic	Nonoxidizing passivator	Steel, Al, Cu, Zn	200 ppm
Lithium Carbonate	Mixed	Film-forming	Al	10^{-2} mol/L
Phosphonates	Mixed	Film-forming	Steel, Mn	10 g/L
Silicates	Mixed	Film-forming	Steel, brass, Cu	25 ppm
Aromatic azoles	Mixed	Adsorption, film-forming	Steel, Al, Zn, Cu	10^{-3} mol/L
Amines and amides	Mixed	Adsorption	Steel	10^{-2} mol/L
Acetylenic alcohols	Mixed	Adsorption	Steel	10^{-3} mol/L
Sulfur-containing compounds	Mixed	Adsorption	Steel, Al, Ti	10^{-3} mol/L
Hydrazine	Oxygen scavenger	-	Steel	10^{-2} mol/L
Sulphites	Oxygen scavenger	-	Steel	10^{-2} mol/L

Effective inhibitors should prevent redox reactions on metal surfaces by forming a passive film that acts as a physical barrier that blocks or delays corrosive processes. The mechanism involved for corrosion inhibition in near neutral solutions (pH 5-10) was summarized by Magnussen [53]:

- Cathodic: Inhibitors that decrease the oxygen reduction reaction (ORR), restrict the diffusion of the dissolved oxygen towards the surface and form layers of low electrical conductivity.
- Anodic: Substances that form insoluble species with ions of metal corrosion, passivating the surface. Its effectiveness usually depends on the interaction with the ions and the nature of the metal.
- Mixed: Both processes occur, usually with the formation of a thick passive layer that covers the entire surface.

Passive film formation is based on the precipitation of insoluble products as (i) precipitation of oxides and hydroxides from the inhibitory species (cathodic inhibition), (ii) reaction with metallic ions in solution (anodic inhibition) or (iii) reduction or decomposition of the inhibitor on the surface, followed by precipitation [53]. Furthermore, the nature of corrosion is intrinsically associated with local changes in pH as a result of the variation of the solubility of the formed passive species, in particular in form of oxides and hydroxides of inorganic inhibitors [53]. Thus, a passivation inhibitor must be able to hinder the progress of the reaction by shifting the potential (E_{SHE})-pH domain to the passive region (Pourbaix diagrams at Figure 2).

Among the countless investigations of chromate free coatings with organic, inorganic inhibitors and galvanic protection with magnesium, zinc and aluminum (sacrificial anodes), the use of inorganic inhibitors such as cerium and lithium salts incorporated into protective coatings is justified by their efficiency. Rare earth salts are known to precipitate as protective layers at cathodic sites [40,54] whereas lithium carbonate interacts with aluminum corrosion products, forming a passive layer over the entire surface [56,62]. With this perspective, cerium salts in the form of ammonium cerium nitrate and cerium nitrate hexahydrate (Ce(IV) and Ce(III), respectively), and lithium ions from lithium carbonate (Li_2CO_3) were used in this work to modify the PMMA-silica hybrids, aiming to compare their efficiency as active inhibitors, to determine the optimal concentrations, mechanisms associated to each inhibitor and to study structural modifications of coatings previously optimized [31,38].

1.4.2.1 An overview of cerium activity in corrosive regime

Among the inorganic inhibitors, cerium salts have shown promising results when directly added into electrolytic solutions, inside the coatings or liberated from incorporated into reservoirs [40,54,63–66]. In fact, among the lanthanide compounds cerium ions are reported as the most efficient inhibitors in near neutral solutions [67] due to the ability to block cathodic sites, through the reaction with OH^- produced by the oxygen reduction reaction at cathodic areas, increasing the local pH and forming insoluble oxides and hydroxides [63,68]. Different cerium precursors have been used in a number of coatings to protect metals such as carbon steel [40,41], tin coated steel

[60], aluminum alloys such as A2024 [63,64], A7075 [69], A1050 [70], magnesium alloys [71], among others.

After the appearance of localized corrosion (pitting) in near neutral solutions, the cathodic current results from the reduction of oxygen while the anodic current is caused by the dissolution of metal ions (Reactions 1, 2, 7 and 8). At pH > 4 (Reactions 8 and 10), Ce(III) ions selectively react with the hydroxyls formed in the cathode producing $Ce(OH)_2^+$, $Ce(OH)_3$ and eventually undergo further oxidation to $Ce(OH)_4$ and/or CeO_2 (Reactions 12, 13 e 14) [15,68,72].

$$Ce^{3+} + 3OH^- \rightarrow Ce(OH)_2^+ + OH^- \rightarrow Ce(OH)_3 \downarrow \quad (12)$$

$$Ce(OH)_3 + OH^- \rightarrow Ce(OH)_4 \quad (13)$$

$$Ce(OH)_3 \rightarrow CeO_2 + H_3O^+ + e^- \quad (14)$$

However, although likely, the oxidation Ce(III) → Ce(IV) is highly dependent on the local pH, occurring only after relatively long times [15,63,68]. This may be related to an important feature of Ce(IV) ions capable of forming extremely insoluble hydroxides at pH about 3 compared to those from Ce(III) formed at pH about 9, fastening the inhibition according to the environment and type of metal alloy [15,63].

In the case of Ce(IV) addition in PMMA-silica coatings, structural effects were also observed, affecting both the inorganic and organic phase. In the former, Ce(IV) salt complexes with ethanol, consuming the alcohol formed during the hydrolysis and condensation and displace the equilibrium towards the formation of more siloxane groups (Si-O-Si) as represented in the Reactions 15, 16 and 17, whereas in the latter, radicals from the decomposition of the ethanol complex accelerate the opening of the double carbon bond of acrylate, resulting in faster and more efficient polymerization (Reaction 18, where R = vinyl groups) [60]. Both effects favor a more compact structure that hinders the uptake of the electrolyte [40,41].

$$(NH_4)_2[Ce(NO_3)_6] + ROH \rightarrow (NH_4)_2[Ce)NO_3)_5(OR)] + HNO_3 \quad (15)$$

$$\equiv SiOR + H_2O \rightleftharpoons \equiv SiOH + ROH \quad (16)$$

$$\equiv SiOR + \equiv SiOH \rightleftharpoons \equiv SiOSi \equiv + ROH \quad (17)$$

$$Ce^{+4} + R \rightarrow R^* + Ce^{+3} + H^+ \quad (18)$$

1.4.2.2 Corrosion inhibition by lithium carbonate

Recently the effect of lithium carbonate as a corrosion inhibitor in organic films has been studied and the obtained results are very promising to protect aluminum alloys. Visser et al. investigated lithium salts as leachable corrosion inhibitors from polyurethane and epoxy-amine coatings and detected the formation of a protective layer in the artificially damaged area of A2024 and A7075 alloys [73–75]. Dieleman and coworkers observed self-healing activity of lithium carbonate additives on scratched epoxy coatings immersed in 0.05 M NaCl and related this effect to the release of Li ions in the damaged zone [65].

To explain the passivation behavior of lithium some mechanisms have been proposed. Marcoen et al. suggested that the release of lithium from the matrix forms a Li/Al surface layer (hydrotalcites class) by a conversion process [76]. This layer is product of dissolution-reprecipitation reactions that occur within the affected area, in most cases in the form of pits. The 2000 and 7000 series of aluminum alloys are particularly susceptible to pitting corrosion, which is classified as acid or alkaline depending upon the chemistry and the salt acting within the pit during its growth [23,26]. It has been suggested that after the thinning and rupture of the native oxide layer a pH gradient is established within the pit, being more acid at the base of the pit [12,13,26,77]. Then carbonate ions react with a proton (from water) and form hydrogen carbonate and hydroxyl ions (OH^-) creating alkaline conditions (Reaction 19) that induce the formation of an insoluble layer based on lithium-aluminum hydroxide (Reactions 20 and 21) [55,56,76,78–80].

$$CO_3^{2-} + H_2O \leftrightarrows HCO_3^- + OH^- \quad (19)$$

$$Al(OH)_4^- = AlO_2^- + 2H_2O \quad (20)$$

$$Li^+ + AlO_2^- \rightarrow LiAlO_2 \quad (21)$$

The possibility to extend the lifetime of hybrid PMMA-silica coatings after localized failure by incorporating lithium species is one of the goals of this work, thus providing an active protection for aluminum alloys.

2 Objective

The aim of this work is to relate the structural effects induced by different quantities of the thermal initiator of polymerization and investigate two corrosion inhibiting agents (cerium and lithium) in PMMA-silica nanocomposites to the passive and active barrier properties of the coatings.

2.1 Specific goals

- Optimization of the barrier property of PMMA-silica hybrid coatings by systematic variation of thermal initiator of polymerization.
- Modeling of the electrochemical barrier properties using electrical equivalent circuits based on the constant phase element and the Young approach.
- In-depth study on the structural effects induced in of PMMA-silica hybrid coatings by addition of different quantities of cerium and lithium salts in feedback with results obtained by the electrochemical analysis.
- Determination of most favorable conditions in terms of type and concentration of the additive for an efficient active corrosion inhibition.
- Investigation of the mechanisms responsible for the self-regeneration ability induced by Li and Ce ions in PMMA-silica coatings after their failure.

This thesis is divided into three parts and the part II is organized in three chapters addressing aspects of the passive and active protection by PMMA-silica nanocomposites, namely (i) passive diffusion barrier coatings with slow permeation and (ii) active protection after coating failure by lithium and cerium induced passivation of corrosion zones. Chapters 1 and 2 are adapted from published articles and Chapter 3 will be submitted for publication.

3 Experimental

3.1 Materials and samples preparation

The following reagents have been purchased from Sigma-Aldrich: methyl methacrylate (MMA), tetraethoxysilane (TEOS), 3-methacryloxypropyl trimethoxysilane (MPTS), benzoyl peroxide (BPO), ethanol, lithium carbonate (Li_2CO_3), cerium ammonium nitrate ($(NH_4)_2Ce(NO_3)_6$), cerium nitrate hexahydrate ($Ce(NO_3)_3.6H_2O$) and tetrahydrofuran (THF). MMA was previously distilled before use to remove the polymerization inhibitor.

The PMMA-silica coatings were prepared through radical polymerization of MMA and MPTS using BPO as the thermal initiator and THF as solvent in a reflux system at 80 °C/4 h. For the sol-gel synthesis of the inorganic part TEOS was mixed in an acidified (pH = 1) ethanol/water solution at 25 °C/1 h (molar ratio H_2O : ethanol : TEOS = 10 : 5 : 3) [38]. After 1 h of stirring at 25 °C in a closed flask, the inorganic phase (TEOS/acidified in water/ethanol solvent - 4.08 mL / 1.72 mL / 2.83 mL) was added to the organic phase (MMA/MPTS/BPO/THF - 7.82 mL / 2.17 mL / 0.85 g / 40 mL), already polymerized for 4 h in a reflux bath at 80 ºC, and they were mechanically stirred for 5 min. The following molar ratios were kept constant: MMA/TEOS = 8, ethanol/H_2O = 0.5, TEOS/MPTS = 2, and H_2O/Si = 3.5 [31,40].

To study the influence of polymerization, type, concentration and efficiency of thermal initiator and inhibitors (Li and Ce) on the structural and electrochemical properties of the PMMA-silica coatings three series of samples were prepared varying independently the (i) BPO/MMA molar ratio, (ii) Li and (iii) Ce(III) and Ce(IV) concentrations. For the first set of samples the BPO/MMA ratio was varied between 0.01 and 0.1 (0.17 to 1.77 g, corresponding to 0.4 wt % and 3.7 wt % of the organic phase), maintaining the optimized values of the reaction temperature of 80 ºC and the reaction time of 4 h constant. The samples were named B001, B005 and B010, respectively. For this series steel A1020 was used as substrate.

Two other series were prepared to coat aluminum A7075 using a constant BPO/MMA ratio of 0.05. Samples containing lithium ions were produced by adding 0, 500, 1000 and 2000 ppm of lithium carbonate (Li_2CO_3) (10, 20 and 40 mg) in the inorganic precursor solution, denoted as Li0, Li05, Li1, and Li2, respectively. In a third

set, inhibitor agent in form of cerium salts was added into the inorganic phase using 500, 1000, 3000 and 5000 ppm of cerium (70, 150, 450 and 750 mg of Ce(IV) salt and 50, 110, 350 and 590 mg of Ce(III) salt) including the cerium free reference, denoted as: Ce0, Ce(IV)_05, Ce(IV)_1, Ce(IV)_3, Ce(IV)_5, and Ce(III)_05, Ce(III)_1, Ce(III)_3, Ce(III)_5. Finally, the hybrids were deposited on steel and aluminum substrates (25 x 25 x 3 mm) by dip-coating using a withdraw rate of 14 cm min^{-1} at 25 °C and 3 dips with 10 min intervals of air-drying between each immersion. Due to the higher viscosity of Ce(IV)_3 and Ce(IV)_5 hybrid solutions, only two immersions were performed to coat the substrates. The coated substrates and the remaining solution were submitted to two heat treatment steps of 60 °C for 24 h and 160 °C for 3 h to ensure a high degree of polymerization and liberation of all volatile species, as summarized in Figure 9.

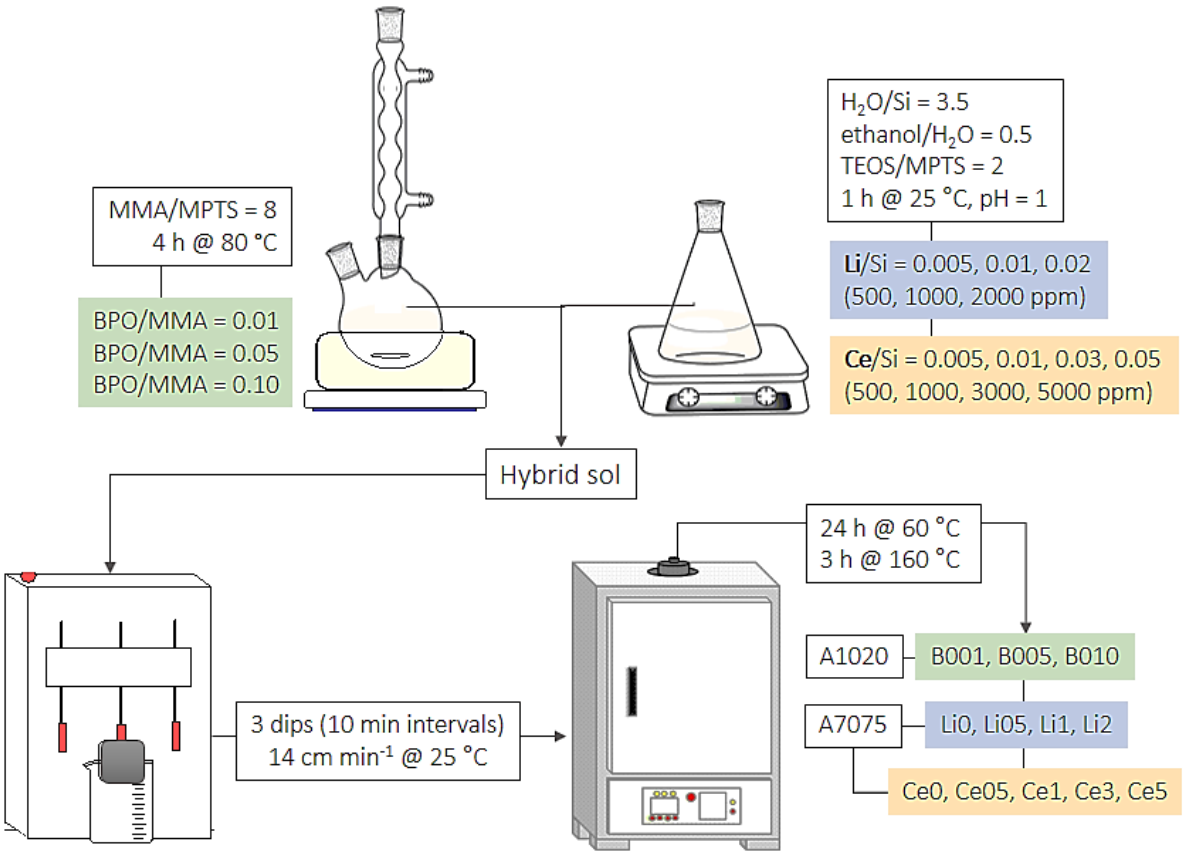

Figure 9. Flow chart of the synthesis procedure used to produce three series of coated steel and aluminum varying the BPO/MMA, Li/Si and Ce/Si molar ratios.

Before deposition, the A1020 carbon steel (ASTM A36) substrates ((wt %) of 0.2 C, 0.45 Mn, 0.14 Si, 0.01 P, 0.015 S, balance of Fe) and the A7075 aluminum ((wt %) of 0.3 Mn, 0.09 Si, 0.24 Cr, 0.05 Ni, 1.48 Cu, 2.6 Mg, 0.37 Fe, 5.64 Zn and 0.2 Ti, balance of Al) were wet grinded using 600 and 1500 SiC abrasive papers, cleaned in an ultrasonic isopropanol bath and dried in a nitrogen stream.

3.2 Characterization methods

The thickness of the coatings was determined using a Filmetrics F3-CS optical interference system, and their uniformity was verified using a XJM900 optical microscope (Instrumental Inc.). Atomic force microscopy (AFM) measurements were performed using an Agilent Technologies 5500 instrument with silicon cantilever (thickness: 4 μm, length: 125 μm, width: 30 μm and force: 42 N/m) in the tapping mode. Using the Gwyddion software, the RMS surface roughness of the coatings was extracted in three different regions (1 × 1 μm^2) from AFM images. Transmittance spectra of the freestanding coatings with average thickness of 300 μm were recorded using a Carry 60 UV-vis spectrometer from Agilent Technologies, in the spectral range from 200 to 800 nm.

The adhesion of the films to the substrate was evaluated by the ASTM D4541 method (Elcometer 510 Pull-Off Adhesion Tester, Elcometer), measuring the tensile pull-off force of detaching. The equipment was calibrated according to the ASTM E74-13a norm (UKAS Calibration Laboratory No. 0157, 2017) and the obtained critical pull-off force refers to the average of 2 measurements. The porosity (P) of unsupported hybrids was calculated ($P = (1 - \rho_b/\rho_s)$) from the values of the skeletal (ρ_s) and bulk (ρ_b) density measured employing a helium pycnometry (AccuPycc 1330, Micromeritics) and a dried-fluid pycnometry (GeoPyc 1360, Micromeritics), respectively.

Raman spectra of the coatings were obtained using a Lab RAM HR 800 (Horiba Jobin-Yvon) spectrometer, with excitation line of 632.8 nm. The spectra were obtained in the range from 200 to 2000 cm^{-1} applying 15 scans and 35 s of exposure time and a N_2 cooled detector. Thermogravimetric analysis (TGA) was performed in nitrogen atmosphere with a flow of 70 mL min^{-1} using a TA Instruments SDT Q600.

Freestanding hybrids films (7.0 mg) were placed in an alumina crucible and temperature was increased from 25 ºC to 800 ºC at a heating rate of 5 °C min^{-1}.

Scanning transmission electron microscopy (STEM) was performed at Electron Microscopy Laboratory (LME/LNNano) using a field-emission gun transmission electron microscope JEOL (JEM 2100F) to visualize the dispersion of the silica nanoparticles into the PMMA matrix. The unsupported PMMA-silica hybrid was embedded in an epoxy resin, cured at 60 °C for 12 h, cut with a diamond knife in 50 nm slices and placed onto a copper grid.

Cross-sections of the coatings were prepared by cutting the substrates, embedding in a conductive resin, polishing and covering it with ~10 nm of evaporated carbon layer to avoid charging. The chemical composition was studied by an Oxford Instruments WDX Spectrometer system WAVE, with four analyzing crystals and an integrated SDD X-MaxN 20 mm^2 EDS detector. The morphology and chemical composition of the cross-section were investigated by scanning electron microscopy coupled with energy dispersive X-ray analysis (SEM-EDS) using a JEOL JSM-7100F field emission microscope at a working distance of 10 mm and an acceleration voltage of 5 kV. SEM-EDS was also used to obtain elemental EDS line profiles recorded along the z-axis and integrated line-scan spectra of the film before and after long-term immersion in 3.5% NaCl.

Electrochemical impedance spectroscopy (EIS) measurements of the coated samples were carried out inside a Faraday cage using a three-electrode electrochemical cell at 25 °C in 80 mL solution containing 3.5 wt % of NaCl using a Potentiostat/Galvanostat GAMRY REFERENCE 600. The contact area of the coated sample (working electrode) with the electrolyte was 1 cm^2. A platinum mesh was used as counter electrode and $Ag|AgCl|KCl_{sat}$ as reference electrode, whose platinum wire was in-parallel connected through a 0.1 µF capacitor to avoid high-frequency phase shifts [81]. After verifying before all EIS measurements that the stability of the open-circuit potential (OCP) was reached within 10 min, a 10 mV_{RMS} sinusoidal potential was applied relative to the OCP to collect 10 points/frequency decade in a frequency range from 1 MHz to 5 mHz, yielding results within the accuracy range of the device. The EIS measurements were repeated after 1 day and then weekly to monitor the evolution of

the coating performance with immersion time. The lifetime of the coating was defined as the time span until a significant drop of the impedance modulus occurred.

The electrochemical stability of the coatings, investigated by electrochemical impedance spectroscopy (EIS), has been modeled according to the standard equivalent electrical circuit CPE model and the two-layer Young approach, the latter involving an expanding uptake zone with exponentially decaying conductivity, which accounts for the deviation of the EIS curves from quasi-ideal capacitive behavior. The Matlab® software was employed to extract the electrochemical parameters for the hybrid coated steel in contact with the electrolyte solution by fitting the experimental EIS curves using the two-layer model proposed by Nguyen et al. [50]. It describes an inhomogeneous electrolyte uptake of the coating, resulting in an exponential decay of the conductivity towards the bulk according to the Young model [51]. In the inner layer, close to the coating/metal interface, the conductivity assumes a constant value, maintaining the characteristic of an unaffected high impedance layer.

Under the assumption that there are two distinct permeation layers in the coating, the impedance of the outer uptake zone can be calculated separately from the inner part. The latter high impedance layer with thickness δ is represented by a parallel combination of film resistance, R_f, and capacitance, C_f, linked in series with the electrolyte resistance R_S and the outer region, represented by the Young model. Thus, the impedance of the inner layer is given by:

$$Z_{\mathrm{RC}} = \frac{R_f}{1 + j\omega\tau_f} \qquad \text{(Eq. 1)}$$

With the time-constant $\tau = R_f C_f$. Assuming a uniform dielectric constant, the water permeation in the wet zone can be represented by Young impedance (Z_Y) given by the integration along the z axis of the wet zone [46,50]:

$$Z_Y = \int_{\delta}^{d} \frac{\exp\left(\frac{\delta - z}{\lambda}\right)}{\kappa_f + j\omega\varepsilon_0\varepsilon_w \exp\left(\frac{\delta - z}{\lambda}\right)} dz \qquad \text{(Eq. 2)}$$

Where d and δ represent the thickness of the coating and of the inner layer, respectively. The parameter λ indicates the sharpness of the conductivity decay, κ_f corresponds to the conductivity at the metal/coating interface, ε_0 is the permittivity of

vacuum and ε_w is the coating permittivity in the wet zone. The integration leads to the solution:

$$Z_Y = -\frac{\lambda}{j\omega\varepsilon_0\varepsilon_w}\ln\left(\frac{\kappa_f + j\omega\varepsilon_0\varepsilon_w \exp\left(\frac{\delta - d}{\lambda}\right)}{\kappa_f + j\omega\varepsilon_0\varepsilon_w}\right) \qquad \text{(Eq. 3)}$$

Consequently, the total impedance of the two-layer system can be calculated by the sum of the electrolyte resistance R_S, inner (Eq. (1)) and outer impedance (Eq. (3)):

$$Z = R_S + \frac{R_f}{1 + j\omega R_f C_f} - \frac{\lambda}{j\omega\varepsilon_0\varepsilon_w}\ln\left(\frac{\kappa_f + j\omega\varepsilon_0\varepsilon_w \exp\left(\frac{\delta - d}{\lambda}\right)}{\kappa_f + j\omega\varepsilon_0\varepsilon_w}\right) \qquad \text{(Eq. 4)}$$

This approach was applied to extract from the EIS curves the parameters, λ, ε_w, κ_f, δ and their time evolution during the permeation of the coating by the saline electrolyte.

The XPS analysis was performed in a PHI 5000 Versaprobe II spectroscope using the Al Kα line (hν = 1486.6 eV) at a spot size of 12 µm and the analyzer pass energy was set to 10 eV. The inelastic background of the Li 1s, C 1s, O 1s and Si 2p photoemission spectra was subtracted using Shirley's method. The composition of the surface region was determined from the ratio of the peak intensities corrected using the Scofield's atomic sensitivity factors of the corresponding elements. The binding energy scale of the spectra was corrected using the C 1s ester group component O-C=O of PMMA (288.8 eV). For the analysis of the chemical bonding structure the spectra were deconvoluted using multiple Voigt profiles, a combination of Gaussian and Lorentzian functions, using the CasaXPS software.

Solid-state ^{29}Si nuclear magnetic resonance (NMR) spectra were recorded using a Bruker Avance III HD 400 WB spectrometer for freestanding films in form of powder at conditions of 400 MHz, 9.4 T and Larmor frequency of 79.49 Hz. The spectra were obtained at sample rotation of 10 kHz, excitation pulse using a power of 140 W and 400 s of relaxation time. Proton decoupling was always used during acquisition of the spectra. The spectra were deconvoluted using a combination of Gauss/Lorentz functions to obtain the degree of condensation (C_d) from the proportion of the intensities of different bonding environments of TEOS and MPTS polycondensation products.

To determine the nanostructural properties, in terms of the size and distribution of silica clusters in the polymeric matrix small angle X-ray spectroscopy (SAXS) measurements were performed at the National Synchrotron Light Laboratory (LNLS at Campinas, Brazil) used to analyze the final organic-inorganic hybrid structure (freestanding coatings). Using a monochromatic radiation (λ = 1,548 Å) and a bi-dimensional detector (Dectris Pilatus 300k) placed at 902.39 mm of the sample (q range = 0.30 - 5.50 nm^{-1}), the scattering intensity I(q) was obtained as a function of the scattering vector, q, which is related to the scattering angle, θ, by the expression $q = (4\pi/\lambda)sin\,(\theta/2)$. The scattering occurs due to the differences of electronic density of the silica phase relative to the polymeric matrix. The presence of a set of spatially correlated scatters can result in constructive interference of the X-ray beam, causing the appearance of a peak in the *I(q)* profile. Its position at q_{max} allows to determine the average distance, d, between the scattering particles: $d \approx 2\pi / q_{max}$.

In the linear regions of the “log I vs. log q” plots, the scattering intensity follows the Porod law, and the slope is corresponding to the Porod exponent, α, related to the geometry of the scattering particles. When α = 4 the particles are spherical and the surface is smooth and for α values between 1 and 3, it shows a fractal character: $I(q) = Aq^{-\alpha}$, where the constant A is proportional to the surface per sample volume [82,83]. The spectra were fitted using the SasView software with the UnifiedPowerRg function for a generalized Guinier/power law object. This model can be used to obtain the average size (radius of gyration - R_g) and morphology of scattering particles, including asymmetric objects such as rods or platelets and fractal shapes. In case of a two-level hierarchical structure of scattering (fine and coarse levels), the correlation between both levels need to be taken into account using the UnifiedPowerRg function from Beaucage model, that is able to approximate the scattering from many different types of particles [84,85]:

$$I(q) = background + \sum_{i=1}^{N}\left[G_i exp\left(-\frac{q^2 R_{gi}^2}{3}\right) + B_i exp\left(-\frac{q^2 R_{g(i+1)}^2}{3}\right)\left(\frac{1}{q_i^*}\right)^{P_i}\right. \quad \text{(Eq. 5)}$$

Where:

$$q_i^* = q\left[erf\left(\frac{qR_{gi}}{\sqrt{6}}\right)\right]^{-3} \quad \text{(Eq. 6)}$$

Chemical maps of the surface and coating/substrate cross-sections were obtained using a TOF.SIMS 5 system (ION-TOF GmbH). A 30 keV Bi_3^+ primary ion beam was used in the high current bunched mode for high mass resolution (approximately 8000 at 29 m/z ($^{29}Si^+$)) with a lateral resolution of 3 µm. The pulsed ion beam target current was approximately 0.70 pA and the mass spectra were acquired over a mass range of 1 – 800 amu calibrated using a list of fragments of known composition, such as Li^+, $C_2H_3O_2^+$, $AlOH^+$ and Al^+. Large area images were obtained by 2000 µm × 2000 µm scans, which were divided into 16 patches of 500 µm × 500 µm. The acquisition time for each patch was 50 s at a resolution of 256 pixels/mm. The data analysis was performed using SurfaceLab software.

For the salt spray tests (ASTM - B117), artificial crosswise scratches formed a groove penetrating into the metal with a width of approximately 50 µm. The corrosion rate, morphology and phases of the corrosion products after immersion before and after salt spray test was evaluated using SEM-EDS.

Part II

Chapter 1[a]: Barrier properties of high performance PMMA-silica anticorrosive coatings

1.1 Structural and thermal properties

PMMA is obtained from the radical polymerization of MMA, initiated by the thermal decomposition of benzoyl peroxide (BPO). The polymerization starts with the double bond of the vinyl group being attacked by radicals formed by the homolytic cleavage of the BPO molecule, involving the formation of another radical. The reaction propagates by the successive linking of monomers, including the MPTS, forming new radicals, and terminates mainly by the combination of two radical chains ends, or by radical disproportionation, where a hydrogen abstraction at the end of one radical chain by another one generates one unsaturated chain and one saturated chain [86]. It is expected that the increase of the BPO to MMA ratio should favor an increase of the polymerization efficiency and lead to a reduction of PMMA chain lengths. Consequently, it might enhance the density of the organic moieties linking the reticulated silica nodes, hence critically affecting the barrier properties of the hybrid film.

To evaluate the structural properties in terms of the degree of polymerization of the PMMA, Raman spectra were recorded for hybrids prepared using different BPO to MMA molar ratios (Figure 10a). The main bands identified in the spectra are summarized in Table 3, including values of reported Raman shifts of pure PMMA [87–90]. The deviation observed between the experimental and reported data values, can be attributed to the variability of the PMMA system, representing coupled oscillators due to the covalent linking with the silica phase. The addition of silica nodes changes

[a] This chapter is adapted from the accepted scientific paper:
A. Trentin, A.L. Gasparini, F.A. Faria, S.V. Harb, F.C. Dos Santos, S.H. Pulcinelli, C.V. Santilli, P. Hammer. *Progress in Organic Coatings*, doi: 10.17632/4nczwt2sjr.1.

the structure of the polymer and consequently the oscillatory frequencies of PMMA segments, making plausible the widening of the bands and the deviation of the vibration frequencies from the pure phase. The band at 1725 cm^{-1}, related to C=O bonds (MMA ester group), was not influenced by the variation of preparation conditions, so its intensity was used as a reference to evaluate the contribution of vinyl groups (C=C) of MMA, identified at 1640 cm^{-1} [87–90]. It can be observed that with increase of BPO fraction, the C=C band at 1640 cm^{-1} disappeared, while there was increased intensity of the carbon-carbon vibrations of the aromatic ring of BPO, at 1001 and 1600 cm^{-1}. This is a clear indication that the higher number of radicals provided by BPO shifted the chemical equilibrium towards a higher polymerization of MMA.

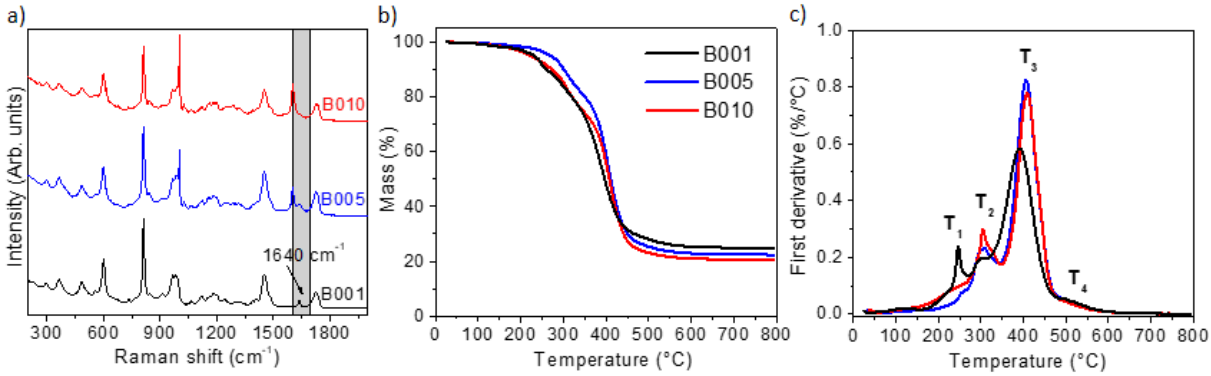

Figure 10. a) Raman spectra b) TG and c) DTG curves for the PMMA-silica hybrids prepared using different BPO/MMA ratios.

Table 3. Raman shifts of functional groups of the PMMA-silica hybrid according to [87–90].

Raman shift (cm^{-1})	Reported Raman shift (cm^{-1})	Attribution
299	304	*δ (C-C-C) of CC_4 groups
483	487	*υ (C^--C^+OO^-) (out of plane)
555	537	δ (C-C-C)
601	604	υ (C-C-O)
732	736	υ (C-C)
813	818	υ (C-O-C)
842	833	δ CH_2
911	914	trapped THF
966	970	δ (α-CH_3) rocking
984	991	δ (O-CH_3) rocking
1000	1001	δ (C-C) aromatic ring of BPO
1122	1125	υ (C-C)
1158	1161	υ (C-O-C-)
1183	1188	υ (C-O-C-)
1241	1234	υ (C-O)
1409	1400	δ (CH_2) wagging
1450	1449	δ (CH_3)
1485	1490	δ (CH_2)
1600	1600	δ (C=C) aromatic ring of BPO
1640	1640	υ (C=C)
1725	1710	υ (C=O)

* δ – bending; υ – stretching

Thermogravimetry under an N_2 atmosphere was applied to analyze the decomposition process in terms of the thermal stability of the hybrid structure and to determine the mass percentage of the inorganic residue (SiO_2) at high temperatures. The TGA and DTG (first derivative of the TG) curves (Figure 10b and Figure 10c) showed that the PMMA phase presents three degradation events with increasing temperature. These involve the rupture of head-to-head segments (stacking defects) at about 240 °C (T_1), breaking of unsaturated chain ends at ~300 °C (T_2), and a generalized depolymerization of head-tail segments at ~400 °C (T_3) [91,92]. After elimination of the silanol groups at about 520 °C (T_4) [45] the polymeric phase is completely degraded, and the residue is formed by the silica phase.

The DTG curve shows clearly that the stacking defects (T_1 events) are strongly suppressed for higher BPO/MMA ratios. The temperature for the onset of thermal stability (T_0), defined as the temperature at mass loss of 5%, shifted by 40 °C to a higher temperature (270 °C) for B005, evidencing an improved polymerization of the organic phase (Table 4). Although T_0 is lower for the B010 hybrid, the depolymerization temperature (T_3) reached the highest value (410 °C). This is possibly related to the reduction of the fraction of the inorganic phase in the hybrid, from 25±1% to 21±1%. The decrease of the residual is in line with results of Raman spectroscopy (Figure 10a) and with the increase of the C/Si ratio observed by XPS (Table 5). The results showed that tuning of the BPO fraction improves the connectivity of the polymeric phase and reduces stacking defects of MMA units, resulting in improved thermal stability of the material.

Table 4. Temperature of the thermal stability limit (T_0), thermal degradation events (T_1-T_3), and residual mass at 800 °C, extracted from curves of Figure 10c.

	T_0	T_1	T_2	T_3	Residual (%)*
			(ºC)		
B001	230	245	300	390	25
B005	270	-	305	405	22
B010	223	-	305	410	21

T_0: Temperature indicating 5% mass loss (thermal stability), * Error: ±1%

X-ray photoelectron spectroscopy was applied to quantify the elemental composition of the hybrids, extracting the proportion between the organic to inorganic phase given by the C/Si ratio, and to evaluate the evolution of local bonding structure with varying preparation conditions, assessed by the analysis of the deconvoluted C 1s, O 1s and Si 2p core-level spectra. Figure 11 displays representative C 1s, O 1s and Si 2p spectra of the B001 hybrid coating, fitted by components related to the different chemical environments of MMA and the polycondensation products of TEOS and MPTS. The results showed for all samples that the chemical bonding structure of the hybrids does not change significantly with increasing BPO fraction. Compared to the reference sample (B001), only a small intensity reduction of the O-Si component at 532.7 eV was detected in the O 1s spectrum, accompanied by an intensity decrease of the Si 2p spectra, assigned to the silica-siloxane phase (SiO_x), indicating an increase

of the proportion of the organic phase [93]. These findings agree with the increase of the carbon to silicon ratio, listed in Table 5 together with the atomic concentrations of all detected elements. In agreement with the observed increase of the C/Si ratio, Raman results show a significant increase of the polymerization efficiency for higher BPO content (Figure 10a). Therefore, within the experimental error, the elevated fraction of the organic phase, observed by XPS, is possibly related to the contribution of trapped residual MMA in the near surface region of the coatings.

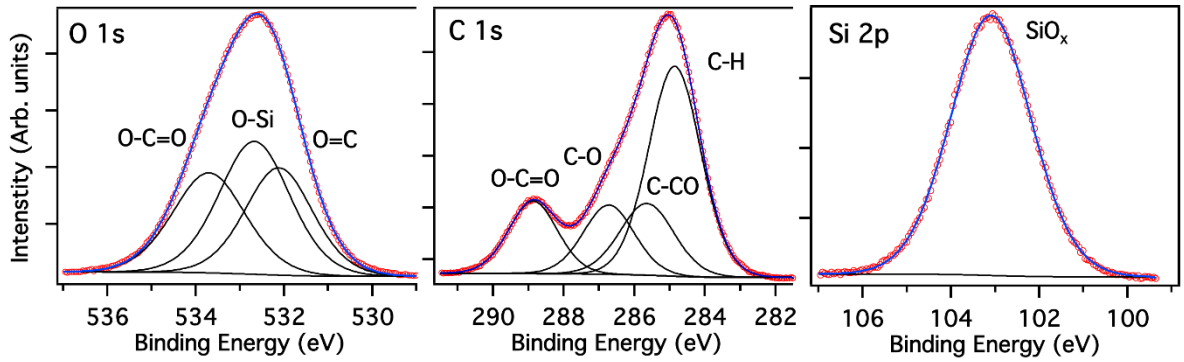

Figure 11. Representative XPS O 1s, C 1s and Si 2p spectra of the B001 coating.

Table 5. Composition and C/Si ratio of PMMA-silica hybrid coatings prepared at different synthesis conditions of the organic phase.

	B001	B005	B010
		(at.%)*	
Oxygen (O 1s)	34.9	37.0	35.6
Carbon (C 1s)	56.6	54.8	57.3
Silicon (Si 2p)	8.5	8.2	7.1
C/Si**	6.6	6.8	8.2

*Experimental error: ±5%,
**Experimental error: ±10%

The bonding structure of the silica phase was studied using magic-angle spinning nuclear magnetic resonance (MAS-NMR). Figure 12 displays the ^{29}Si spectra of hybrid samples prepared using different BPO/MMA ratios. The observed broad resonances at -48, -57 and -65 ppm were assigned to T^1 ($–CH_2Si(OSi)(OR)_2$, R = H or CH3), T^2 ($–CH_2Si(OSi)_2$ (OR)) and T^3 ($–CH2Si(OSi)_3$) structural units, respectively, related to the polycondensation product of MPTS. Resonances related to TEOS polycondensation products were detected at -92, -101 and -109 ppm, corresponding to Q^2 ($Si(OSi)_2(OR)_2$, R = H or CH_2CH_3), Q^3 ($Si(OSi)_3(OR)$) and Q^4 ($Si(OSi)_4$) species,

respectively [94]. The absence of monomer species T^0 ($–CH2Si(OR)_3$) and Q^0 ($Si(OR)_4$) is in agreement with the cluster-cluster condensation mechanism, expected under strongly acid conditions [94]. The proportions of T^J and Q^J species present in the hybrid nanocomposites were extracted from the spectra by a peak fitting procedure using Gauss functions to determine the relative peak area of each species. The degree of condensation (C_d) of the inorganic phase was calculated from the relative proportions of each T^J and Q^J species according to the following equation:

$$c_d = \left[\frac{(T^1+2T^2+3T^3)}{3} + \frac{(Q^1+2Q^2+3Q^3+4Q^4)}{4}\right] \qquad \text{(Eq. 7)}$$

The degree of polycondensation of the silica nodes, extracted from the fitted spectra, was in the range from 81.5±0.5% (B001) to 83.3±0.5% (B010). The observed tendency for increasing connectivity of the silica phase (specially of Q-species related to TEOS polycondensation products) for samples prepared using the highest BPO/MMA ratio coincides with a high polymerization efficiency of the organic phase, resulting in enhanced barrier properties of this coating, as discussed below. A similar trend, however with smaller values, has been already observed for PMMA-silica prepared at BPO/MMA = 0.01 varying the ethanol/H_2O ratio with C_d ranging between 78% and 83%) [31].

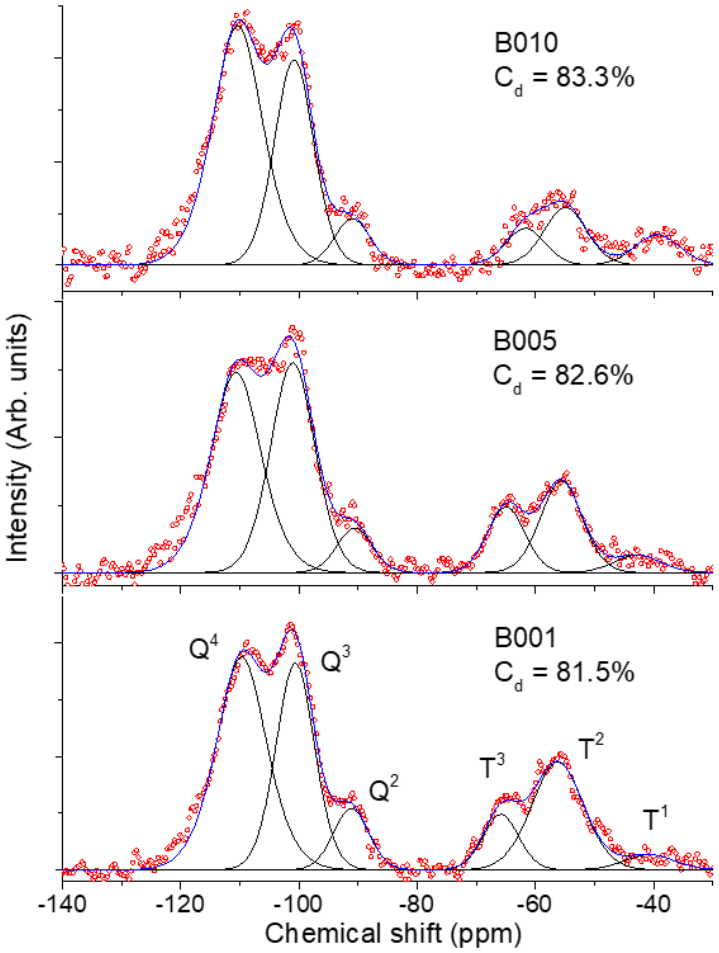

Figure 12. Fitted ^{29}Si NMR spectra of the PMMA-silica hybrids with different BPO/MMA fraction.

Other important characteristics expected for coatings with effective corrosion protection are structural homogeneity, very low porosity, and strong adhesion to metallic substrates. All samples presented a very smooth surface with RMS roughness of less than 1nm, as determined by AFM (Figure 13b). Optical inspection of the coated steel samples showed that all coatings were transparent, homogeneous, and free from macroscopic defects (Figure 13c and Figure 13d). The transmittance spectra obtained for freestanding hybrids, displayed in Figure 13e, evidenced their transparency (80% – 90%) in the visible spectral range. The red-shift of the absorption edge in the UVA spectral range might be related to an increasing contribution of the aromatic BPO species (Figure 13e). The FEG-SEM (Figure 13f) and AFM (Figure 13b) micrographs showed that the surface of all coatings is homogeneous, free form of cracks or pores.

The STEM image (Figure 13g), confirmed the uniform distribution of silica nanoparticles in the PMMA matrix. The silica nodes have an average size of about 2 nm and are spaced at mean distance of 4.6 nm as determined by small angle scattering (SAXS) analysis in a previous study [31].

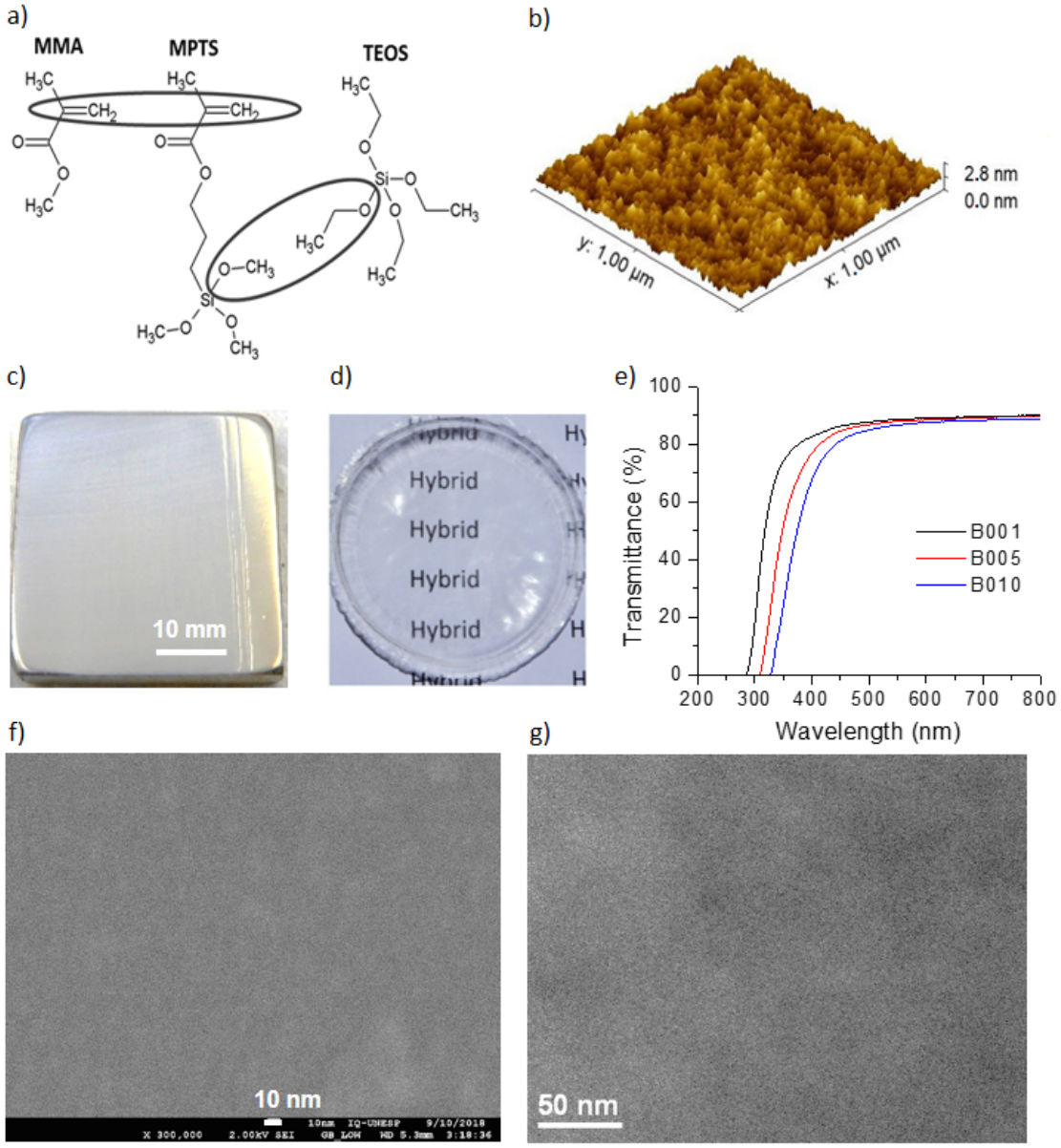

Figure 13. a) Representation of the molecular structure of the PMMA-silica hybrid precursors, showing the reactive groups of MMA and silicon alkoxides, b) 3D AFM topography image of B001 coating deposited on carbon steel, c) representative image of hybrid coated carbon steel and d) unsupported hybrid, e) UV-vis transmittance spectra of unsupported hybrids, f) FEG-SEM image of B001 coated surface, g) STEM of the B001 hybrid.

Pycnometry measurements of the unsupported PMMA-silica hybrids revealed that the porosity was within the error bars of the technique. The results showed that the bulk density (1.299±0.033 - 1.303±0.026 g/cm^3) was higher than skeletal density (1.221±0.004 - 1.271±0.003 g/cm^3), resulting in slightly negative porosity values, which is indicative for an absence of open pores in the thermally treated samples. In contrast, a pure PMMA sample presented a small residual porosity of 1.58%, reflecting the important role of silica as a densification agent of the hybrid. Adhesion measurements revealed a high critical tensile pull-up detachment force, reaching 26.3MPa for the B001 reference coating, while somewhat lower values were obtained for the B005 and B010 coatings (14.8MPa and 8.9 MPa, respectively). For comparison, a value of 6.7 MPa was obtained for a pure PMMA coating. The strong adhesion of the hybrid coatings to the steel substrate is due to the formation of covalent bonds between silanol groups of the hybrid and iron oxy-hydroxide species at the coating/steel interface [37,45]. Therefore, the observed decrease of adhesion with increasing BPO fraction can be attributed to the higher amount of the PMMA phase in the hybrid. Several studies have associated the adhesion strength with corrosion protection properties. Values reported for pull-off tests (ASTM D4541) were 17MPa for a 14 μm thick coating of a silica-epoxy nanocomposite on magnesium alloy AZ31 [95], 3 MPa for ~120 μm thick epoxy-silica coating on steel [96] and about 4 MPa for a 7 μm GPTMS/TEOS coating on AA5083, also validated by cross tape test (ASTM D3359) with the highest score of 5B [97].

1.2 Electrochemical barrier properties

The intrinsic barrier properties of the PMMA-silica films were investigated using electrochemical impedance spectroscopy (EIS) of the coated and uncoated steel immersed in neutral 3.5% NaCl solution. The measurements were performed in regular intervals until a significant drop of the impedance modulus was observed, referred to as the lifespan of the coating. Prior the acquisition of EIS data, the open circuit potential (OCP) was measured before all measurements over a period of 10 min (Table 6). Compared to the OCP value recorded for the bare carbon steel substrate after 3 h of immersion (−718 mV/Ag/AgCl), the coated samples showed a stable time dependence

at anodic potentials, indicating an elevated barrier property of coatings with a thickness between 2.3 and 9.7μm (Table 6). The variation of the film thickness was due to the higher viscosity of the hybrid solution prepared using higher BPO/MMA molar ratios.

In general, coatings with an low frequency impedance modulus higher than 100 MΩ cm^2 are considered to provide a very good corrosion protection, while values below 1 MΩ cm^2 indicate a poor barrier property [98]. The results of EIS measurements after 3 h of contact with saline solution show that all the PMMA-silica coatings were highly corrosion resistant (Figure 14). All samples, prepared for each formulation in duplicate, exhibited a low frequency impedance modulus normalized by the thickness of the coating ($|Z_{lf}|$ thickness^{-1}), near or above 1 GΩ cm^2 μm^{-1} while the capacitive phase angle behavior (-80° < Φ < -90°) close to that of an ideal capacitor, over almost the entire frequency range. The weighted low-frequency impedance modulus was used to take into account the effect of increasing thickness due to the higher viscosity of the solution. Compared to the bare carbon steel, which showed a completely corroded surface after 1 day of exposure (Figure 6a). with an impedance modulus of few kΩ cm^2, the unaffected PMMA-silica coatings presented up to 6 orders of magnitude higher values of $|Z_{lf}|$ thickness^{-1} highlighting their elevated barrier property. The results were similar for the B001 and B005 coatings (Table 6), while a further increase of BPO resulted in an improvement of the corrosion resistance. The elevated anticorrosion performance of the B010 coating can be attributed to the high polymerization efficiency of a less defective organic structure, as suggested by the Raman and TG/DTG results (Figure 10).

Table 6. Film thickness (d), open circuit potential (OCP) after 3 h of immersion in 3.5% NaCl saline solution, impedance modulus ($|Z_{lf}|$ thickness^{-1}) after 3 h and 21 days of immersion, normalized by the coating thickness, and lifespan for PMMA-silica coatings deposited on carbon steel. The values were obtained in duplicate.

Samples	Film thickness d (μm)	OCP 3 h (mV/Ag/AgCl)	$\|Z_{lf}\|$ thickness^{-1} (GΩ cm^2 μm^{-1})		Lifespan (days)
			3 h	21 d	
B001	2.8 / 2.3	191 / 155	1.7 / 0.4	0.6 / 0.1	56 / 40
B005	5.0 / 3.5	173 / 107	1.1 / 1.2	0.4 / 0.1	42 / 21
B010	9.7 / 7.6	385 / 375	2.4 / 1.5	2.0 / 0.3	>583 / 311
Carbon steel	–	-687 / -718	–	–	–

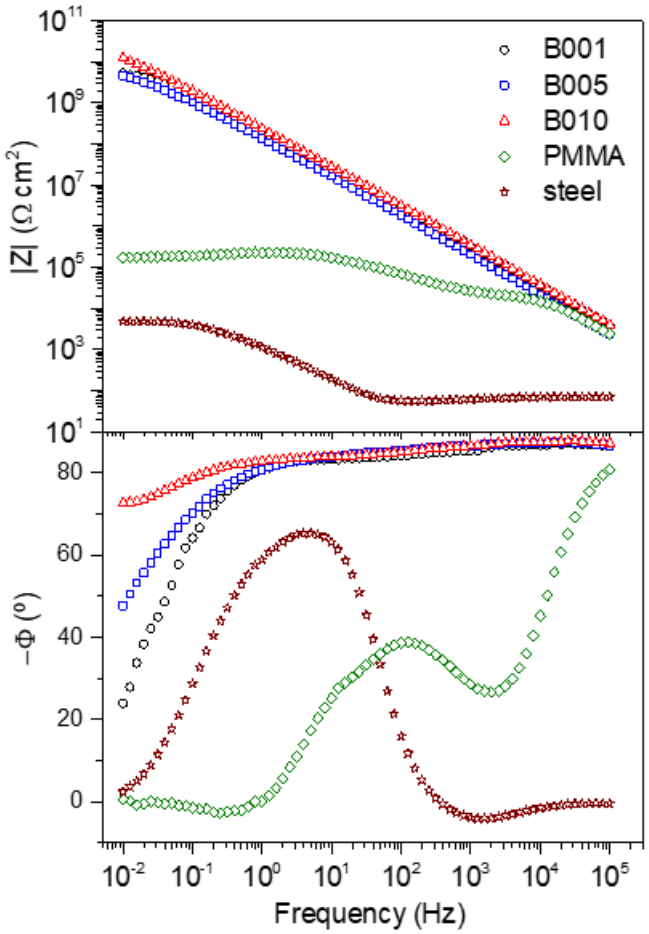

Figure 14. Bode plots recorded after 3 h immersion in neutral 3.5% NaCl, for PMMA-silica coatings on carbon steel prepared at different BPO/MMA ratios, pure PMMA (BPO/MMA = 0.01) and bare steel.

Besides the high initial corrosion resistance, another important pre- requisite for the applicability of protective coatings is their long-term stability in aggressive environments. As shown in Figure 14, the reference coating (B001) presented an initial low frequency impedance modulus of about 1 GΩ cm^2 μm^{-1} and a maximum lifespan of 56 days (Table 6). Similar corrosion protection performance was found for the B005 sample. However, a higher BPO fraction significantly improved the durability of the BPO010 coating, with a high impedance modulus (~2.4 GΩ cm^2 μm^{-1}), maintaining essentially unchanged for up to 19 months. These findings reveal a clear trend of increased corrosion protection for the higher BPO/MMA proportion, which yielded samples with reproducibility of impedance modulus in the GΩ cm^2 μm^{-1} range at low frequencies. To our best knowledge, such remarkable long-term performance,

achieved for a few micrometers thick coating, has not been reported previously. In terms of high impedance modulus (> GΩ cm^2), similar results were recently obtained for somewhat thicker acrylic, epoxy and polyurethane hybrid coatings, listed in the Table 7.

Table 7. Reported high performance acrylic, epoxy and polyurethane hybrid coatings for corrosion protection of metallic surfaces: composition, substrate, thickness, impedance modulus at low frequency, $|Z_{lf}|$, (EIS), lifetime and solution.

Coating	Substrate	Thickness (μm)	$\|Z_{lf}\|$ (GΩ cm^2) Lifetime (days), Solution	Ref.
Acrylic resin-SiO_2	Mild steel	75	~ 10 90 3.5% NaCl	[99]
PMMA-MPTS-TEOS	A1010 carbon steel	1.5 – 2	~ 5 196 3.5% NaCl	[31]
PMMA-MPTS-TEOS-Ce(IV)	A1010 carbon steel	~ 2	~ 10 304 3.5% NaCl	[40]
PMMA-MPTS-TEOS-Ce	Mild steel	~ 26	~ 10 362 3.5% NaCl	[41]
PMMA-MPTS-TEOS-CNTs or GO	A1020 carbon steel	3 - 6 μm	~ 3 211 3.5% NaCl	[32]
Epoxy-zinc phosphate - iron oxide	Cold rolled low carbon steel	55-140	~450/ 60 220/405 3 wt % NaCl	[100]
Epoxy-PANI	Mild steel	20	10-100 120 3.5 wt % NaCl	[101]
Epoxy-APTES-tetra-thiol	Al alloy AA2024-T3	150	~1 350 0.5 M NaCl	[102]
Polyurethane- ZrO_2-SiO_2	Carbon steel	40 – 55	~ 100 226 3.5% NaCl	[28]
Polyurethane-urea	Carbon steel	-	~ 0.1 100 3.5% NaCl	[103]
Polyurethane-MMT	Carbon steel	~ 40	~ 10 225 3.5% NaCl	[104]

PMMA: poly(methyl methacrylate); MPTS: 3-(trimethoxysilyl)propyl methacrylate; TEOS: tetraethoxysilane; CNTs: carbon nanotubes; GO: graphene oxide; PANI: polyaniline; APTES: aminopropyltriethoxysilane; MMT: montmorillonite.

Figure 15 compares the B010 and B005 samples in terms of the time dependence of the open circuit potential (OCP), the phase angle (Φ) at a low and a high frequency (0.1 Hz and 1 kHz) and the low frequency impedance modulus ($|Z_{lf}|$) for the B010 and B005 samples. The B010 coating only small decreases of OCP, Φ and $|Z_{lf}|$ values during the lifespan of 583 days, while the B005 coating failed after 21 days due to pitting, resulting in a sharp drop of all three parameters. No surface degradation was observed in the immersed zone for the B010 sample. It is interesting to note that the OCP values recorded for the B010 coating at the end of its lifespan correspond to those found in the initial stage of B005.

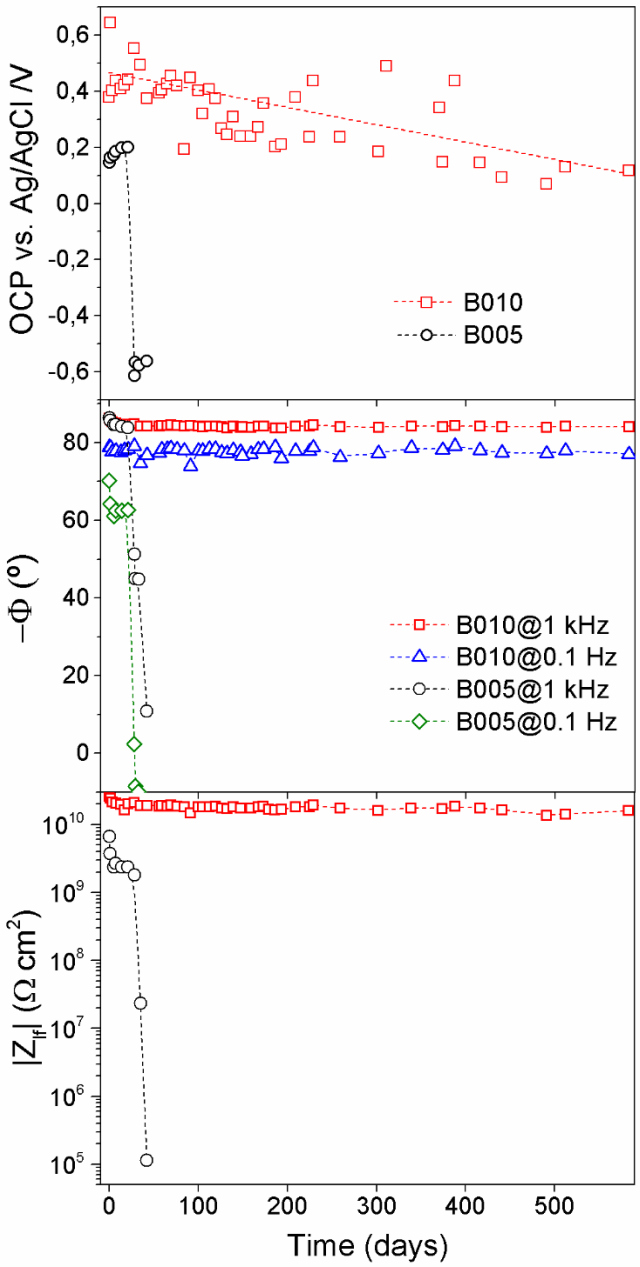

Figure 15. Time dependence of the open circuit potential (OCP), phase angle (Φ) at 1 kHz and 0.1 Hz, and impedance modulus $|Z_{lf}|$ for B010 and B005 coatings.

To obtain more information about the electrolyte permeation process in the two coatings before failure, the EIS curves were fitted using an equivalent electrical circuit (EEC) with two time constants containing constant phase elements (CPE): one at high frequencies, related to the water uptake zone at the electrolyte/coating interface, and a second one at low frequencies, associated with the response of the underlying high impedance layer adjacent to the coating/steel interface (Figure 8a). The EEC

parameters obtained from the best-fit curves of the EIS data (Figure 16) after 3 h and after long-term exposure are summarized in Table 8. As expected, for both samples, the pore resistance (R_1) in the water uptake zone was several orders of magnitude lower than that of the inner layer, which reached a value as high as 59.2 GΩ cm^2. The difference of about four decades in the resistances for the uptake zone and the inner layer was more evident for the B010 coating. The low capacitance values (C_1, related to the water uptake zone, and C_2, associated with the inner layer), calculated using $C = Q^{1/n} R^{(1-n)/n}$, where Q and n are CPE parameters and R is the coating resistance [47,105], are characteristic of a coating with very low pore density, which efficiently blocks the entrance of corrosive species. Concerning the CPE exponents, $n_1 < n_2$ was expected with n_1 close to 0.5, associated with surface heterogeneity and consequently low pore resistance (R_1) in the uptake zone, and n_2 close to 1.0, (where n = 1 represents an ideal capacitor) with a much higher resistance (R_2) due to a dense high impedance layer at the coating/steel interface [52,106,107]. However, as shown in Table 8, the inverse relationship was obtained for the two exponents. Similar inverse behavior has been reported for high performance coatings [32,52], indicating the limited validity of the EEC model for this coating system [106,107].

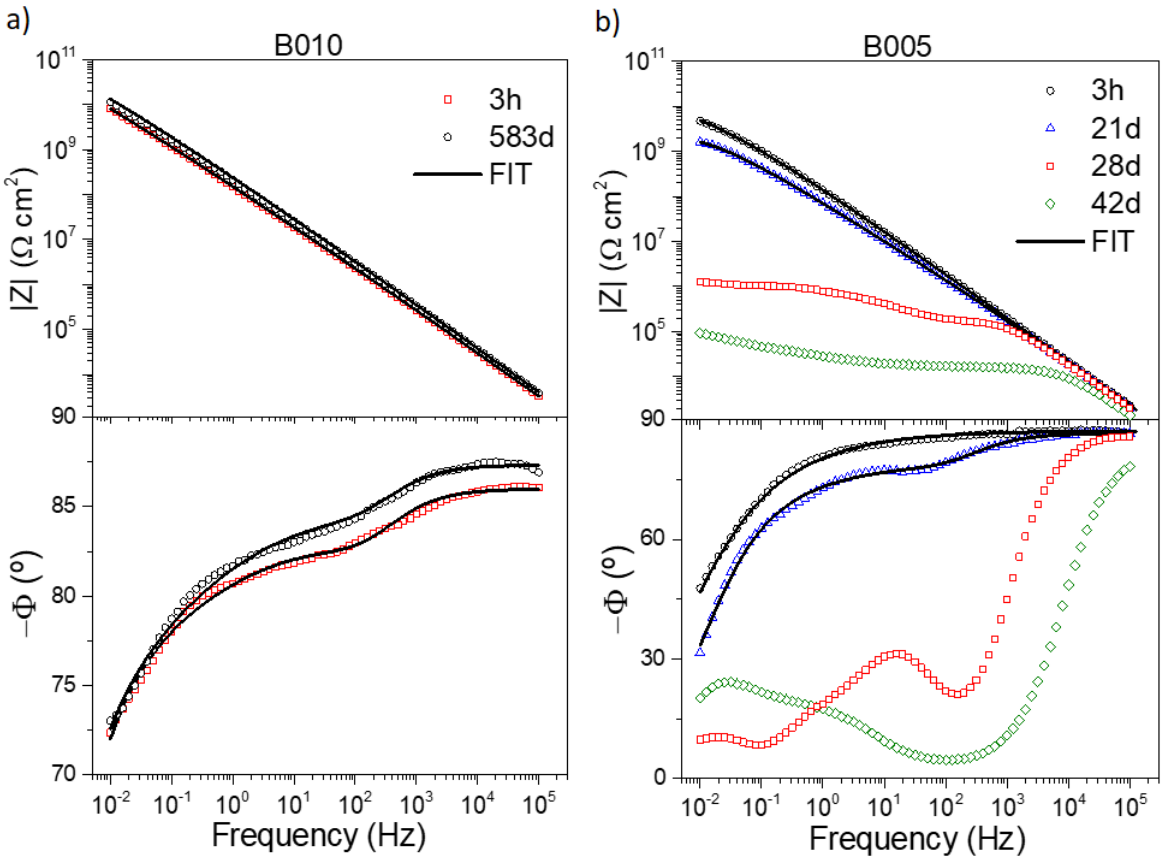

Figure 16. Bode plots for different periods of immersion of PMMA-silica coated steel samples in neutral 3.5% NaCl: a) for B010 and b) B005. The symbols represent the experimental data and the solid lines are fits obtained using the EEC/CPE model of Figure 8a.

Table 8. Time dependence of the EEC parameters obtained for samples B005 and B010 immersed in 3.5% NaCl.

Sample	B005 (3 h)		B005 (21 days)		B010 (3 h)		B010 (583 days)	
χ^2	2.9×10^{-4}		6.8×10^{-4}		4.7×10^{-4}		2.5×10^{-4}	
R_1 (MΩ cm^2)	3.37	(14.8)*	1.75	(6.6)	4.27	(13.4)	2.88	(8.9)
Q_1 (nΩ^{-1} cm^{-2} s^n)	1.17	(0.5)	1.29	(1.1)	0.61	(0.9)	0.88	(0.7)
n_1	0.96	(0.1)	0.96	(0.1)	0.96	(0.1)	0.95	(0.1)
C_1 (nF cm^{-2})	0.97		1.04		0.52		0.70	
R_2 (GΩ cm^2)	3.65	(3.3)	1.32	(1.0)	59.2	(9.1)	29.8	(3.4)
Q_2 (nΩ^{-1} cm^{-2} s^n)	0.83	(0.9)	1.97	(0.7)	0.31	(1.7)	0.44	(1.4)
n_2	0.56	(0.5)	0.69	(0.8)	0.71	(0.4)	0.72	(0.3)
C_2 (nF cm^{-2})	3.45		4.06		1.77		1.97	

*The values in the parentheses correspond to the error (%) for each parameter

As an alternative to the CPE model, the two-layer approach, given by Eq. 4, was used to obtain more details about the electrochemical system, in terms of the evolution of the physical properties during electrolyte permeation prior to coating failure (Figure 17). As the Young impedance is only slightly dependent on the frequency, it might also account for the observed continuous time-constant distribution in the Bode plots for samples with elevated barrier property, showing a phase angle dependence as an extended plateau close to -90° over a wide frequency range (Figure 14). In this model, the impedance in the uptake zone is represented by a continuous distribution of infinitesimal RC elements along the z-axis (Figure 8b) resulting in an exponential decay of conductivity, with a sharpness given by λ, in the interval $\delta \leq z \leq d$, according to the representation of the model in Figure 17c:

$$\kappa(z) = \kappa_f exp\left(\frac{d-z}{\lambda}\right) \qquad \text{(Eq. 8)}$$

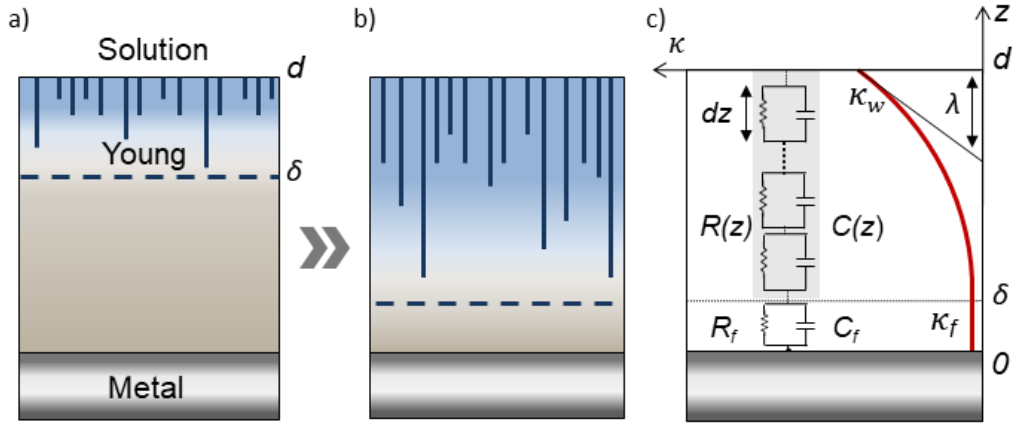

Figure 17. Representation of the electrolyte permeation through the coating according to the two-layer model for: a) the initial stage of contact with the solution, and b) after long-term exposure; c) the corresponding continuous time-constant distribution, resulting from an exponential conductivity profile along the z-axis in the water uptake zone.

Excluding the frequently observed case of fast pitting at defective film sites, which allows rapid access of the electrolyte to the metal substrate, the permeation of water can proceed relatively fast (within hours or days) by the diffusion process through residual pores, while a much slower diffusion rate of solvated Cl^- ions is expected [50,52]. However, slower penetration of water and corrosive species is expected for

thick organic coatings or high performance hybrid coatings with very low pore density, which exhibit almost unchanged EIS profiles during long periods of time [31,49,108,109]. This implies the existence of a preserved high impedance inner layer of nearly constant conductivity at the coating/metal interface. During the initial stages of electrolyte contact, the thickness of this pristine layer (δ) might be close to the film thickness (d), decreasing progressively with increasing immersion time (Figure 17a and Figure 17b). The progressive thickness reduction of the inner layer leads to a small but continuous decrease of the impedance modulus and a slight drop of the phase angle, which is more pronounced at low frequencies (Figure 16) [31,49]. The timescale of the permeation process of corrosive species depends critically on the connectivity and homogeneity of the hybrid network, resulting in an extended coating lifetime for an optimized formulation

The cross-sectional microstructure of the B010 coating was examined using SEM images acquired before and after 583 days of immersion (Figure 18). The micrographs, including details of the coating/steel inter- face, show a homogeneous, non-porous, and defect-free coating, which remained essentially unaffected after long-term immersion. No signs of an ongoing corrosion process were found at the coating/steel interface (Figure 18b). Further evidence for the long-term stability of the coating was provided by EDX line profiles recorded along the z-axis of the film (Figure 19a). The concentration profiles of all the elements constituting the coating (C, O and Si), including Fe at the coating/steel interface, remained almost unchanged after long-term exposure. However, a small increase of the O content at the coating/steel interface is indicative of beginning formation of water percolation paths within the inner layer. With a detection limit for chlorine of less than 0.3 at.% no indication for the presence of Cl^- ions was detected in the integrated line-scan spectra (Figure 19b). Interestingly, the iron profile showed an increase of the Fe content at the coating/steel interface, suggesting the presence of an interfacial diffusion layer, which could have contributed to the strong adhesion of the coatings. The reason for the high carbon content close to the film surface is not clear, although a possibility might be that the resin mold contributed to this signal.

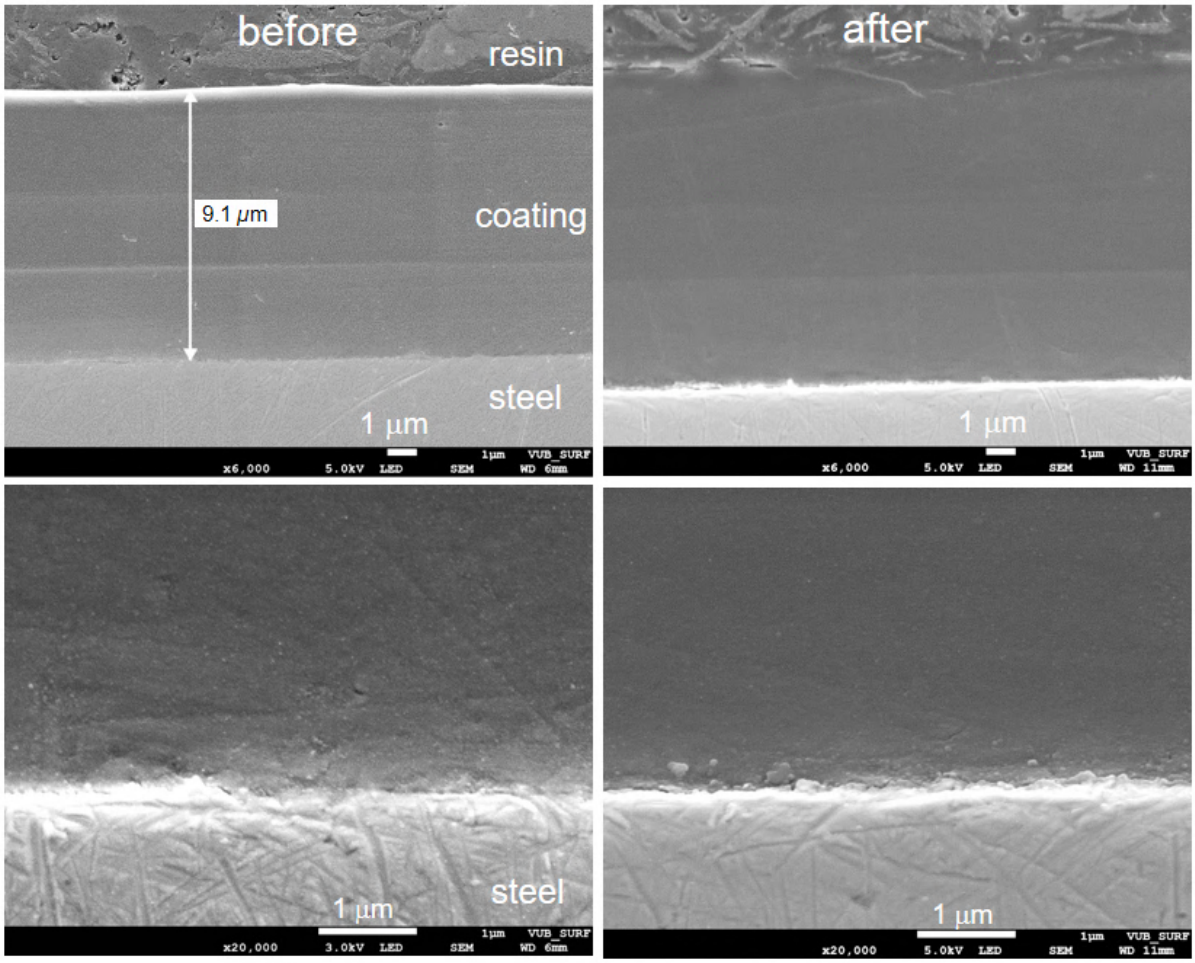

Figure 18. Cross-sectional SEM images of the B010 coating, before (left) and after (right) 583 days of immersion in 3.5% NaCl solution. The layers visible in the images were due to three dips performed for deposition of the coating.

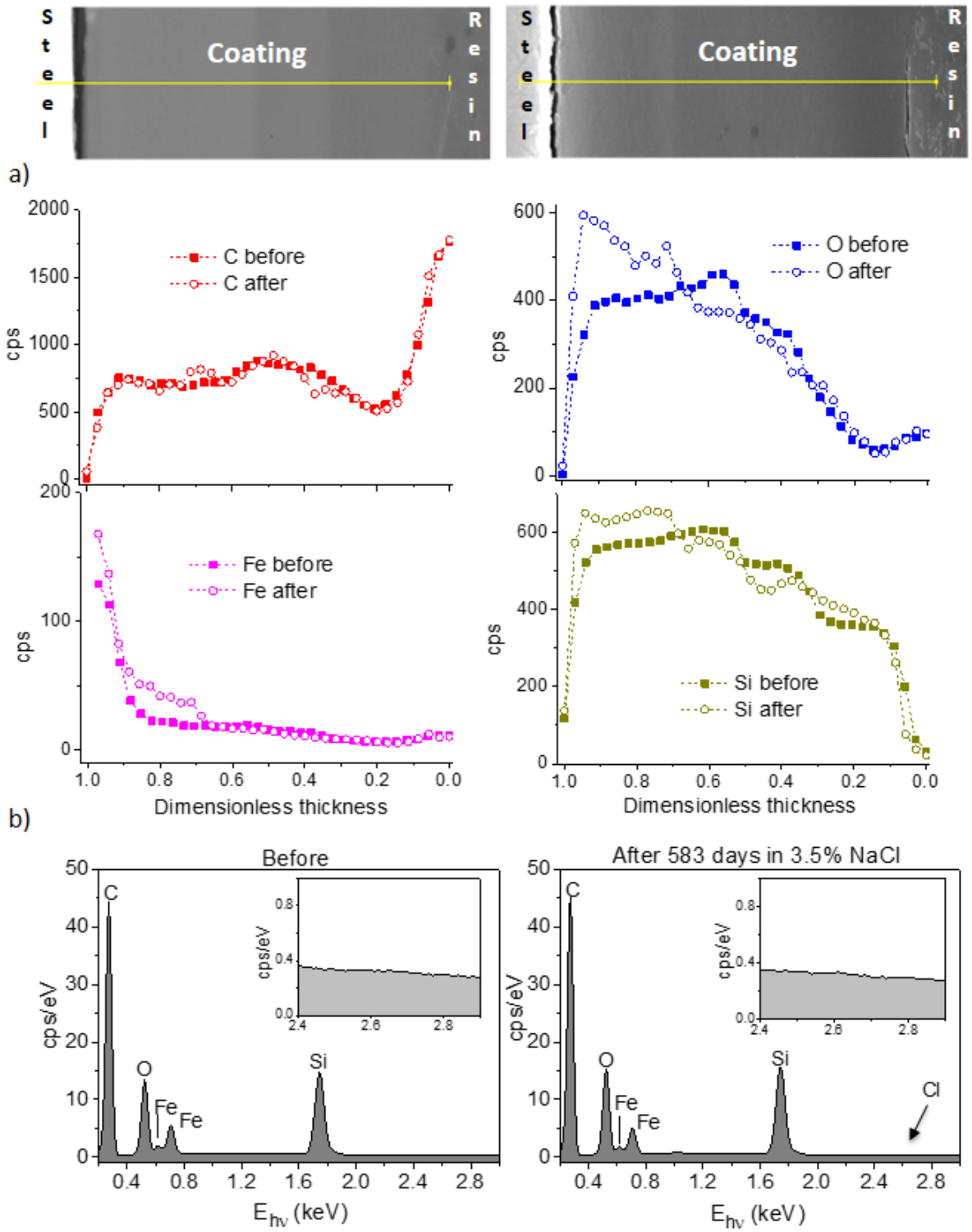

Figure 19. a) EDX cross-section line profiles and b) integrated EDX cross-sectional spectra before and after 583 days of immersion in 3.5% NaCl solution.

Based on these results, which are consistent with the presence of a pristine inner layer, the impedance profiles of the immersed coating were modeled according to

Equation 4, combining in series the parallel RC term of the inner layer, with the Young term of the outer diffusion affected zone, and the electrolyte resistance. By fitting the EIS curves, recorded for the B005 and B010 coatings at different immersion times, the model allowed extraction of the time dependence of relevant physical parameters, such as the sharpness of the conductivity decay (λ), the permittivity of the wet layer (ε_W), the conductivity of the preserved film at the coating/metal interface (κ_f) and its residual thickness (δ). As can be observed in Figure 20 the best-fit curves provided a good agreement between the data and the two-layer model, with a slight deviation of the phase angle in the mid frequency range (~30 Hz). This anomaly, which was more pronounced for the B005 coating, marks a deviation from the quasi-ideal capacitive response and is most probably related to the initial formation of percolation paths within the inner layer of the coating [52,108].

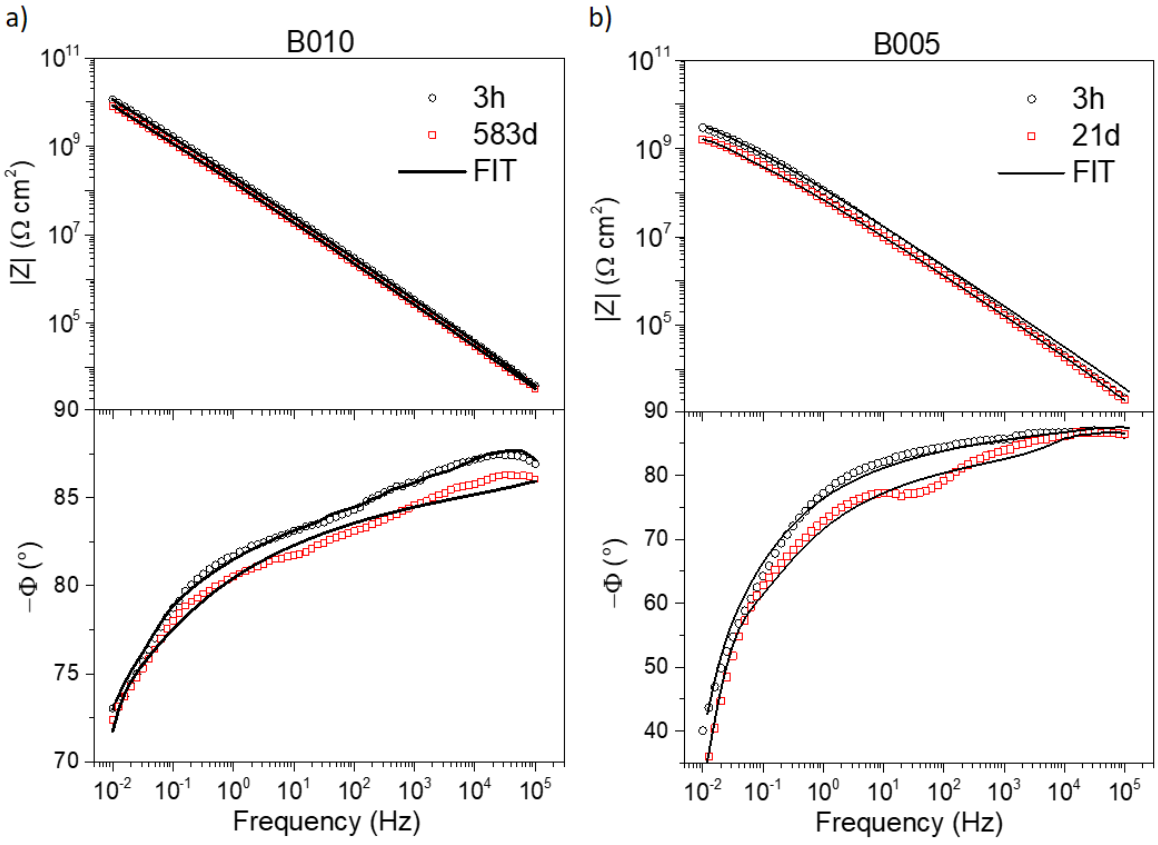

Figure 20. Bode plots for different periods of immersion of PMMA-silica coated steel samples in neutral 3.5 % NaCl: a) B010 coating; b) B005 coating. The symbols represent the experimental data and the solid lines are fits obtained using the two-layer model of Eq. 4 and Figure 8b.

Table 9 shows the obtained fitting parameters for B010 and B005 coatings before and after immersion, including the quadratic error values of the fit. With values in the range of 10^{-2} to 10^{-3}, the chi-square parameter (χ^2) indicate a good quality of the fitting for the two layers model. As expected, only a small increase of the very low conductivity of the inner layer (κ_f) was found for both samples, which is also reflected by the high R_f resistance values. In contrast, for both coatings, the parameters of the uptake zone showed quite different behavior. For the B010 sample, the steep conductivity increase towards the coating/electrolyte interface remains essentially unchanged (small λ), while the B005 sample showed an increase of λ over a much shorter timescale (21 days), indicative of a fast water permeation of the coating. This difference is reflected by the depth of the uptake zone ($d - \phi$), which reached about 16% of the coating thickness for the B010 sample after 583 days, compared to 69% found for the B005 coating after 21 days. Consequently, the permittivity of the latter reached a higher value (22.0), due to the filling of defective zones with water ($\varepsilon_{H2O} \approx 80$). In contrast, for B010, the ε value remained close to that of the hybrid nanocomposite of $\varepsilon \approx 3.7$, obtained by the linear combination of well-known PMMA (3.6) and silica (3.9) values. This result is in agreement with the cross-sectional SEM images, showing that the coating remained essentially unaffected after long-term immersion (Figure 18). Knowing the depth of the uptake zone (d - δ), the conductivity (κ_w) at the coating/solution interface (d) was calculated according to:

$$\kappa_w = \kappa_f exp\left(\frac{d-\delta}{\lambda}\right) \qquad \text{(Eq. 9)}$$

Table 9. Parameters of the two-layer model (Eq. 4) applied to the EIS data of B005 and B010 coatings for different immersion times.

Samples	B005 (3 h)	B005 (21 days)	B010 (3 h)	B010 (583 days)
χ^2	7.4×10^{-2}	1.6×10^{-2}	5.8×10^{-3}	2.7×10^{-3}
λ (μm)	0.15	0.27	0.07	0.09
ε_w	10.5	22.0	4.09	6.65
κ_f (fS cm^{-1})	46.5	202.0	1.4	6.9
κ_w (nS cm^{-1})	17.1	54.7	4.7	139
δ (μm)	2.54	1.56	8.61	8.10
$d - \phi$ (μm)	4.72	2.88	8.62	8.40
R_f (GΩ cm^2)	1.7	0.8	23.2	10.3
C_f (nF cm^{-2})	30.8	42.4	11.0	12.7
R_s (Ω cm^2)	37	33	44	40

The comparison of conductivities of the inner layer (κ_f) and of the coating/electrolyte interface (κ_w) showed that for both samples the latter was between 5 and 7 orders of magnitude higher (Table 9). A similar result obtained using the Young model was reported for 20 μm thick epoxy-polyaminoamide films deposited on AA2024 aluminum alloy [50]. Figure 21a shows a comparison of the conductivity profiles for different immersion times of samples B005 and B010, calculated according to Eq. 9 using the parameters of Table 9. The almost unchanged conductivity profile of B010 contrasts with that of B005, with the latter showing the continuous expansion of the Young zone towards the coating/steel interface.

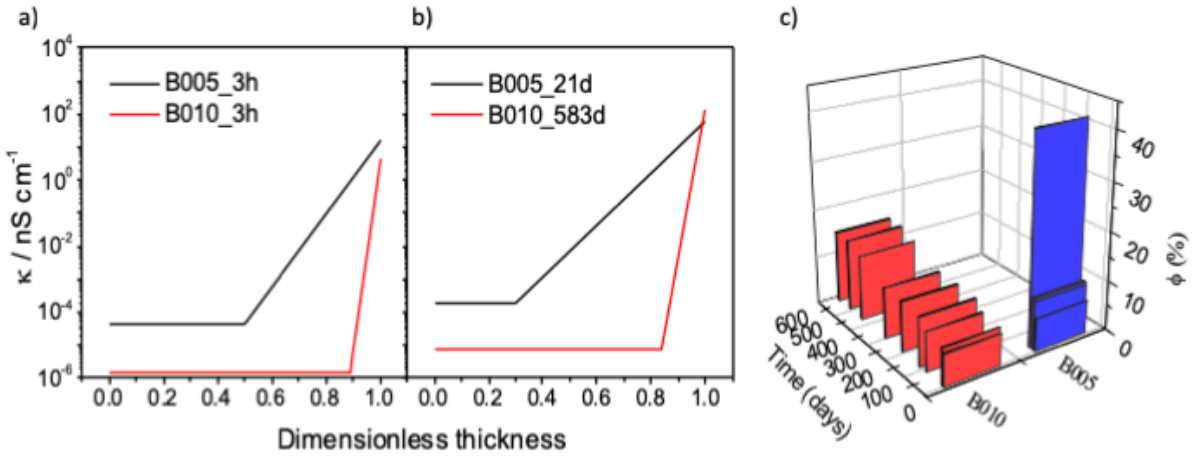

Figure 21. Profiles of conductivity vs. dimensionless thickness for different immersion times in 3.5% NaCl: a) after 3 h; b) after 21 and 583 days for B005 and B010 coatings, respectively; c) Time dependence of water uptake of the two coatings.

The best-fit results obtained using the EEC/CPE and the two-layer models clearly showed that the propagation of the electrolyte along the normal axis affected the structure of the external layer, resulting in a pronounced resistance drop for both samples, although the rates of the decreases had different timescales. The superior performance of the B010 coating can be explained by its improved structural characteristics, as revealed by the Raman and thermal analyses. Comparing the time evolution of the electrical quantities, the two models showed similar trends for resistances and capacitances (Table 8 and Table 9). For the B010 sample, the two resistances (R_f and R_2) of the inner layer are similar, while a slightly greater deviation was found for the capacitances. In order to compare the inner layer thickness of the two models, the water uptake volume percentage (ϕ) (Figure 21b) was calculated using the Brasher-Kingsbury relation [105,110] and the obtained CPE parameters (Table 8). Expressing ϕ as the average uptake penetration depth, the results showed that for the B010 sample ($d - \phi$) and δ values of both models are in very good agreement (Table 9). Moreover, the effective parallel plate capacitances obtained using the dielectric constants of the Young model were used to calculate the water uptake values for both coatings after 583 (B010) and 21 (B005) days of immersion [111]. The obtained penetration of 11% for B010 and 16% for B005 sample contrast with those determined using the Brasher-Kingsbury equation (13 and 42%) and the Young model (16 and

69%), especially for B005 coating, indicating a limited validity of capacitances derived from the parallel plate model.

On the other hand, greater divergence has been found for the B005 coating with the inferior corrosion protection performance. In several studies [47,50,110,112]; two different approaches have been used to extract most reliable water uptake values: (i) the Brasher-Kingsbury equation, including the Q value of the CPE, and the (ii) the "power-law model", although an inaccurate knowledge of the coating resistivity has a large impact on the resistivity of the electrolyte, leading to erroneous values for the water uptake [107]. Consequently, the two approaches may not generate very reliable water uptake volume percentages, since the first considers only a single RC element, while neither account for the differences in the diffusion rates of ions and water in the coating [50,110]. Indeed, discrepancies were also found between the values of water uptake using Brasher-Kingsbury equation and other techniques such as gravimetric methods. These differences come from capacitance calculation that does not depend only on the amount of water, but on the way water permeates the coating [111]. A higher formation rate of micropores in the uptake zone of the B005 coating might account for the thickness divergence between the models. The inclusion of a pore resistance (R_{pore}) was evaluated by using the extended binary layer model, as suggested by Nguyen et al. [113]. Compared with the experimental data, the simulated impedance curves showed a slightly improved accuracy ($\chi^2 < 10^{-2}$). However, apart from small increase of permittivity and resistance, no significant changes of the extracted parameters were observed, as can be observed for the fitting of the B005 coating (Figure 22). This is in agreement with pycnometry results suggesting a pore-free structure.

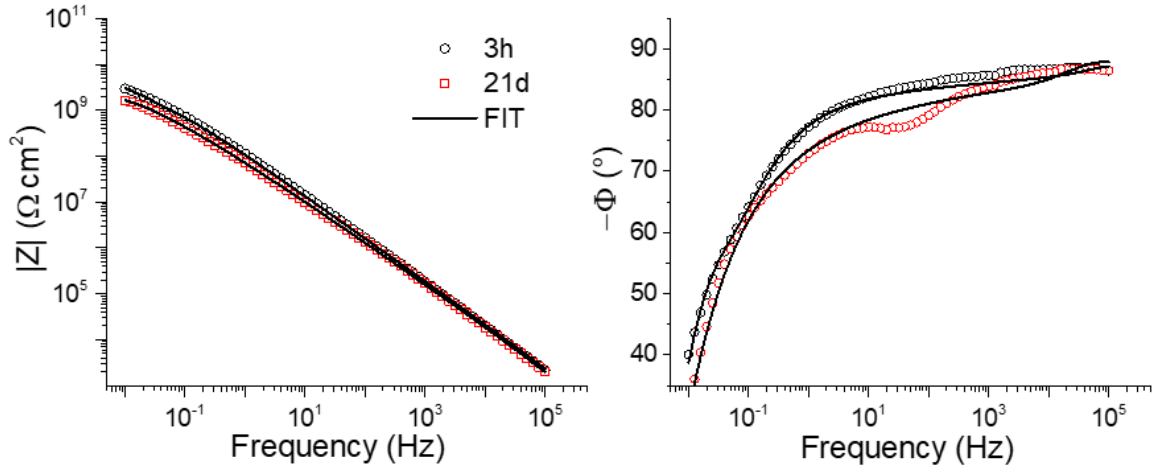

Figure 22. Bode plots after 3 h and 21 days of immersion in 3.5 % NaCl of B005 and fits obtained using the two-layer model including a pore resistance term [113].

The results suggest that the two-layer approach based on the Young model is a method well-suited to describes the electrochemical behavior of high performance PMMA-silica coatings. In addition to the commonly applied CPE model, it can be applied to impedance data, enabling extraction of the time dependence of conductivity profiles and other important quantities (δ, ε, λ), essential for describing of an inhomogeneous electrolyte uptake through a dense barrier. The model might be also valid for coatings with inferior corrosion protection performance, during the initial stages of immersion.

In a recent work [40], a comparable long-term stability (>300 days) of high impedance coatings has been reported for PMMA-silica coatings modified by Ce(IV) ions. It was suggested that the decrease of the impedance modulus after long-term exposure was primarily caused by the uptake-induced roughness of the surface layer, involving the formation of nanopits with an average size of about 250 nm during the final stage of the coating lifetime. Hence, the expansion of a microporous uptake layer towards the coating/steel interface might be the principal mechanism responsible for the long-term deterioration of high impedance hybrid coatings.

The remarkable corrosion protection performance of the PMMA-silica coatings is a consequence of the synergic effect of the two phases, forming a densely packed hybrid structure of very low porosity, which acts as a very efficient diffusion barrier with an impedance response close to that of an ideal capacitor. This was achieved by

careful tuning of the synthesis parameters, resulting in a nanocomposite formed by silica nanodomains covalently interconnected by short PMMA chain segments [31]. In addition, the high durability of the coating was favored by the hydrophobic character of the dominant polymeric phase (>70%), together with the strong adhesion of the films to the metallic substrate.

1.3 Conclusions

Thin (2–10μm), transparent (80–90% transmission) and adherent (9–26MPa) PMMA-silica coatings on carbon steel were prepared by varying the thermal initiator to methacrylate ratio (BPO/MMA) between 0.01 and 0.10. Raman spectroscopy and thermogravimetric analyses showed that the increase of the BPO/MMA ratio to 0.10 improved the polymerization efficiency, as evidenced by the suppression of the vinyl vibrational band and stacking defects of the PMMA chains, respectively. Based on EIS assays, coatings prepared using a BPO/MMA molar fraction of 0.10 presented the best anticorrosive barrier property, presenting with low-frequency impedance modulus of up to 2.4 GΩ cm^2 μm^{-1}, which remained almost unchanged after more than 580 days of immersion in 3.5% NaCl solution. Cross-sectional elemental profile analysis confirmed the absence of chlorine in the bulk of the best performing coating, after long-term immersion. Modeling of the EIS curves using the two-layer Young model evidenced a very slow electrolyte uptake by the hybrid coating, which can be described by an exponential decay of conductivity towards the coating/steel interface. All these results suggest that PMMA-silica coatings represent an interesting alternative to conventional corrosion protection systems.

Chapter 2[b]: Dual role of lithium on the structure and smart corrosion inhibition of PMMA-silica coating

2.1 Structural properties

A dense and highly cross-linked hybrid structure is essential to provide an elevated barrier property for the coating. In a previous study, it was shown that only a structure of homogeneously distributed silica nanodomains covalently conjugated with a highly polymerized matrix leads to a dense reticulated hybrid network that prevents the formation of permeation paths by the contact with the electrolyte [31]. To get information on the nanostructural properties of samples with different lithium content, SAXS profiles were recorded and fitted according to models of Porod and Guinier [40,82,83] allowing to extract the Porod coefficient (α) and the radius of gyration (R_g) (Table 10). The change of the SAXS profiles displayed in Figure 23a evidences significant modifications in the hybrid nanostructure for higher lithium loadings. The SAXS profiles of Li0 and Li05 samples present a correlation peak indicative for a concentrated set of silica domains [31] with an average spacing that increases from 3.3 nm to 4.0 nm with the addition of 500 ppm of lithium (Figure 23b). Further addition of lithium (Li1 and Li2), however, leads to a vanishing correlation peak due to the presence of a more diluted set of larger silica domains with fractal morphology ($\alpha \approx 2$). While for the Li1 sample the well-defined Guinier regime (plateau and Gaussian decay) at mid q-range is characteristic for silica particles with average size (R_g) of about 1 nm, the profile of the Li2 hybrid, showing a linear decay over almost the entire q-range, points to the formation of diluted set of larger silica particles ($R_g \sim 3$ nm), uniformly distributed in the PMMA matrix (Table 10).

---

[b] This chapter is adapted from the accepted scientific paper:
A. Trentin, S.V. Harb, M.C. Uvida, S.H. Pulcinelli, C.V. Santilli, K. Marcoen, S. Pletincx, H. Terryn, T. Hauffman, P. Hammer. *ACS Applied Materials & Interfaces*, doi: 10.1021/acsami.9b13839.

Additionally, the increase of the scattering intensity in the low q-range, observed for Li0 and more pronounced for the Li05 sample, hints on the presence of large silica heterogeneities in the hybrid matrix, while the flatter profile found for hybrids with higher amount of lithium (Li1 and Li2) is indicative for a diluted monomodal distribution of silica nanoparticles embedded in the PMMA matrix, as represented in the idealized structural model of Figure 23c. The improved homogeneity of the latter hybrid structure is considered to be more favorable to form a diffusion barrier that effectively inhibits the penetration of corrosives species. This is due to the reticulating effect of a uniform distribution of the silica nodes, which reduces the porosity by contraction of the PMMA chain segments [31].

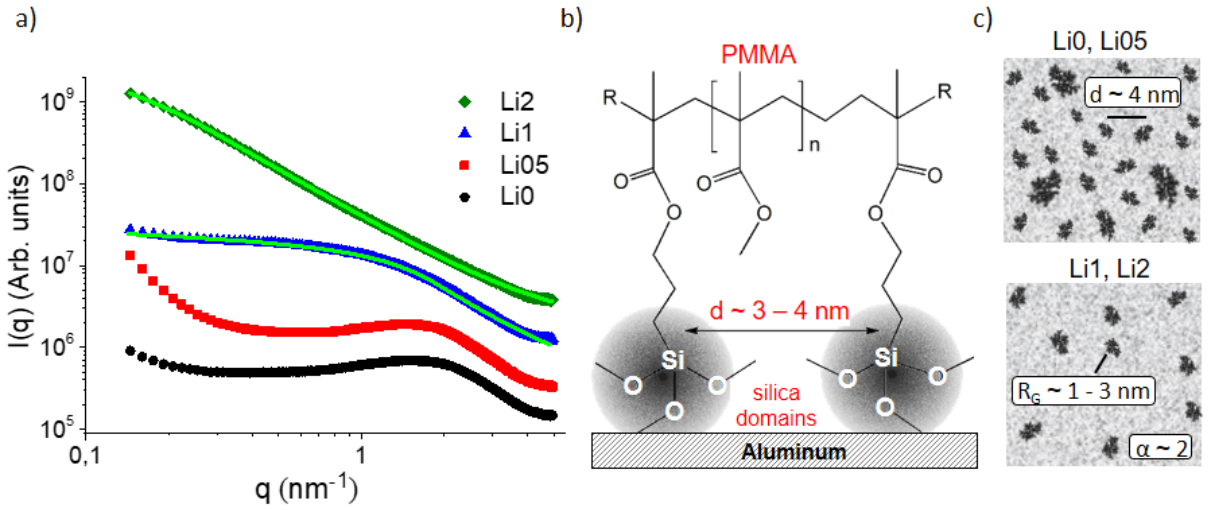

Figure 23. a) SAXS intensity profiles of the hybrids prepared with different concentrations of Li_2CO_3 fitted according to the Guinier-Porod model (green lines), b) structural representation of Li0 and Li05 PMMA-silica hybrids, c) idealized structure of silica clusters distribution in the amorphous polymeric matrix for different lithium concentrations.

In agreement with the R_g values obtained by SAXS, the analysis of AFM maps showed that the RMS roughness increases with the addition of lithium from 1.1 nm to 3.3 nm. The transparent films have a thickness between 4 µm and 6.3 µm and present an excellent adhesion to the aluminum substrate reaching a critical pull-off force of up to 28.6 MPa for coatings with higher Li loading (Table 10). The values, listed in Table 10, are significantly higher than those previously reported for epoxy-silica coatings on magnesium alloy (AZ31), mild steel and aluminum (AA5083) with 17.3, 3.0 and 4.7

MPa, respectively [95–97]. It is worth pointing out that strong adherence is essential for efficient corrosion protection in terms of long-term stability of the coatings.

Table 10. Properties of PMMA-silica-lithium hybrids: film thickness obtained by optical interferometry and cross-section SEM images; surface roughness extracted from AFM images; adhesion to the substrate determined by pull-off test; radius of gyration (R_g), Porod power law exponent (α) and correlation distance (d), determined by SAXS; decomposition on-set temperature (T_s) and residue, extracted by TGA; polycondensation degree of the inorganic phase (C_d) obtained by NMR. *Experimental error: ± 0.5.

Sample	Thickness (μm)	RMS roughness (nm)	Adhesion (MPa)	R_g (nm)	α	d (nm)	T_s (°C)	Residue (%)	C_d (%)*
Li0	4.0	1.1	17.9	-	-	3.3	205 ± 23	18 ± 1	88.6
Li05	5.3	0.8	18.6	-	-	4.0	224 ± 10	19 ± 2	87.6
Li1	5.8	2.2	28.6	1.0	2.1	-	237 ± 10	21 ± 0.5	88.8
Li2	6.3	3.3	24.0	3.1	1.9	-	231 ± 7	20 ± 0.5	90.2

An indicative for the degree of the overall connectivity of the hybrid network can be derived from thermogravimetric analysis (TG and DTG - derivative curves) by studying the degradation events of hybrid monoliths in nitrogen atmosphere (Figure 24a and Figure 24b). The experiments, performed in triplicate, allowed to estimate the thermal stability of the hybrids, as the on-set temperature of degradation at 5% mass loss (T_s), the degradation events of the polymeric phase (DTG) and the residual mass, corresponding to the percentage of the silica phase at 800 °C. Although the T_s values presented large variation, the addition of lithium improved the thermal stability of the hybrids (Table 10) and as expected, a similar fraction of residual silica between 19 and 21% (Figure 24a). The addition of lithium resulted in a slight increase of the thermal stability, which was more pronounced for Li1 sample (Table 10). The analysis of degradation events (DTG) showed that samples containing lithium exhibited strongly suppressed decomposition events related to the breaking of head-head stacking defects (T_1) and unsaturated PMMA chain-ends (T_2) [92], indicating a more efficient polymerization of PMMA (Figure 24b). In addition, the temperature of complete PMMA degradation (T_3) [92] increased with the addition of Li from 392 °C (Li0) to 409 °C (Li2), suggesting higher structural stability of the lithium containing polymeric network (Figure

24b). Both effects evidence the role of Li as structural modifier of the organic-inorganic structure, as already suggested by SAXS results. The findings indicate that lithium addition in the range of 1000 to 2000 ppm provides increased connectivity of the hybrid network formed by a homogeneous distribution of silica nodes covalently linked to a highly polymerized PMMA matrix.

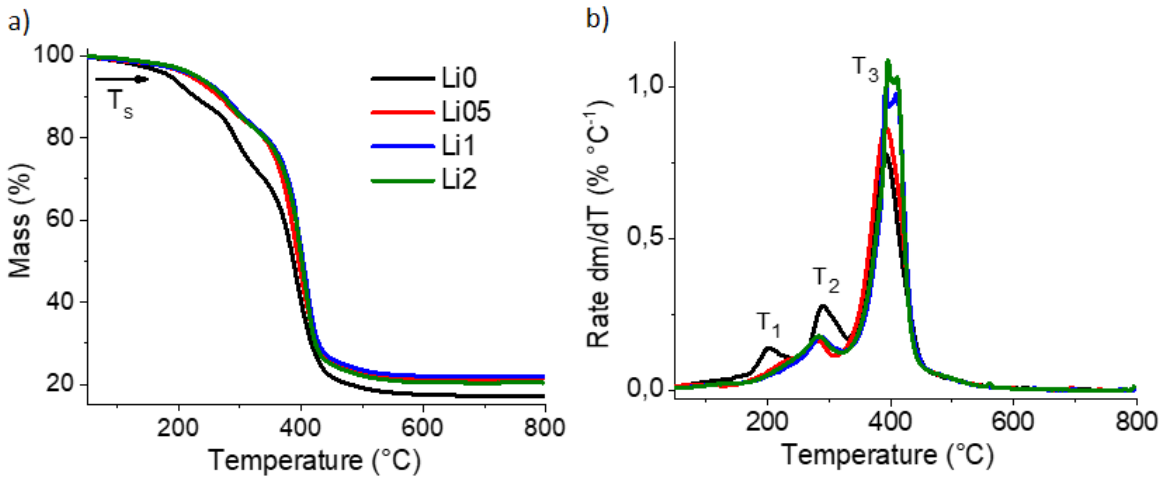

Figure 24. a) Thermogravimetric curves (TG) and b) differential thermogravimetric curves (DTG) of PMMA-silica hybrids prepared with different concentrations of lithium carbonate.

The local bonding structure of the silica phase was studied using ^{29}Si nuclear resonance spectroscopy. The polycondensation products of TEOS and MPTS appear as broad resonance peaks in Figure 25, denoted as T^J and Q^J, respectively, where the structural units of TEOS correspond to Q^2 ($Si(OSi)_2(OR)_2$, R = H or CH_2CH_3), Q^3 ($Si(OSi)_3(OR)$) and Q^4($Si(OSi)_4$) and MPTS units are assigned to T^1 ($–CH_2Si(OSi)(OR)_2$, R = H or CH_3), T^2 ($–CH_2Si(OSi)_2(OR)$) and T^3 ($–CH_2Si(OSi)_3$). The relative peak intensities of each T^J and Q^J component were determined from the spectra by a peak fitting procedure using a combination of Gauss/Lorentz functions. The polycondensation degree (C_d) of the silica domains was calculated from relative peak areas of T^J and Q^J species using the equation 7.

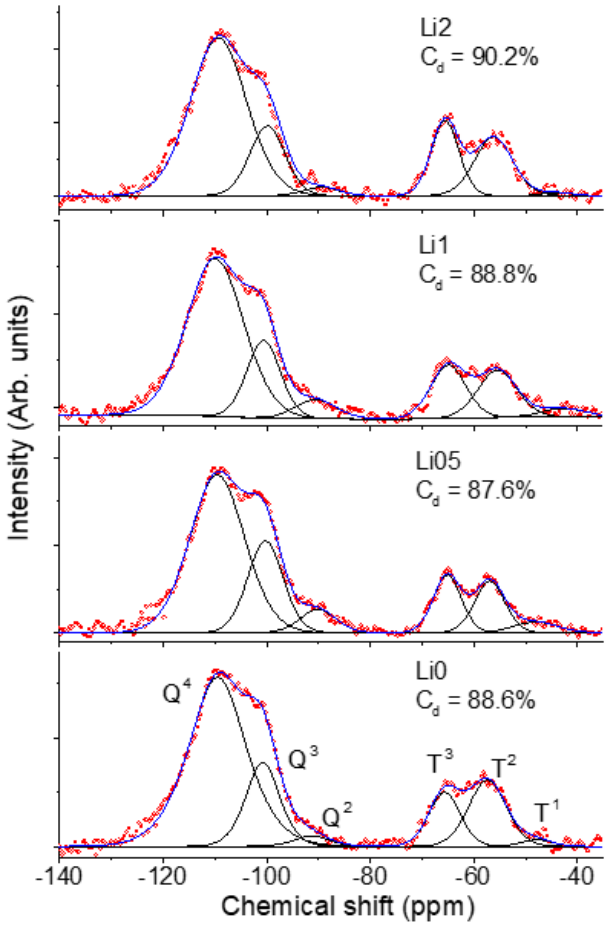

Figure 25. ^{29}Si NMR of PMMA-silica hybrids prepared with different concentrations of Li_2CO_3.

The polycondensation degree (C_d) values extracted from the spectra for all samples were in the range of 88.6±0.5% (Li0) to 90.2±0.5% (Li2), indicating a small increase of the connectivity of the inorganic phase for samples containing higher Li amount, mainly associated to the increase of T^3 species of the MPTS polycondensation product. It is interesting to note that these C_d values are about 5% higher than those recently reported for pure PMMA-silica hybrids [31] and slightly higher than the best value (87%) achieved by cerium doping of this material [40].

From the results of the structural analysis, it can be concluded that lithium addition induces a homogeneous distribution of highly condensed silica nodes embedded in PMMA matrix that improves the connectivity of the hybrid network, an essential prerequisite for a coating with elevated barrier property. This is supported by the recently reported role of lithium as a network modifier [114,115]. Based on these

studies, the structural improvement of the hybrid is driven by lithium induced changes in form of (i) lithium complexation with MMA monomers causing chain growth after rearranging the unsaturated bonding ends [114], and (ii) change of the condensation kinetics of the silica network resulting in higher condensation rate of free silanols, which are charge balanced by the presence of Li^+ [115].

2.2 Active corrosion protection of intact coatings

Besides the beneficial effects of lithium on the structural properties, its uniform distribution in the coating is essential for an active corrosion protection of metallic surfaces. Figure 26 shows the SEM cross-section view of the Li1 coating after 310 days of immersion in 3.5% NaCl solution and the corresponding ToF-SIMS mass spectra maps, obtained for Li^+ and $C_2H_3O_2^+$ secondary ion fragments, along with the EDS cross-section elemental profiles of Li1 and Li0 samples. The SEM image confirmed the thickness of the Li1 coating of 5.8 µm (Figure 26a) and SIMS results evidence a homogeneous distribution of lithium and carbon in the entire coating (Figure 26b), even after long-term exposure to the saline environment. The cross-section elemental line scans of Li1 and Li0 coatings confirmed the nominal composition of the coatings (59 wt % C, 29 wt % O and 12 wt % Si), also in agreement with the mass fraction of the silica residue obtained from the thermal analysis. It is interesting to note for both coatings the existence of a Al enrichment zone close to the aluminum/coating interface suggesting the presence of an interfacial diffusion layer, which might explain the elevated adhesion of the coatings [37].

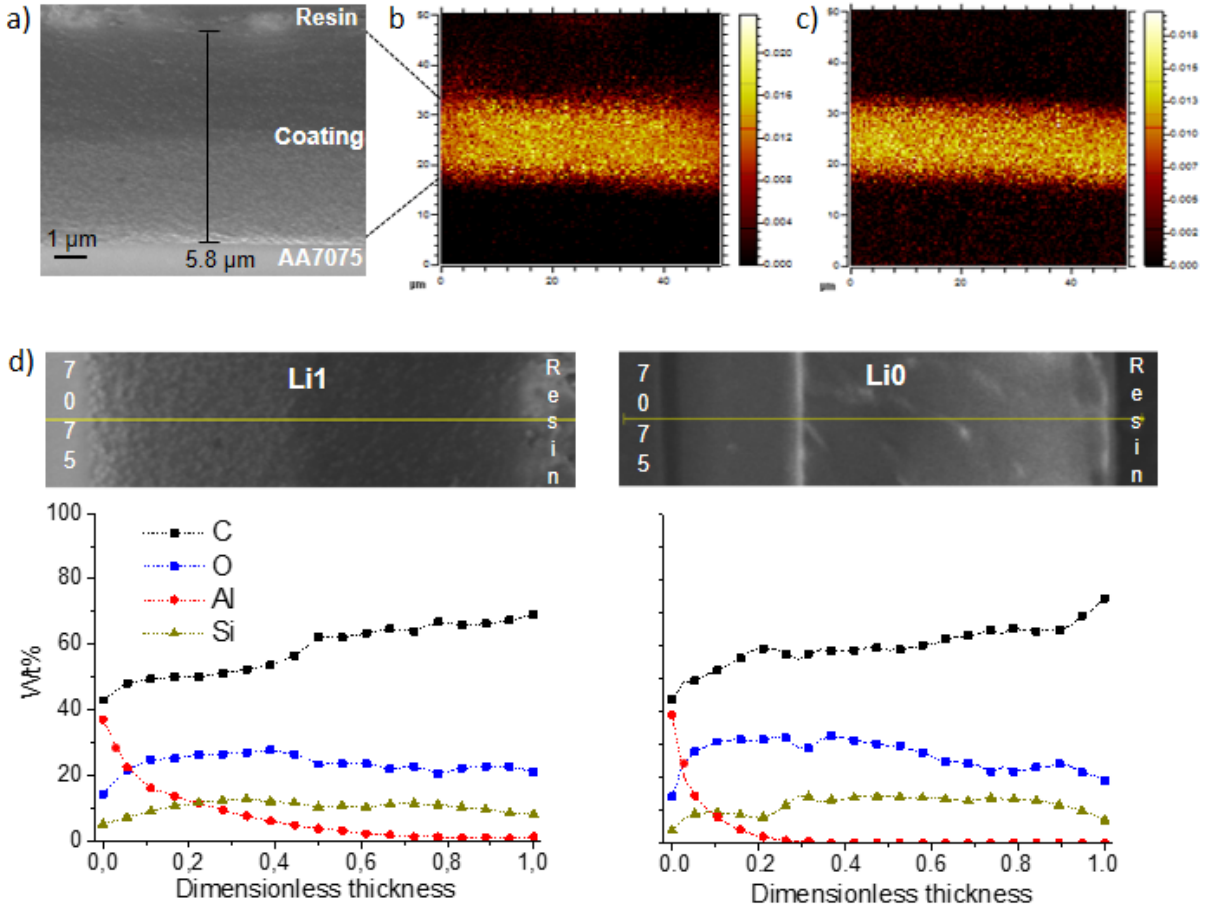

Figure 26. a) SEM image of Li1 cross section after 310 days of immersion in 3.5% NaCl, b) ToF-SIMS map of Li^+ normalized to total, c) $C_2H_3O_2^+$, a PMMA fragment normalized to total, and d) EDS elemental profiles of Li1 and Li0 cross sections for C, O, Si and Al.

For all coatings, electrochemical impedance spectroscopy (EIS) measurements were performed in a 3.5% NaCl solution in regular time intervals of 7 days. Bode plots recorded after 3 h of immersion (Figure 27) revealed that the coatings present elevated anticorrosive performance with an impedance modulus up to six orders of magnitude higher than bare aluminum alloy and a quasi-ideal capacitive behavior with a phase angle close to -90° extending over a frequency range of 7 decades. This performance is comparable with the best anticorrosive coatings reported so far [40,41,52,116]. As shown in Table 11, the Li0, Li05, Li1 and Li2 coatings showed after 3 h exposure a low frequency impedance modulus ($|Z_{lf}|$ thickness^{-1}) of 2.9, 9.4, 3.2 and 0.8 GΩ cm^2 µm^{-1}, respectively. The observed normalized Z_{lf} values reveal the trend of a superior protection achieved at intermediate concentrations of Li (500 – 1000 ppm), and even

though they vary to some extent, a reproducible behavior of PMMA-silica coatings with impedance modulus in the GΩ cm^2 range was achieved, regardless of the amount of inhibitor added. Although the initial value was lowest for the Li2 sample, after 30 days of immersion the coating containing higher lithium amount (Li1 and Li2) showed a smaller decrease ($|Z|_{3h}$ / $|Z|_{30d}$) of the corrosion resistance (Table 11), an effect that might be related to the improved structural properties, discussed before.

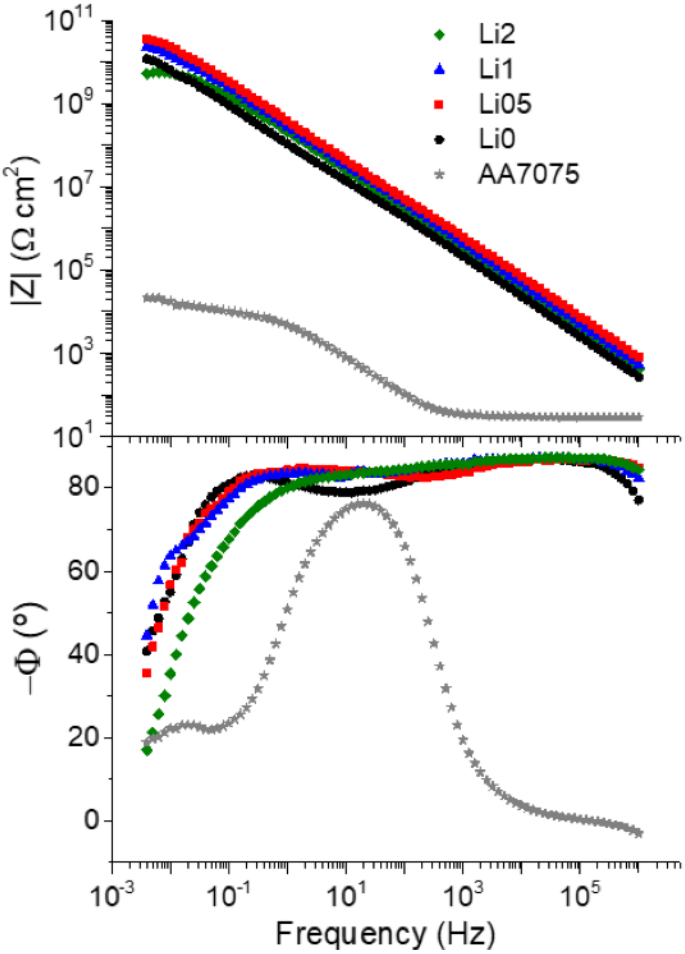

Figure 27. Bode plots of the hybrid coatings modified with different concentrations of lithium after 3 h of immersion in 3.5% NaCl solution.

Table 11. Impedance modulus at low frequency ($|Z|_{lf}$) after 3 h and 30 days of immersion in 3.5% NaCl, normalized by the thickness; $|Z|_{3h}/|Z|_{30d}$, E_{OC} after 3 h and time until the first failure event occurs.

Sample	$\|Z_{lf}\|$ thickness^{-1} ($G\Omega\ cm^2\ \mu m^{-1}$)		$\|Z\|_{3h}$ / $\|Z\|_{30d}$	-(E_{OC})	1st failure event (days)
	3 h	30 days		(mV/Ag/AgCl)	
Li0	2.9	0.5	5.8	899	70
Li05	9.4	1.5	6.2	516	50
Li1	3.2	1.5	2.1	770	99
Li2	0.8	0.4	2.0	827	142
AA7075	$2.1x10^{-5}$	-	-	729	1

Figure 28 displays the time dependence of the impedance modulus and phase angle for the Li1 coating. After the local failure of the coating after 99 days, visible as an impedance drop of 2 orders of magnitude, the impedance profile was almost entirely restored after 126 days. The appearance of a second pit after 154 days caused a new decay of the impedance modulus of about 4 decades, which was partially restored (183 days) and remained essentially stable until 310 days of immersion. This notable finding is related to the self-healing ability of the coating induced by the chemical activity of Li species in the corrosion affected zones restoring the coating in pit affected area. Concerning the phase angle behavior, the high-frequency range of the phase angle is generally assigned to the capacitance and resistance of the coating, while the time constant at about 10 Hz accounts for the aluminum passive layer and that at about 10^{-2} Hz to the charge transfer processes at the interface [56,64,117]. Consequently, the diffusion of corrosive species towards the coating/aluminum interface leads to a continuous drop of the phase angle, which is more pronounced at low frequencies. This localized corrosion process at the interface is accompanied by a phase angle depression in mid-frequency range, known as anomaly, occurring as a consequence of the formation of conductive percolation paths within inner layer of the coating [52,108]. The lithium induced restoration process at the coating/aluminum interface can be clearly noted after 126 and 183 days of immersion, marking a recovery of the capacitive behavior of the phase angle at low frequencies and to some extent also in the mid-frequency range.

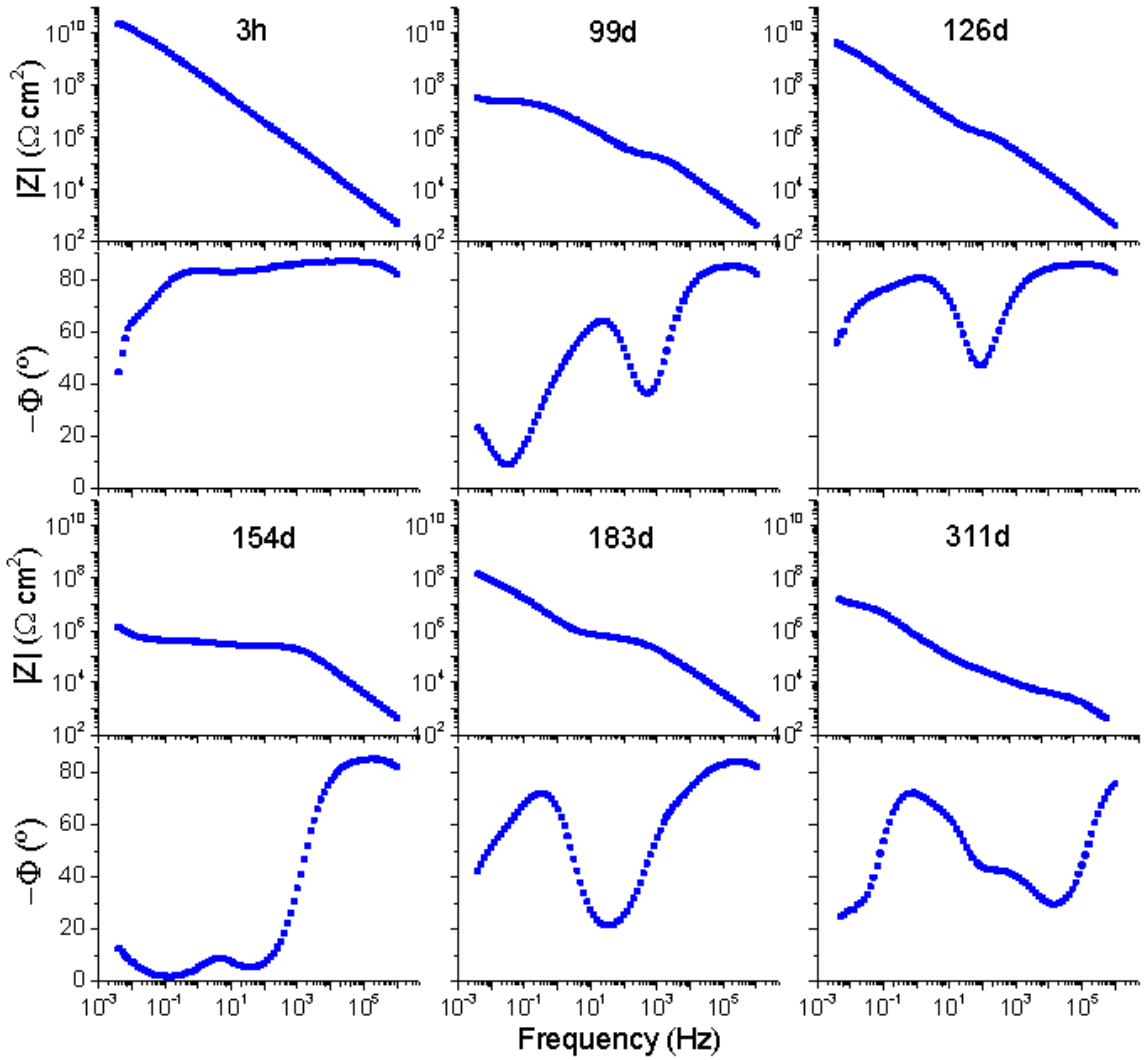

Figure 28. Time evolution of impedance modulus and phase angle plots for the Li1 coating immersed in 3.5% NaCl solution.

The reversible process observed in Figure 28 for the coating containing 1000 ppm of lithium can be related to redox reactions taking place in the localized defect at coating/substrate interface. As soon as water, oxygen and aggressive chloride ions reach the substrate, the Cl^- ions form a complex with aluminum producing soluble Al compounds, which cause the pit acidification/ propagation at the coating/aluminum interface. Simultaneously, at the top of the defect, $Al(OH)_x$ starts to precipitate at higher pH as a consequence of the reaction with OH^- from cathodic oxygen reduction reaction and carbonate activity (Reactions 6, 19 and 20), leading to the formation of corrosion products [12,13,77]. The curing activity of lithium within the pit is triggered at higher pH

by the formation of Li^+ containing hydrated $Al(OH)_x$ phase with a highly passive character [55,76,78,80,118]. This is evidenced by the absence of a charge transfer process at the interface, as observed in Figure 28 after 126 and 183 days of immersion. In this model, the partially recovering of the capacitive behavior in the mid-frequency range can be related to the filling of water percolation paths formed within the coating.

This self-regeneration process was identified for all Li loaded coatings, as evidenced by the dependence of the open circuit potential (E_{OC}) and the low frequency modulus ($|Z|_{lf}$), recorded during 310 days of immersion (Figure 29). The analysis of the data after pitting revealed several important features of the lithium activity at different Li loadings: (i) for all samples the time dependence of $|Z|_{lf}$ presents a similar trend as E_{OC}, showing a clear correlation between both quantities; (ii) after a local failure of the coating, an impedance drop occurred, followed by a gradual recovery of $|Z|_{lf}$ of about two orders of magnitude within 40 days (Li05), 28 days (Li1) and 20 days (Li2), indicating a faster regeneration with increasing Li content; and (iii) a higher lithium concentration delayed the appearance of localized corrosion, maintaining $|Z|_{lf}$ stable for 50 days (Li05), 99 days (Li1) and about 140 days (Li2), compared to 70 days observed for Li0.

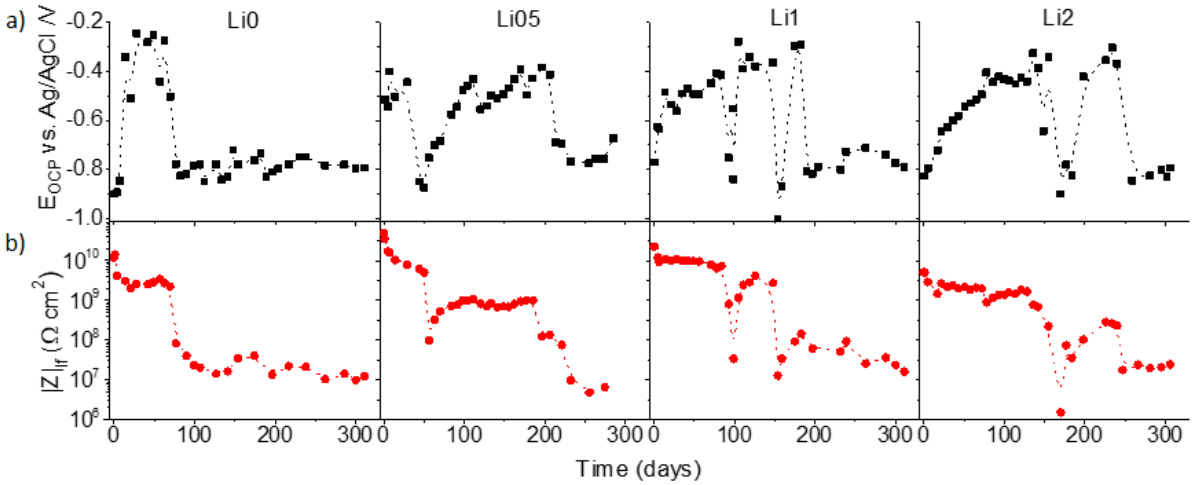

Figure 29. a) Time evolution of E_{OC} and b) $|Z|_{lf}$ for coatings modified with different amounts of lithium during 310 days of immersion in 3.5% NaCl solution.

According to Figure 29b, samples modified with higher amounts of lithium salt maintained elevated values of $|Z|_{lf}$ over longer immersion periods and restored faster

after pitting. The acidic environment in the pit might be the cause of the low E_{OC} value of about -0.85 V, observed for the coatings after local failure (Figure 29a), which is about 0.1 V lower than that determined for bare aluminum alloy in 3.5% NaCl solution (Table 11).

To obtain more information on the regeneration mechanism of lithium containing coatings, detailed surface and cross-sectional analysis in the defective zones have been performed by SEM/EDS and ToF-SIMS. For the pit located in the center of the contact area of the Li1 coating (Figure 30c) overlay SIMS maps of Li^+, $C_2H_3O_2^+$ and Al^+ ions are displayed in Figure 30a. Small spots of lithium can be noticed right in the pit center (red) surrounded by aluminum (blue) and further by the coating ($C_2H_3O_2^+$, a PMMA fragment (green)). The accumulation of lithium in the pit is evident from the Li^+ map of Figure 30b showing much smaller intensity of lithium contained in the surrounding coating. Moreover, larger Li^+ map, recorded close to the edge of the immersed zone (Figure 30d), revealed that due to their mobility Li^+ ions have been leached from the coating into the solution during the immersion.

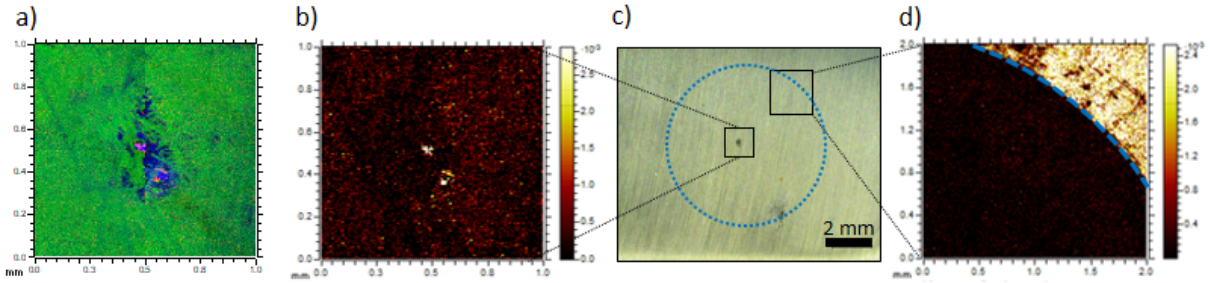

Figure 30. ToF-SIMS maps and optical micrograph of the Li1 coating recorded after 310 days of immersion in saline solution: a) overlay of Li^+ (red), $C_2H_3O_2$+ (green) and Al^+ (blue), b) normalized Li^+ (yellow) map, c) optical micrograph displaying the immersed area delimited by a blue dashed circle, and d) normalized ToF-SIMS map of Li^+ (yellow) at the edge of the immersed zone.

The cross-sectional view of the central pit of Li1 coating is shown in Figure 31a. The pit has a nearly conical shape and penetrates the aluminum substrate to a depth of about 70 µm and, as consequence of the corrosive attack, the delaminated coating around the pit forms debris of cathodic deposits. After electrolyte permeation through percolation paths in the PMMA−silica coating and the rupture of the passive oxide layer, the preferential attack occurs at intermetallic sites of Cu and Zn, intermetallics used to improve the hardness of A7075 alloy (Figure 31a, inset).

Cross-section SIMS maps showed that the lower part of the pit is mainly composed of $AlOH_x$ corrosion products (Figure 31b), in agreement with previous studies [56,76], however in the present study, a lithium containing top layer was found (Figure 31c). This is a clear evidence of the high mobility of lithium ions, which diffuse from the adjacent coating and accumulate in the defective zone under the formation of a protective layer. XPS analysis, performed with a lateral resolution of 50 μm in the top and bottom zone of the pit, confirmed the SIMS findings revealing a Li concentration of 31 at.% and 22 at.%, respectively. The deconvoluted high-resolution Li 1s spectra identified two spectral components assigned to the presence of Li_2O and/or $LiAlO_2$ phase at 55.5 eV and possibly Li^+ containing AlO(OH) (pseudoboehmite) species at about 54.0 eV (Figure 31d) [62,93].

Moreover, the presence of lithium oxides and aluminum hydroxide species was confirmed for both positions as the most intense component from the analysis of the high-resolution O 1s spectra. Hence, the results of two complementary techniques confirmed the formation of Li containing protective aluminate oxide/hydroxide layer in the pitting zone. SIMS surface maps suggest that at least a fraction of lithium ions was leached from the nearby coating surface, migrated to active corrosion sites to form a protective barrier layer inside the pit, which inhibited the redox reactions and consequently led to the recovery of the $|Z|_{lf}$ and E_{OC}.

Based on studies reporting on the pitting process of aluminum alloys and results obtained in this work, a mechanism for the self-healing activity of lithium ions in active corrosion spots of PMMA-silica coatings is proposed. Figure 32 depicts in cross-sectional view the main stages of the pitting process under the presence of lithium ions as corrosion inhibiting agents. During the contact with saline solution, dissolved oxygen slowly oxidizes the hybrid coating creating local structural defects [36]. At this stage, the barrier properties of the material provide efficient protection for the substrate against the corrosive attack due to the dense hybrid structure containing low quantity of defects, as supported by SAXS, TGA and NMR results obtained for coatings with higher Li content. After long-term exposure, water percolation paths containing aggressive species start to corrode the passive layer and reach the alloy causing the

formation of soluble chloride complexes with Al^0, while the pH drops to 3 - 4 at the base of the pit due to aluminum hydrolysis [12,13]:

$$Al^{3+} + 3H_2O \rightarrow Al(OH)_3 + 3H^+ \qquad (22)$$

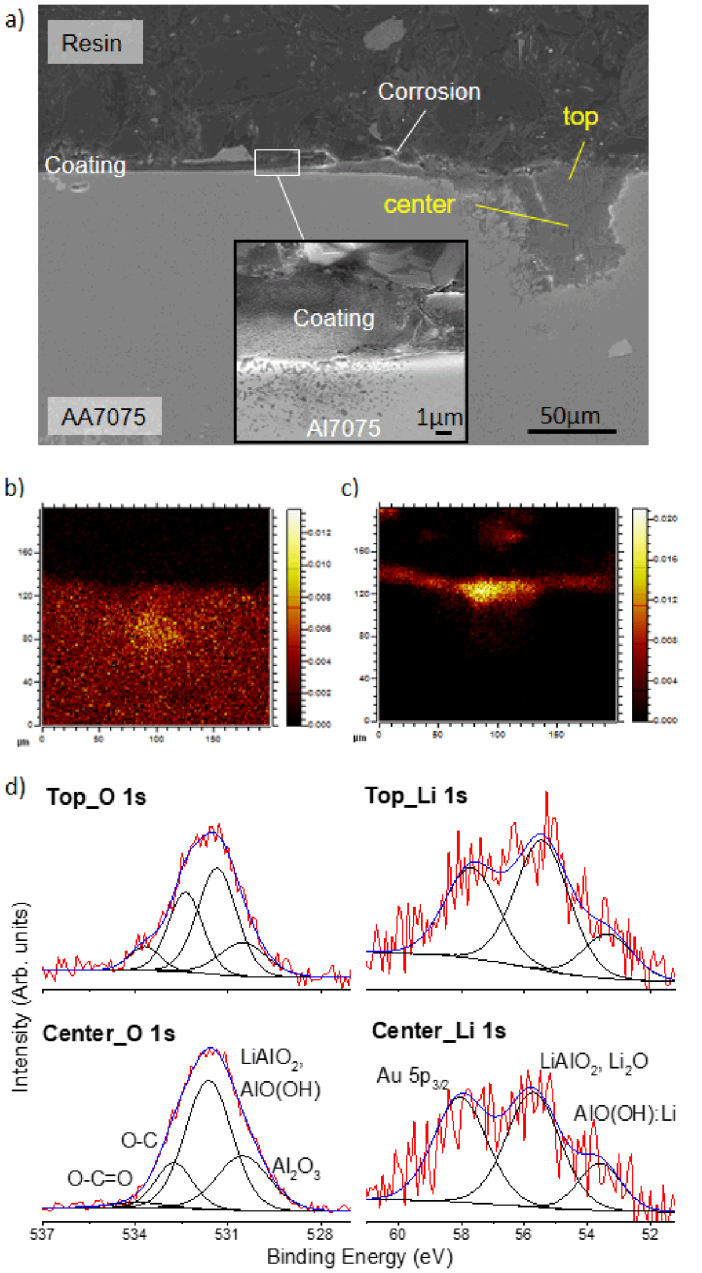

Figure 31. a) Cross-section view of the pit of Li1 coating obtained by SEM after 310 days of immersion in 3.5% NaCl. Normalized cross section ToF-SIMS map of b) $AlOH^+$ (yellow) and c) Li^+ (yellow), recorded in the pit cross-section area (top + center) of Figure 31a. d) Fitted XPS O 1s and Li 1s spectra taken at top and center of the pit. (For SEM analysis sputtered Au was used to improve surface conductivity).

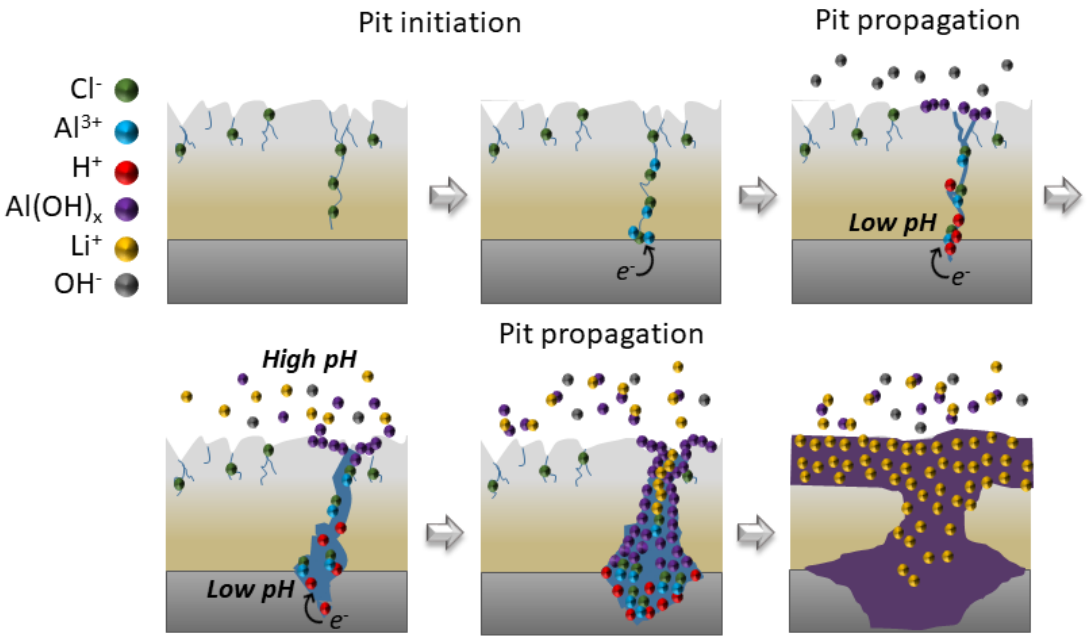

Figure 32. Proposed mechanism for the formation of a lithium induced protective barrier layer (see the description of the steps in the text).

Then the corrosion process of the alloy proceeds horizontally along the metal/coating interface provoking cathodic delamination and/or filiform corrosion (crevice corrosion under a protective film (Figure 31a), the predominant corrosion mechanisms for aluminum alloys [36]. At this stage, the adhesion of the coating to the substrate plays a crucial role in avoiding a fast delamination and consequently alloy dissolution caused by the corrosion process [36]. Simultaneously, aluminum hydroxide precipitates on the top and at the pit walls due to the alkaline conditions created by leached Li^+ ions from the adjacent coating, as evidenced in Figure 30b [12,13,76,78]. The presence of carbonate, a conjugate base, contributes to a further local pH increase by reacting with a proton from water under formation of hydrogen carbonate (HCO_3^-) and hydroxyl ions (OH^-) [78].

$$CO_3^{2-} + H_2O \leftrightarrows HCO_3^- + OH^- \qquad (23)$$

Next, the Al hydroxides formed during the corrosive attack trigger species able to react with Li^+ [78,80]:

$$Al(OH)_4^- = AlO_2^- + 2H_2O \qquad (24)$$

$$Li^+ + AlO_2^- \leftrightarrow LiAlO_2 \qquad (25)$$

Based on XPS (Figure 31d) and SIMS result (Figure 30b and Figure 31c) this process induces the formation of a protective lithium rich barrier layer based on $LiAlO_2$ and/or Li containing AlO(OH) on the top of cathodic corrosion products, mainly composed of Al hydroxides. Subsequently, the barrier properties in the defective zone are restored, leading to a recovery of the corrosion resistance of the coating.

2.3 Active protection of scratched coatings

To evaluate the lithium ions induced corrosion inhibition in PMMA-silica hybrids, the coatings were manually scratched and exposed to accelerated corrosion test. After 1 day and 7 days in salt spray chamber (ASTM-B117), the scratched films were examined by SEM and EIS. Figure 33a and Figure 33b show a notable difference between the lithium free (Li0) and Li2 coating (selected here due to a more pronounced lithium effect). SEM images showed that after 7 days of salt-spray exposure the damaged area of the Li2 sample is almost completely covered by a homogeneous layer, whereas the Li0 sample presents abundant debris of corrosion products. EIS measurements of the scratched samples recorded after 1 and 7 days of salt-spray confirmed the formation of a protective layer for the lithium containing coating (Li2), resulting in an increase of the corrosion resistance of one decade, while for the Li free coating a drop of impedance modulus was observed (Figure 33b and Figure 33a).

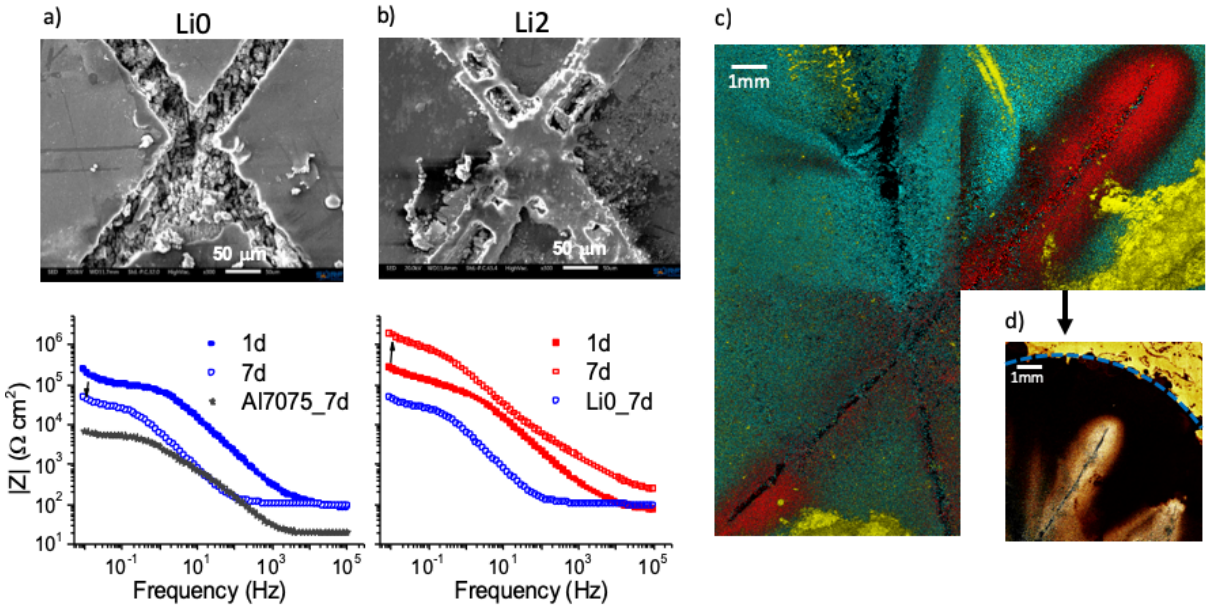

Figure 33. SEM images of the scratched film recorded after 7 days salt spray-test and the corresponding EIS impedance modulus profiles after 1 day and 7 days for a) Li0 and Al7075 substrate and b) Li2 samples. ToF-SIMS maps of the Li2 sample showing c) the overlay map of Li^+ (red), $AlOH^+$ (green) and $C_2H_3O_2^+$ (yellow), d) Li^+ normalized map (yellow).

SIMS maps of the Li2 sample scratched zone were obtained to investigate the nature of the formed layer in the presence of lithium ions. The overlay maps of Li^+ (red), AlH^+ (green) and $C_2H_3O_2^+$ (yellow) show high concentration of lithium within the scratch track, suggesting also in this case that lithium ions were preferentially leached from the coating into the active corrosion zones (Figure 33c). The surface leaching of Li^+ into the scratch was confirmed by the presence of a circle edge from the tape (blue dashed line) used to cover a part of the coating during the salt-spray test (Figure 33d). The covered coating surface (Figure 33d) presented higher lithium concentration (yellow intensity) compared to the area exposed to salt-spray, which was covered by an AlOOH layer (green).

SEM analysis evidenced below this layer the presence of the coating (Figure 34). After 7 days of salt spray, EDS layered map of Li2 shows in Figure 34a that the coating was covered by a thick layer of corrosion products, identified as $AlOH^+$ phases by SIMS (green area in Figure 33c). EDS spectrum evidences the presence of carbon (in green) attenuated by the debris formed by Al and O. In addition, the quantitative analysis show that the 3rd most abundant element is C and that the C to Si ratio is close to that of

PMMA-silica coating (10 : 1.5) with a wt. percentages of 9.1 and 1.7, respectively. Finally, the Si map of the regions adjacent to the scratch shows the presence of Si (Figure 34b), a confirmation that the coating is preserved below the debris.

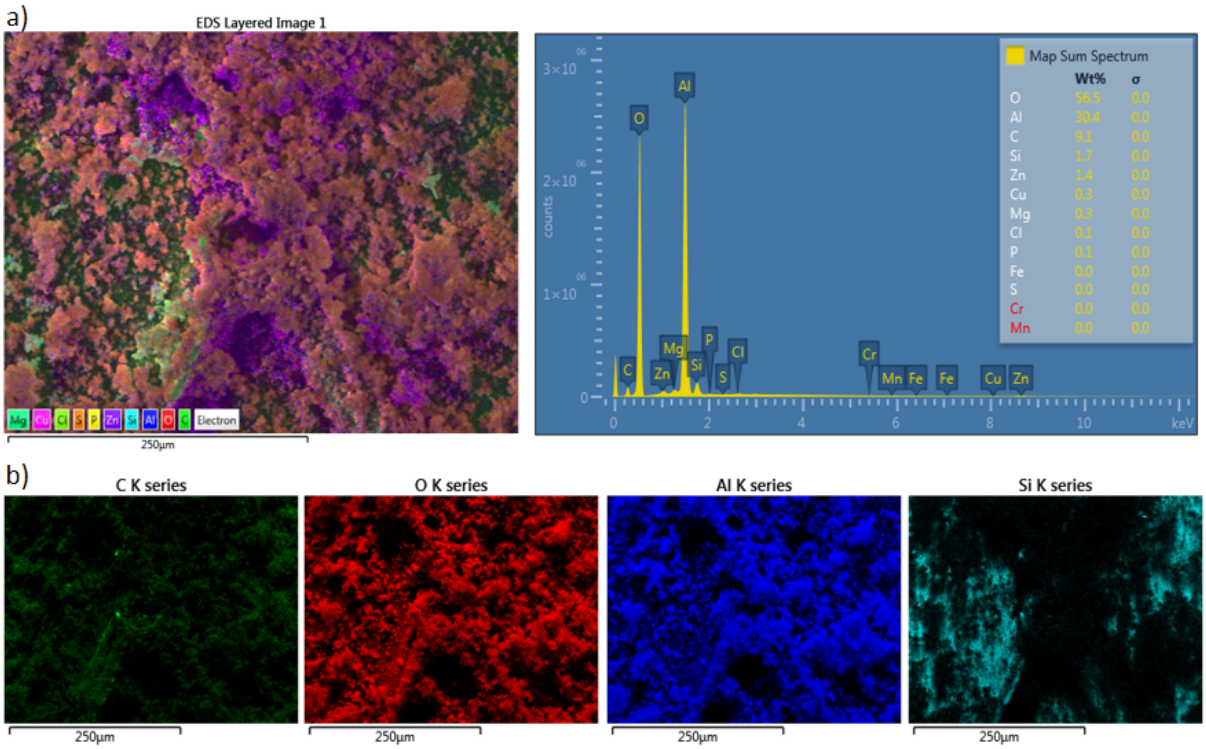

Figure 34. a) SEM overlay map of scratched Li2 and elemental spectrum sum and b) EDS maps of C, O, Al and Si after 168 h NSS exposure.

The protection of scratched PMMA-silica coatings submitted to aggressive environment is driven by the dissolution of lithium ions from the surface and walls of the scratch after contact with the electrolyte, a process that slowly ceases after depleting the adjacent coating [73,119]. The leached lithium ions migrate into the anodic areas of redox reactions driven by the pH gradient and intercalate within aluminum hydroxide species present in the solution forming a pseudoboehmite structure (incompletely dehydrated boehmite [AlO-(OH)]), a process not observed in the absence of lithium as can be seen in the comparison of Li0 and Li2 SIMS mass spectra in the range 0 – 100 m/Z (Figure 35) [12,13,62,118]. Consequently, the relationship between the lithium distribution in the active sites (Figure 33c) and the formation of inhibiting lithium containing pseudoboehmite involves a complex

dependence of variables such as intercalation rate, cathodic area, local pH and concentration of ionic species [12,78,120].

The analysis of the cationic fragments, detected in the SIMS spectra for Li0 and Li2 samples (Figure 33c), indicates that lithium might have driven a precipitation reaction of aluminum oxides in the form of pseudoboehmite, identified as the most abundant specie. One possible cause might be the reversible intercalation of Li ions within the aluminum oxide structure, favored in an environment with leached lithium ions [62,76,118,120]. The obtained results point on lithium containing pseudoboehmite as the phase responsible for the impedance increase observed after 7 days of salt-spray.

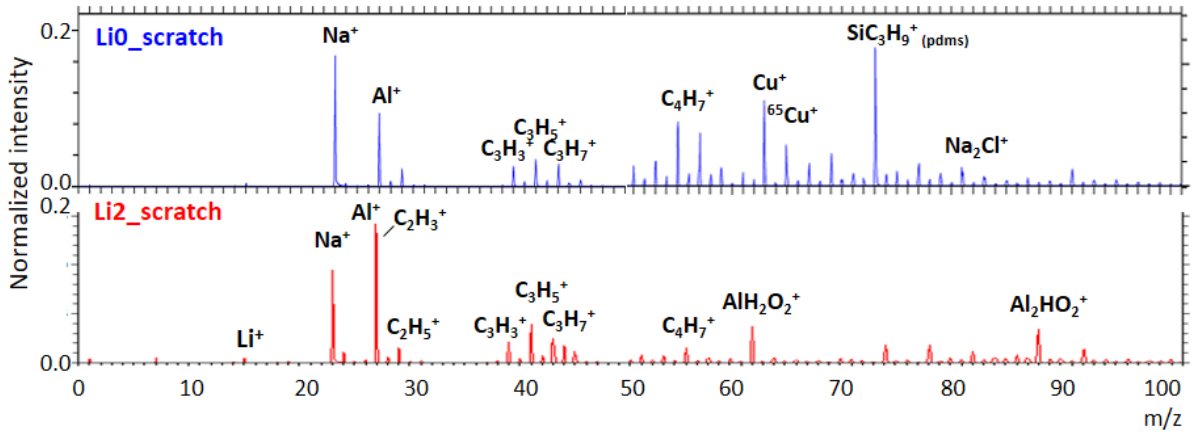

Figure 35. Positive ToF-SIMS mass spectra in the range 0 - 100 m/Z recorded in the scratch track (ToF-SIMS map in the Figure 33c) for Li0 and Li2 samples after 7 days of salt-spray exposure.

We have shown that lithium modified PMMA-silica coatings provide for aluminum alloys not only an active corrosion protection after permeation of electrolytes through the coating (pitting), but also an active protection after artificial damage of the coating, extending significantly the service lifetime of the alloy. Moreover, it was shown that this performance can be achieved with much thinner coatings, resulting in considerable material savings.

2.4 Conclusions

The incorporation of lithium ions into PMMA-silica nanocomposites resulted in significant modification in the hybrid structure. SAXS, NMR, TGA results showed that a concentration of lithium higher than 1000 ppm contributed to the improvement of the hybrid structure in three main aspects: i) formation of a homogeneous monomodal distribution of silica nanoparticles, ii) increase the connectivity of the inorganic network, which contributes to interfacial adhesion, and iii) improvement the polymerization efficiency by strong reduction of stacking defects of the PMMA phase, thus resulting in a dense highly cross-linked hybrid network that acts as an efficient diffusion barrier against corrosive species. This structural optimization was confirmed by EIS results, evidencing an improvement of the already excellent barrier properties of the PMMA-silica coating, thus protecting effectively the aluminum alloy substrate.

Another notable feature of Li containing coatings is their active corrosion inhibition. The self-healing ability, observed by EIS after long-term immersion in saline solution as a restoration of the impedance modulus, was identified as a depletion process of lithium from the adjacent film surface and its migration to localized corrosion spots forming a protective layer of lithium containing aluminum oxide under alkaline conditions, provided by hydroxyls from carbonate oxidation. It was found that higher Li concentrations accelerate this recovery process and delay the formation of pits, thus extending significantly the lifetime of the coating.

In the case of artificially scratched coatings, an analogous self-recovery mechanism was proposed to explain the increase of the impedance modulus of about one order of magnitude after 7 days of salt-spray test. Here the leached Li ions trigger a precipitation reaction of aluminum oxides in the form of pseudoboehmite creating a protective layer within the scratch track that results in a significant reduction of the corrosion rate. From this, it is clear that high mobility and chemical activity of lithium ions are the driving force of the self-healing process. Hence, it can be concluded that PMMA-silica hybrids modified by lithium represent a new class of low-cost functional coatings with the potential to replace the toxic hexavalent chromium-conversion process used to protect aluminum alloys against corrosion.

Chapter 3[c]: Influence of Ce(III) and Ce(IV) ions on the structure and anticorrosive properties of PMMA-silica hybrid coated AA7075 alloy

3.1 Influence of Ce(III) and Ce(IV) ions on the structure of the PMMA-silica coatings

Among inorganic corrosion inhibitors, cerium ions incorporated within reservoirs or added directly into the precursor solutions have proven to be very efficient as cathodic inhibitors through precipitation of insoluble oxides and hydroxides in defective areas of the coating [54,63–66]. Upon immersion in a 3.5% NaCl, the incorporation of Ce(III) into nano/microcontainers or clays provided corrosion inhibition for commercial epoxy [64,121,122] and sol-gel (zirconium (IV) propoxide – 3-glycidoxypropyltrimethoxysilane) coatings [123]. Moreover, CeO_2 nanoparticles have demonstrated active protection for hybrid sol-gel coatings on aluminum 2024, magnesium AZ31 and galvanized steel alloys [63,71,124]. An analogue cathodic protection was observed for Ce(IV) in sol-gel coatings [40,125]. When incorporated into the PMMA-silica system the activity of Ce(IV) as oxidation agent lead to an enhancement in the degree of silica/siloxane polycondensation and polymerization of the organic moieties [39,41,60]. Hence, in order to understand the role of cerium on the structure and corrosion inhibition of PMMA-silica coatings, this work reports a detailed comparison between Ce(III) and Ce(IV) ions on their structural and anticorrosive properties.

The results obtained by SAXS (Figure 36a and Figure 36b) evidence that the addition of increasing amounts of both salts changes significantly the hybrid nanostructure, in particular for samples with highest cerium content (≥ 3000 ppm). The profiles obtained for highest cerium concentrations were fitted using Beaucage function to extract the Guinier radius of gyration (R_g) [82,83]. For samples with the highest Ce content (3000 and 5000 ppm), a second structural level in low q-range

[c] This chapter will be submitted for publication as a scientific paper.

indicates the formation of large agglomerates as illustrated in Figure 36c. In the high q-range, a radius of gyration R_{g1} of about 0.7 nm was obtained for both Ce(III) and Ce(IV) containing samples, indicating that the silica clusters are formed by sub-nanometric particles [40]. The radius of gyration, R_{g2}, extracted in low q-range indicates that larger silica aggregates were formed, in the range of several nanometers: 2.9 and 2.7 nm for the Ce(III)_3 and Ce(III)_5 samples, and 3.8 and 3.9 nm for Ce(IV)_3 and Ce(IV)_5 samples, respectively. However the possible contribution of remaining cerium nitrates particles cannot be exclude in this concentration range [126,127]. Concerning the samples with lower cerium content, the presence of a correlation peak in the mid q-range prevented to obtain reliable results from Beaucage fitting, however allowed to determine for the peak position ($d = 2\pi/q$) the average correlation distance indicating a homogeneous distribution of a concentrated set of scattered silica nanoparticles separated by 3 – 4 nm. In the case of Ce(IV) samples there is a slight increase of the spacing with increasing Ce content, while the opposite is observed for Ce(III) samples (Table 12).

The coatings are homogeneous, present a thickness close to 3 µm, they are colorless at low concentrations and become yellowish for higher Ce(IV) content (Table 12). The presence of aggregates observed by SAXS for Ce(III) and Ce(IV) concentration ≥ 3000 ppm of was also inferred from the increase of the RMS roughness (R_{RMS}), obtained by AFM analysis. The roughness values increased from 0.8 nm to 6.7 nm for Ce(IV) and from 0.6 nm to 2.2 nm for Ce(III) (Table 12). Cerium addition affected also the adhesion strength to the aluminum surface, showing an increase of adherence for samples with lower cerium content of up to 22.1 MPa (Ce(IV)_1) compared to the cerium free reference (17.9 MPa). However for higher cerium loading, the formation of larger aggregates and possibly cerium salt particles, as suggested by SAXS results, decreased the adhesion to the substrate. Nevertheless, it is important to note that all values are superior to those of conventional coating system based on paints, with values below 10 MPa.

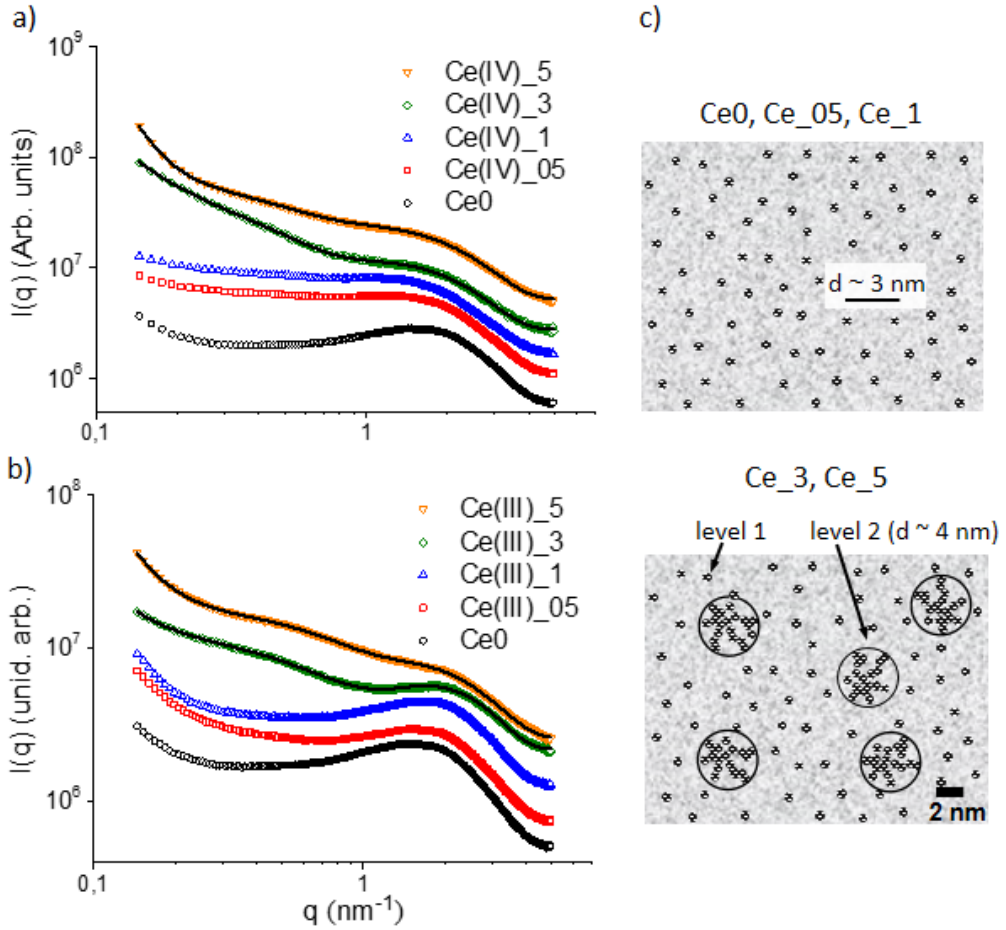

Figure 36. a) SAXS profiles of PMMA-silica hybrids prepared with different concentrations of a) Ce(IV) and b) Ce(III). Black lines are fits using the Beaucage model for ≥ 3000 ppm of cerium; c) Structural representation of the silica phase embedded in PMMA matrix for low (including cerium free) and high Ce concentrations (≥ 3000 ppm).

Information on the thermal stability and decomposition events of the polymeric structure were accessed by thermogravimetry (Figure 37). The DTG curves (derivative of TG) of the hybrids prepared at different Ce amounts show three main degradation events: breaking of head-head segments (T_1 at 240 °C), scission of unsaturated vinylidene chain-ends (T_2 at 310 °C) and random depolymerization at 400 ºC (T_3) [92]. The small tail at about 480 ºC is attributed to the dehydration of residual silanol groups after hydrolysis and condensation [40].

The thermal stability (T_S), determined for 5% weight loss, was for all hybrid samples in the range 237 °C to 247 °C, showing no correlation with the cerium content. This indicates that the overall connectivity of the hybrid network was not negatively

affected by cerium inclusion. In contrary, the observed suppression T_2 event (unsaturated PMMA chain endings) for cerium loaded samples (Ce(III) and Ce(IV)) indicates an improvement of the polymerization efficiency. This finding confirms the active role of cerium in the polymerization process. As suggested by some authors, the cerium redox system acts as additional polymerization agent by opening the vinyl double bond of the acrylate terminations, thus improving the polymerization degree of the organic phase (Reaction 17) [40,60,127–130]. Polymer chain growth stems principally from the activity of Ce(IV) free radicals able of initiating vinyl polymerization, also present in Ce(III) containing PMMA-silica hybrids [127,128,130]. Finally, the increase of the inorganic residue at 800 °C, ranging from 19% - 27%, scales with the additional contribution of cerium to the inorganic phase (Table 12).

Structural and thermal analysis of PMMA-silica hybrids proved similar impact of both precursors on the final structure, possibly induced by Ce(III) ↔ Ce(IV) transitions of the instable cerium redox system during the thermal treatment.

Table 12. Properties of Ce containing PMMA-silica hybrids: film thickness obtained by optical interferometry; RMS surface roughness (R_{RMS}) extracted by AFM; adhesion strength measured by pull-off test; decomposition on-set temperature (T_s) and residue by TGA; and correlation distance (d) determined by SAXS.

Sample	Thickness (µm)	R_{RMS} (nm)	Adhesion (MPa)	T_s (°C)	Residue (%)	d (nm)
Ce0	3.7	0.8	17.9	237	19	3.6
Ce(IV)_05	3.4	0.9	21.4	241	22	3.7
Ce(IV)_1	3.4	0.3	22.1	247	23	4.0
Ce(IV)_3	2.8	3.9	14.4	240	24	-
Ce(IV)_5	3.6	6.7	9.5	244	26	-
Ce(III)_05	2.5	0.6	19.5	238	24	3.4
Ce(III)_1	2.5	0.7	13.8	237	23	3.3
Ce(III)_3	2.7	1.7	11.3	238	26	-
Ce(III)_5	2.8	2.2	12.9	242	27	-

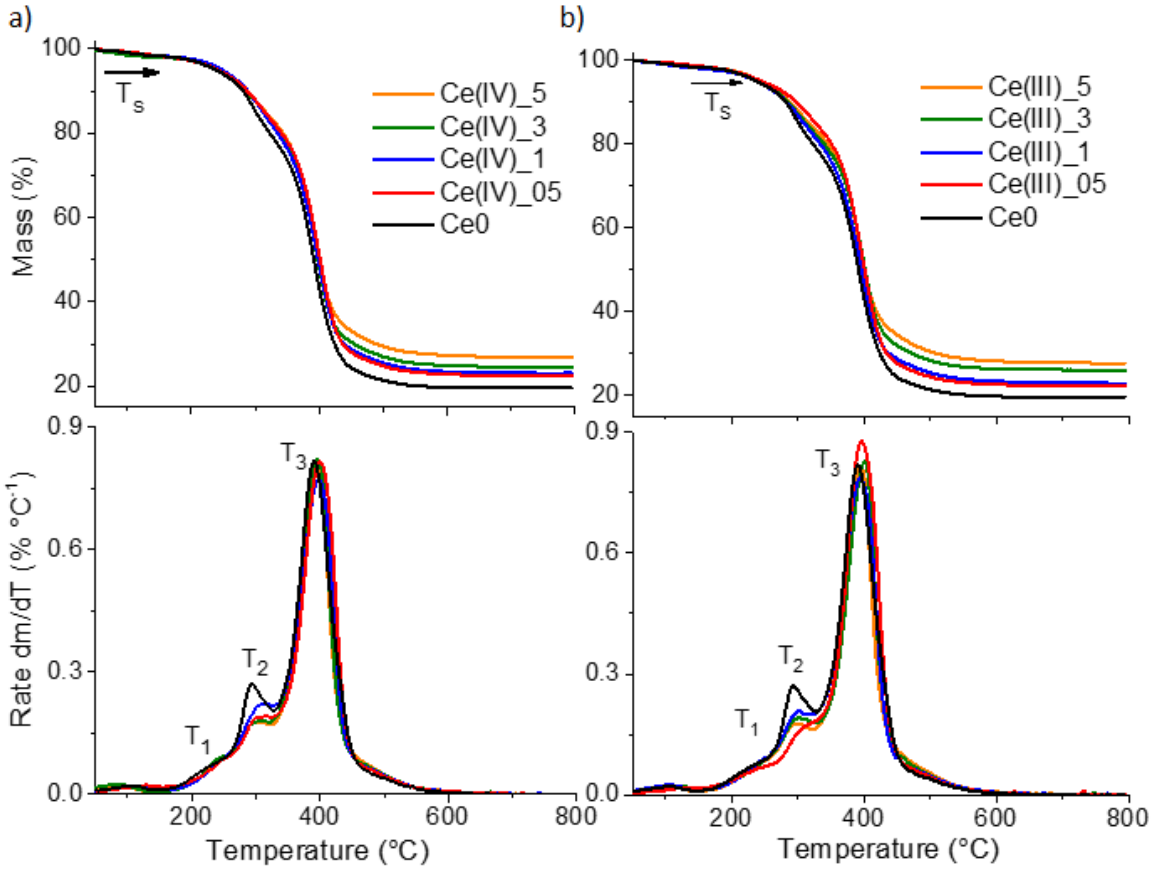

Figure 37. TG and DTG curves of modified PMMA-silica hybrids with concentrations of a) Ce(IV) and b) Ce(III).

3.2 Active corrosion inhibition

A major challenge in designing active hybrid coatings is to provide a balance between additive loads in the structure without affecting it. For PMMA-silica-Ce coatings, the homogeneous dispersion of silica and cerium in the hybrid structure and absence of large aggregates leads to adherent, crosslinked and dense barrier coatings, as evidenced by EIS measurements. The corrosion resistance of the hybrid coatings deposited on AA7075 was accessed by EIS measurements in 3.5% NaCl solution (Figure 38). Regardless the type of cerium salt added, after 3 h immersion the coatings presented a high low-frequency impedance modulus ($|Z_{lf}|$) of more than 10 GΩ cm^2, up to six orders of magnitude higher than bare aluminum, and showed a quasi-ideal capacitive phase angle behavior close to -90° over almost the entire frequency range (Table 13).

In terms of durability in saline solution, the incorporation of Ce(IV) leads to significant improvements especially in the low an medium concentration range, maintaining the low-frequency above 1 GΩ cm^2 for up to 529 days (Table 13). For higher cerium concentrations a reduction of the coating live span can be observed. This might be related to the presence of larger agglomerates due to excess of nitrates anions [127] affecting the hybrid structure, as also suggested by SAXS results. A decrease of the life span for high cerium loading was not observed for Ce(III) modified coatings, showing for all concentrations a long-term stability of up to 519 days (Table 13).

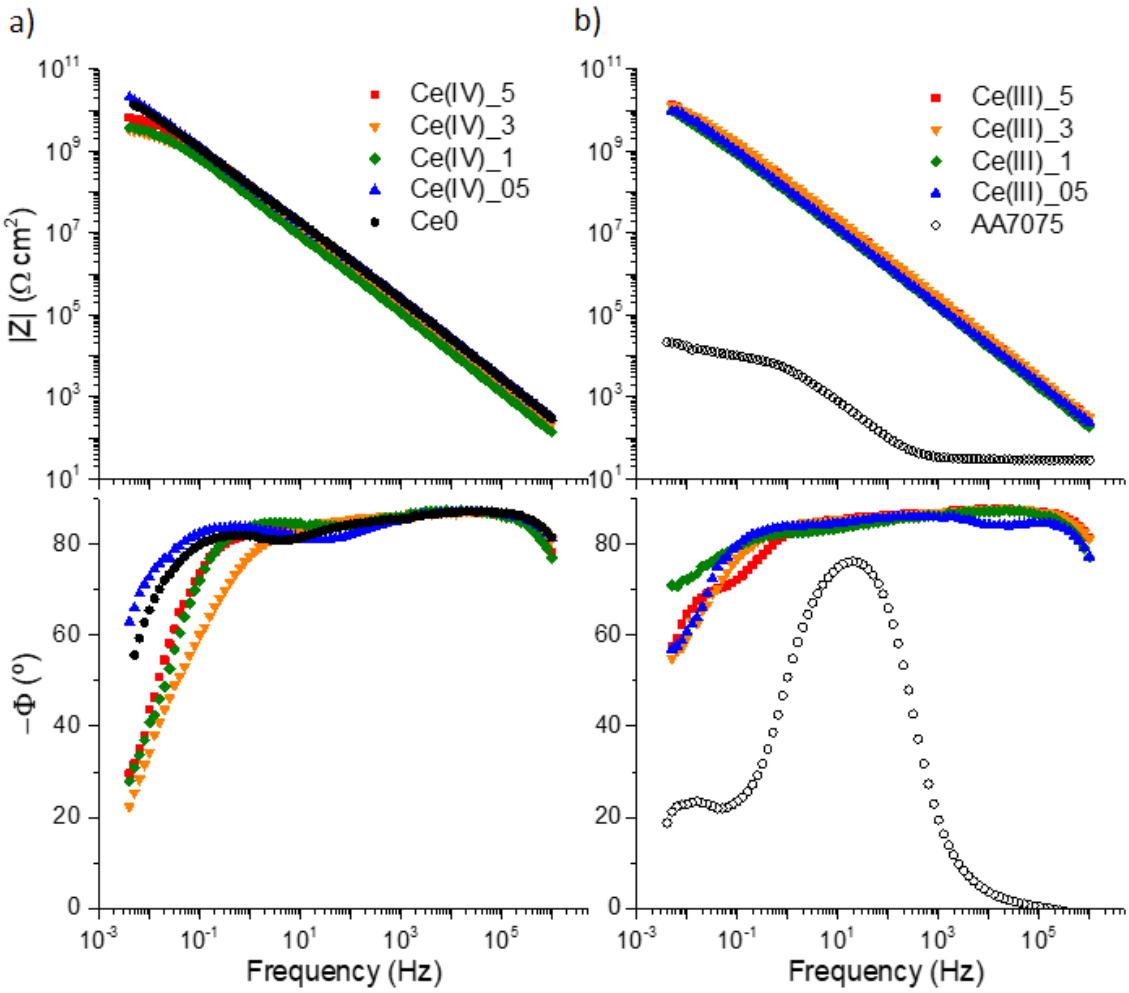

Figure 38. a) Impedance modulus and phase angle vs. frequency plots for a) Ce(IV) and b) Ce(III) PMMA-silica hybrid films on AA7075, recorded after 3 h in 3.5% NaCl solution at 25 °C.

Table 13. Impedance modulus at low frequency ($|Z|_{lf}$) after 3 h and 30 days of immersion in 3.5% NaCl normalized by the thickness; ($|Z|_{3h}/|Z|_{30d}$), E_{OC} after 3 h and time until the first failure event, of PMMA-silica coatings on AA7075, obtained in duplicate for Ce(IV).

Sample	$\|Z_{lf}\|$ thickness^{-1} (GΩ cm^2 μm^{-1})		$\|Z\|_{3h}/\|Z\|_{30d}$	-(E_{OC})	1st failure event (days)
	3 h	30 d		(mV/Ag/AgCl)	
Ce0	5.8 / 3.2	3.7 / 0.7	1.5 / 4.5	722 / 475	72 / 80*
Ce(IV)_05	6.0 / 1.8	4.2 / 0.1	1.4 / 6.0	979 / 701	529 / 21 (116)**
Ce(IV)_1	7.1 / 1.1	3.5 / 1.0	2.0 / 1.3	1030 / 831	271* / 310
Ce(IV)_3	0.4 / 0.1	0.2 / 0.02	2.0 / 1.8	787 / 1037	169 / 120
Ce(IV)_5	2.0 / 0.5	1.2 / 0.01	1.6 / 10.0	868 / 761	157 (183)** / 61
Ce(III)_05	5.6	3.9	1.5	663	455
Ce(III)_1	1.6	1.5	1.1	739	198*
Ce(III)_3	2.7	2.3	1.1	667	243
Ce(III)_5	4.1	3.4	1.2	796	519

*Ongoing measurement, **current immersion time

Figure 39 shows the time dependence of $|Z|_{lf}$ for coatings modified with different concentrations of Ce(IV) (Figure 39a) and Ce(III) (Figure 39b) during 30 days of immersion. The comparison of Ce(IV) coatings prepared in duplicate (Figure 39a) shows a certain variability of $|Z|_{lf}$, especially for samples with higher cerium content. Despite these variations, all coatings present very good corrosion resistance with impedance modulus in the GΩ cm^2 range. Nonetheless, more experiments are needed to improve the reproducibility affected by the variations of the substrate morphology, such as presence of pores and roughness, and also by the coating deposition conditions (temperature, humidity, viscosity, etc.)

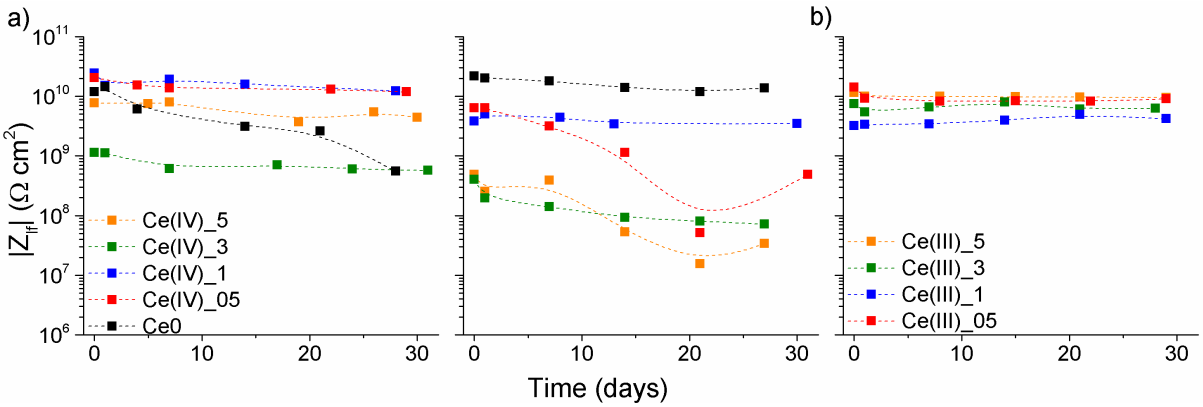

Figure 39. a) Time evolution of $|Z|_{lf}$ for coatings modified with different amounts of a) Ce(IV) in duplicate and b) Ce(III) during 30 days of immersion in 3.5% NaCl.

Active corrosion inhibition was evidenced only for Ce(IV) containing coatings, as can be observed in the Bode plots of Figure 40, Ce(IV)_05 and Ce(IV)_5 coatings show a partial restoring of the impedance modulus after 42 and 173 days of immersion, respectively, clearly visible by the increase of the phase angle at low and intermediate frequencies. The expected effect of cerium addition is the passivation of corrosion-induced defects by the formation of insoluble cerium oxide phases, thus increasing coatings lifetime. The faster regeneration observed for Ce(IV)_5 can be related to the greater availability of Ce^+ ions. A self-healing effect after local pitting was reported in a recent study after monitoring the long-term behavior of the impedance modulus of PMMA-silica-Ce(IV) coatings on carbon steel immersed in 3.5% NaCl solution [127]. A possible explanation for the finding that only Ce(IV) coatings provide active corrosion inhibition after pitting [15,63] is that under a pH gradient, Ce(IV) forms insoluble hydroxides at a pH of about 3 in comparison to those from Ce(III) formed at a pH of about 9 [15].

Three main regions are clearly present in the phase angle plot during electrolyte uptake: (i) at high frequencies a time constant is attributed to the external part of the coating, more specifically at coating/electrolyte interface, (ii) the medium range is usually related to the coating bulk and passive layer of aluminum as Al-O-Al and Al-O-Si bonds [37] and (iii) at low frequencies <10 Hz the time constant is associated to corrosive phenomena related to the charge transfer process at the metal/coating interface. Therefore, the electrochemical reactions occurring at the inner part of the coating can be accessed by changes in phase angle plots at low/medium frequencies.

Interesting features can be seen in the time dependence of the phase angle plots for Ce(IV)_05 and Ce(IV)_5 coatings (Figure 40). The sample Ce(IV)_05 showed an impedance recovery after pitting more pronounced at about 0.1 Hz by the suppression of charge transfer process at the interface whereas Ce(IV)_5 partially restored the impedance at medium and low frequency. These behavior in the low/medium frequency range indicate the formation of insoluble $Ce(OH)_4/CeO_2$ induced by cerium IV ions within the pits and consequently a reduction of charge transfer process at metal/coating interface.

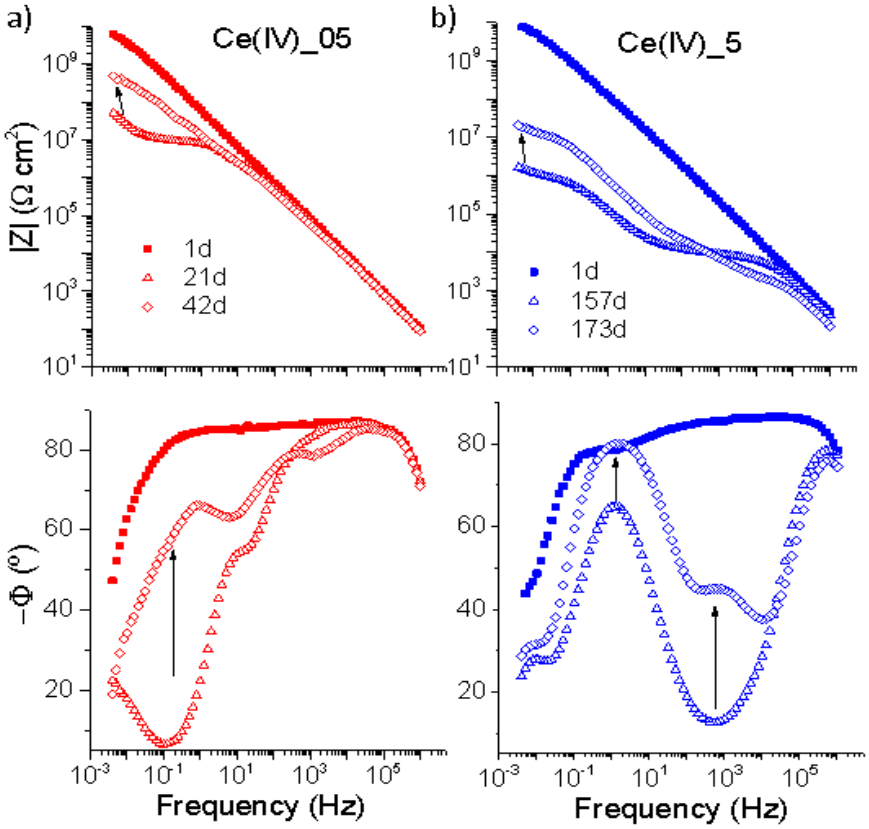

Figure 40. a) Time evolution of Bode plots for Ce(IV)_05 and b) Ce(IV)_5 samples showing partial regeneration of the impedance in the pit affected region.

Figure 41 displays SEM image and SIMS maps of the pitted zone on Ce(IV)_5 coating. The overlay SIMS maps of Al^+, Ce^+, CeO^+, Cu^+ and Zn^+ ionic species (~5 nm sampling depth) show that, although the surface is not covered by cerium phases (Ce^+ or CeO^+ signal) there is a spatial correlation between Cu^+ and Zn^+ (intermetallic constituents of AA7075) and CeO^+ and Ce^+ species, indicating that the formation of

cerium oxides on Zn and Cu intermetallic phases may account for cathodic protection in the defective zone.

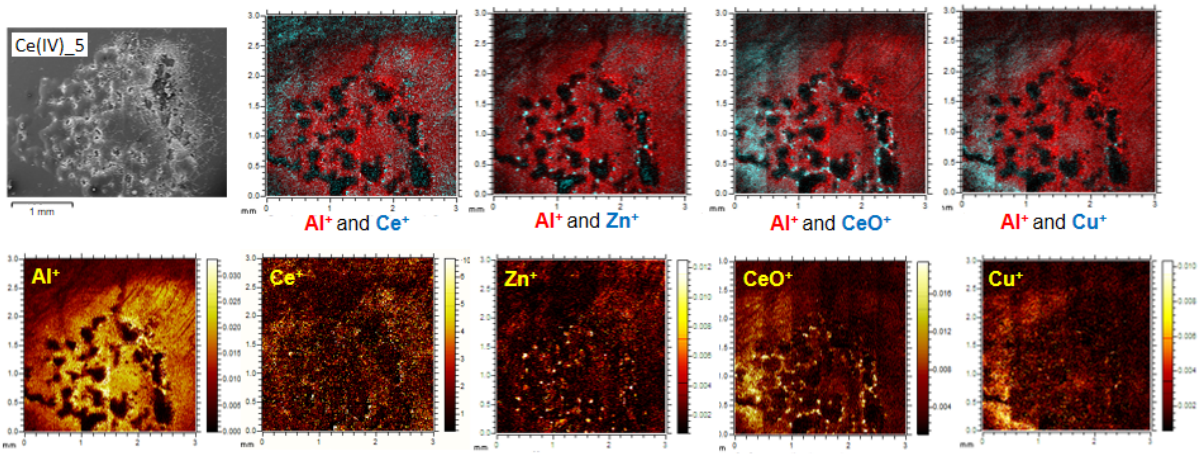

Figure 41. SEM image and SIMS maps of the pit of sample Ce(IV)_5 after 173 days of immersion in 3.5% NaCl solution.

More rigorous tests on the regeneration ability of Ce(IV) containing coatings were conducted by accelerated corrosion test. In Figure 42, SEM images of scratched coatings after 7 days of salt spray test are shown. The spatial correlation between Ce, Zn and Cu rich areas at the edges of the scratch track suggests that the small increase of impedance after 7 days exposure, observed for Ce(IV)_05 and Ce(IV)_3 samples in the corresponding Bode plots (Figure 43), can be related to the inhibitive effect induced by the formation of insoluble cerium species in segregation zones of Zn and Cu corrosion products. In the center of the scratch the corrosion products are mainly composed of Al species.

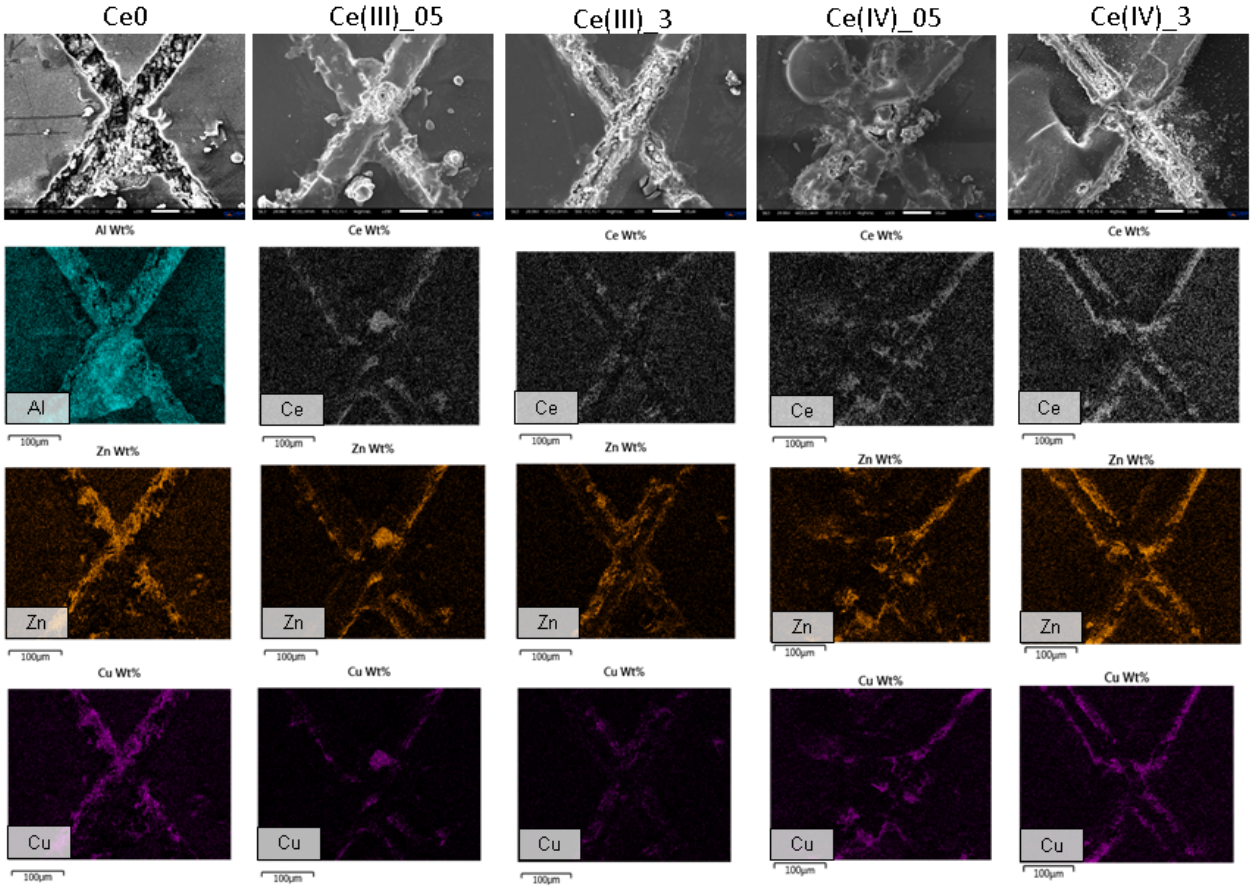

Figure 42. SEM top view of the scratch with EDS maps of Al, Ce and Zn after 7 days of salt spray.

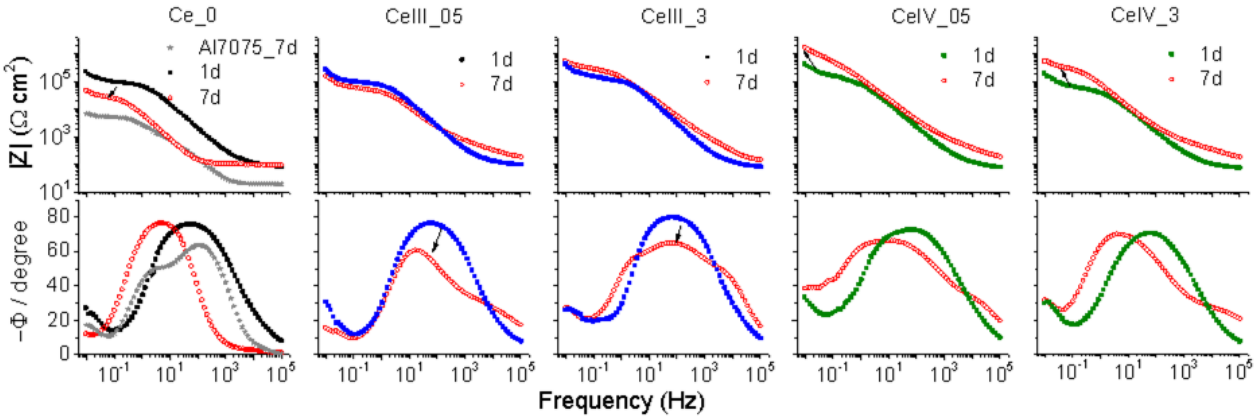

Figure 43. Bode plots recorded after 1 and 7 days (red) of salt spray, for Ce0, Ce(III)_05, Ce(III)_3, Ce(IV)_05 and Ce(IV)_3 coatings.

Although PMMA-silica-Ce(III) coatings also exhibited the presence of Ce at the scratch edges, no impedance modulus increase was observed, rather a tendency for an impedance drop as suggested by the phase angle plots was observed, a behavior

comparable to the cerium free coating. This is most likely related to the higher solubility of the Ce products formed in the corrosion pH range of AA7075.

A detailed study was carried out by SIMS to elucidate the mechanism of regeneration observed for Ce(IV) coatings, choosing the Ce(IV)_5 sample to achieve best cerium detection. Figure 44 shows the optical images and corresponding SIMS maps of Ce(IV)_5 after 7 days of exposure to salt-spray. The images evidence a depletion of cerium in the exposed area due to leaching by the electrolyte and an accumulation of Ce and Cu species in the scratch track. Similar to the process observed for Li, the explanation for the increase of the impedance modulus of pitted and artificially scratched coatings can be attributed to the redox activity of Ce(IV) ions (Reactions 11 - 13) leached from adjacent coating wall into the damaged zone. Furthermore, Figure 44d shows that during the spray test, corrosion products ($AlOH^+$) were spread over the coating ($C_4H_5O^+$, PMMA fragment).

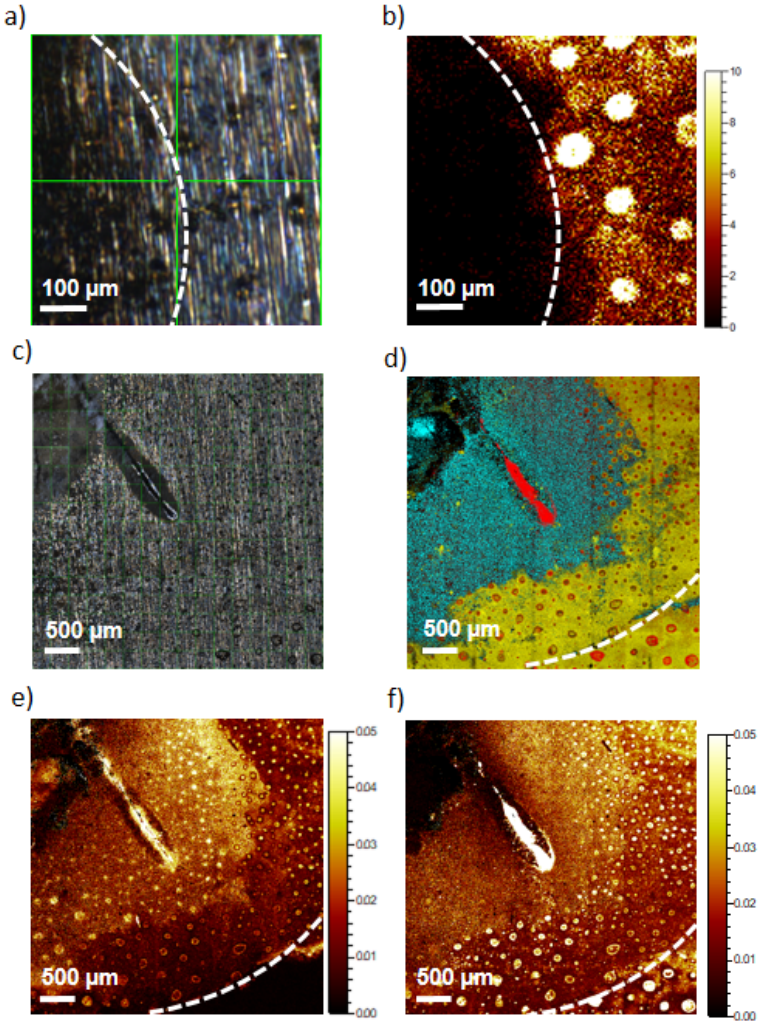

Figure 44. a) Optical micrograph at the edge of the exposed area of Ce(IV)_5 after 7 days of salt-spray and corresponding SIMS map of b) Ce^+ (yellow); c) optical image of the scratched region of Ce(IV)_5 and corresponding SIMS maps of d) overlay of CeO^+ (red), $AlOH^+$ (green) and $C_4H_5O^+$ (yellow), e) Cu^+ (yellow) and e) CeO^+ (yellow). The Ce^+ spheres present on the unexposed coating surface may result from selective salt precipitation from the electrolyte.

Recent studies show that a wide range of synthesis parameters, such as the ratio between the organic and inorganic precursors, type of coupling agent, polymerization initiator and corrosion inhibitors can be used to optimize the structure of coatings, enhancing their corrosion resistance [27,31,38]. Here it was shown that the balance of cerium loadings promotes an optimal hybrid structure in addition to provide active protection to AA7075. A comparison between Ce(III) and Ce(IV) showed that only Ce(IV) addition provides active corrosion protection, reacting with cathodic intermetallics and passivating them by formation of insoluble oxides and hydroxides.

3.3 Conclusions

The addition of Ce(III) and Ce(IV) into PMMA-silica hybrids increased the thermal stability up to 247 °C along with a gradual reduction of unsaturated PMMA terminations by enhancing the PMMA chain growth, as found by TGA. SAXS results showed more significant changes in the hybrid structure for higher cerium content (≥3000 ppm), explained by an excess of cerium salts which aggregate in the hybrid network, leading to a decrease of adhesion to the substrate and coating durability. Hence, intermediate cerium loading (500 – 1000 ppm) provides an optimized structure resulting in an excellent passive protection of the aluminum surface.

All hybrid coatings presented high anticorrosive performance, with impedance modulus up to 7.1 GΩ cm^2 μm^{-1}, nonetheless only the addition of Ce(IV) provided active protection for AA7075. This partial regeneration effect of the PMMA-silica-Ce(IV) coating was is explained by the redox activity of Ce(IV) ions leached from adjacent coating walls into the damaged zone and the subsequent formation of insoluble oxide and hydroxide phases that block corrosive process. The beneficial effect provided by intermediate Ce(IV) loadings on the structure and active corrosion inhibition properties of PMMA-silica coatings makes this material a potential candidate for the development of low-cost, high-performance and active chromium-free coatings.

Part III

Conclusions and outlook

The investigation of organic-inorganic hybrid coatings for the protection of metallic surfaces has been boosted in the last years. This interest is based on the wide range of polymer options available combined with a large quantity of nanofillers and inhibitors that can be incorporated into organic matrices, resulting in new material that profit from the synergy between the constituent phases. This integration, when properly conducted, enhances essential properties for anticorrosive application, including adhesion to metallic substrates, crosslinking of the hybrid network able to block the entrance of corrosive species, as well as increases mechanical strength and thermal stability to withstand aggressive environments and high temperatures. However, the right choice of a large number of variables of the synthesis parameters, deposition and thermal curing and the choice of inhibitor to obtain coatings which act as an efficient passive as well as active corrosion barrier is quit challenging.

In this work the structural and electrochemical characterization showed that the PMMA-silica coating system is a potential alternative to develop safe and cost-effective chromium-free coatings. The addition of inorganic corrosions inhibitors such as cerium and mainly lithium, which was for the first time incorporated into this phase, proved to be effective in the active corrosion protection of aluminum, resulting in a significant extension of coatings' service life. Moreover, considering that high-performance PMMA-silica coatings can be achieved without specific surface treatment with much thinner coatings than those of conventional paint systems, this implies significantly lower costs and resource savings.

The two-layers permeation model presented in Chapter I, represents a step forward to accomplish a lifetime prediction for coatings exposed to corrosive environments using a theoretical simulation that allows tracking the evolution of physical quantities during electrolyte permeation. However, considering the slight deviation of fitting to the experimental data at high frequencies, future studies could consider to include an additional corrective term to the model accounting for the pore resistance or by adding a third component considering a permeated outer layer of constant conductivity to provide a more reliable uptake estimative.

Based on the findings obtained in this work concerning the structural properties and mechanism of active corrosion inhibitor by lithium and cerium ions, complementary research should be considered for the implementation of PMMA-silica hybrids in the primer and coatings' market, such as:

(i) Explore the compatibility of green solvents in the synthesis of PMMA-silica coatings (e.g. 2-propanol, ethanol) in order to advance the production and application on an industrial scale;

(ii) To investigate the addition of both lithium and cerium ions, combining their inhibitive properties, as they proved to be sustainable inhibitors for the next generation of primers for the coatings industry;

(iii) To evaluate the feasibility of lower cure temperatures (< 100 ºC) considering practical issues in the painting process of large metallic components;

(iv) Evaluate the UV stability and weathering effects of coatings on different metallic substrates in climate chamber tests.

References

[1] W.D. Callister, Jr., D.G. Rethwisch, Materials science and Engineering: And Introduction, 9th ed., Wiley, Hoboken, 2014.

[2] K. Gerhardus, V. Jeff, N. Thopson, O. Moghissi, M. Gould, J. Payer, International Measures of Prevention, Application, and Economics of Corrosion Technologies Study, NACE Impact Rep. (2006) 1–216.

[3] R.N. Lumley, Introduction: Aluminium, the strategic material, in: R.N. Lumley (Ed.), Fundam. Alum. Metall. Recent Adv., Woodhead Publishing, Duxford, 2018: pp. 17–30.

[4] K.U. Kainer, Basics of Metal Matrix Composites Basics of Metal Matrix Composites. Custom-made Materials for Automotive and Aerospace Engineering, Wiley VCH, Weinheim, 2017.

[5] D.S. Lee, D.W. Fahey, P.M. Forster, P.J. Newton, R.C.N. Wit, L.L. Lim, B. Owen, R. Sausen, Aviation and global climate change in the 21st century, Atmos. Environ. 43 (2009) 3520–3537.

[6] J.R. Davis, Light Metals and Alloys, in: Hugh Baker (Ed.), Alloy. Underst. Basics, ASM International, Ohio, 2001: pp. 351–416.

[7] Y. Wan, J. Tan, S. Zhu, J. Cui, K. Zhang, X. Wang, X. Shen, Y. Li, X. Zhu, Insight into atmospheric pitting corrosion of carbon steel via a dual-beam FIB/SEM system associated with high-resolution TEM, Corros. Sci. 152 (2019) 226–233.

[8] J. Alcántara, D. de la Fuente, B. Chico, J. Simancas, I. Díaz, M. Morcillo, Marine atmospheric corrosion of carbon steel: A review, Materials (Basel). 10 (2017) 1–65.

[9] E.D. Verink Jr, Simplified Procedure for Constructing Pourbaix Diagrams, in: R.W. Revie (Ed.), Uhlig's Corros. Handb., 2nd ed., John Wiley & Sons, 1979: pp. 111–124.

[10] F.-Y. Ma, Corrosive Effects of Chlorides on Metals, in: N. Bensalah (Ed.), Pitting Corros., InTech Published, Rijeka, 2012: pp. 139–178.

[11] G.S. Frankel, Pitting Corrosion of Metals A Review of the Critical Factors, J. Electrochem. Soc. 145 (1988) 2186–2198.

[12] M.C. Reboul, T. Warner, H. Mayet, B. Baroux, A Ten-Step Mechanism for the Pitting Corrosion of Aluminium, Mater. Sci. Forum. 217–222 (1996) 1553–1558.

[13] R.T. Foley, Localized Corrosion of Aluminum Alloys—A Review, Corrosion. 42 (1986) 277–288.

[14] S. Gheytani, Y. Liang, Y. Jing, J.Q. Xu, Y. Yao, Chromate conversion coated aluminium as a light-weight and corrosion-resistant current collector for aqueous lithium-ion batteries, J. Mater. Chem. A. 4 (2015) 395–399.

[15] K.A. Yasakau, M.L. Zheludkevich, S. V. Lamaka, M.G.S. Ferreira, Mechanism of corrosion inhibition of AA2024 by rare-earth compounds, J. Phys. Chem. B. 110 (2006) 5515–5528.

[16] P. Rodič, I. Milošev, Corrosion Inhibition of Pure Aluminium and Alloys AA2024-T3 and AA7075-T6 by Cerium(III) and Cerium(IV) Salts, J. Electrochem. Soc. 163 (2016) C85–C93.

[17] E. Deltombe, M. Pourbaix, The Electrochemical Behavior of Aluminum, Corros. 14 (1958) 496t-500t.

[18] J. Ning, Y. Zheng, B. Brown, D. Young, S. Nešić, A thermodynamic model for

the prediction of mild steel corrosion products in an aqueous hydrogen sulfide environment, Corrosion. 71 (2015) 945–960.
[19] K.K. Sagoe-Crentsil, F.P. Glasser, “Green rust”, iron solubility and the role of chloride in the corrosion of steel at high pH, Cem. Concr. Res. 23 (1993) 785–791.
[20] B.N. Stirrup, N.A. Hampson, I.S. Midgley, Pit formation in relation to the etching of aluminium in chloride solutions, J. Appl. Electrochem. 5 (1975) 229–235.
[21] J.A. Moreto, C.E.B. Marino, W.W. Bose Filho, L.A. Rocha, J.C.S. Fernandes, SVET, SKP and EIS study of the corrosion behaviour of high strength Al and Al-Li alloys used in aircraft fabrication, Corros. Sci. 84 (2014) 30–41.
[22] H.R. Fischer, S.J. García, Active Protective Coatings: Sense and Heal Concepts for Organic Coatings, in: M.L. Zheludkevich, R.G. Buchheit, A.E. Hughes, J.M.C. Mol (Eds.), Act. Prot. Coatings New-Generation Coatings Met., Springer Science+Business Media B.V, Dordrecht, 2016: pp. 139–156.
[23] P. Visser, H. Terryn, J.M.C. Mol, Aerospace Coatings, in: A.E. Hughes, J.M.C. Mol, M.L. Zheludkevich, R.G. Buchheit (Eds.), Act. Prot. Coatings New-Generation Coatings Met., Springer Science+Business Media B.V, Dordrecht, 2016: pp. 315–372.
[24] IARC Working Group, Chromium (VI) Compounds, in: L. Galichet (Ed.), Arsenic, Met. Fibres Dusts. A Rev. Hum. Carcinog., International Agency for Research on Cancer, 2012: pp. 147–164.
[25] ECHA - European Chemicals Agency, Appl. Auth. - Curr. Consult. (2019). https://echa.europa.eu/applications-for-authorisation-consultation (accessed July 2, 2019).
[26] Z. Szklarska-Smialowska, Pitting corrosion of aluminum, Corros. Sci. 41 (1999) 1743–1767.
[27] S. V. Harb, A. Trentin, R.F.O. Torrico, S.H. Pulcinelli, C. V. Santilli, P. Hammer, Organic-Inorganic Hybrid Coatings for Corrosion Protection of Metallic Surfaces, in: C. Giudice, G. Canosa (Eds.), New Technol. Prot. Coatings, Intech, Rijeka, 2017: pp. 19–51.
[28] D. Del Angel-López, M.A. Domínguez-Crespo, A.M. Torres-Huerta, A. Flores-Vela, J. Andraca-Adame, H. Dorantes-Rosales, Analysis of degradation process during the incorporation of ZrO2:SiO2 ceramic nanostructures into polyurethane coatings for the corrosion protection of carbon steel, J. Mater. Sci. 48 (2013) 1067–1084.
[29] C. Sanchez, P. Belleville, M. Popall, L. Nicole, Applications of advanced hybrid organic–inorganic nanomaterials: from laboratory to market, Chem. Soc. Rev. 40 (2011) 696–753.
[30] P. Hammer, F.C. Dos Santos, B.M. Cerrutti, S.H. Pulcinelli, C. V. Santilli, Corrosion Resistant Coatings Based on Organic-Inorganic Hybrids Reinforced by Carbon Nanotubes, in: R.S. Razavi (Ed.), Recent Res. Corros. Eval. Prot., InTech, Rijeka, 2012: pp. 117–142.
[31] F.C. Dos Santos, S.V. Harb, M.J. Menu, V. Turq, S.H. Pulcinelli, C.V. Santilli, P. Hammer, On the structure of high performance anticorrosive PMMA-siloxane-silica hybrid coatings, RSC Adv. 5 (2015) 106754–106763.
[32] S. V. Harb, S.H. Pulcinelli, C. V. Santilli, K.M. Knowles, P. Hammer, A Comparative Study on Graphene Oxide and Carbon Nanotube Reinforcement

of PMMA-Siloxane-Silica Anticorrosive Coatings, ACS Appl. Mater. Interfaces. 8 (2016) 16339–16350.
[33] C. Sanchez, P. Belleville, M. Popall, L. Nicole, Applications of advanced hybrid organic-inorganic nanomaterials: from laboratory to market, Chem. Soc. Rev. 40 (2011) 696–753.
[34] P.A. Sorensen, S. Kiil, K. Dam-Johansen, C.E. Weinell, Anticorrosive coatings: A review, J. Coatings Technol. Res. 6 (2009) 135–176.
[35] A.A. Olajire, Recent advances on organic coating system technologies for corrosion protection of offshore metallic structures, J. Mol. Liq. 269 (2018) 572–606.
[36] G. Grundmeier, W. Schmidt, M. Stratmann, Corrosion Protection by organic coatings: electrochemical mechanism and novel methods of investigation, Electrochim. Acta. 45 (2000) 2512–2533.
[37] J.S. Gandhi, S. Singh, W.J. Van Ooij, P. Puomi, Evidence for formation of metallo-siloxane bonds by comparison of dip-coated and electrodeposited silane films, J. Adhes. Sci. Technol. 20 (2006) 1741–1768.
[38] P. Hammer, F.C. Dos Santos, B.M. Cerrutti, S.H. Pulcinelli, C.V. Santilli, Highly corrosion resistant siloxane-polymethyl methacrylate hybrid coatings, J. Sol-Gel Sci. Technol. 63 (2012) 266–274.
[39] S.V. Harb, B.M. Cerrutti, S.H. Pulcinelli, C.V. Santilli, P. Hammer, Siloxane–PMMA hybrid anti-corrosion coatings reinforced by lignin, Surf. Coatings Technol. 275 (2015) 9–16.
[40] S.V. Harb, F.C. Dos Santos, B.L. Caetano, S.H. Pulcinelli, C.V. Santilli, P. Hammer, Structural properties of cerium doped siloxane-PMMA hybrid coatings with high anticorrosive performance, RSC Adv. 5 (2015) 15414–15424.
[41] J. Mosa, N.C. Rosero-Navarro, M. Aparicio, Active corrosion inhibition of mild steel by environmentally-friendly Ce-doped organic-inorganic sol-gel coatings, RSC Adv. 6 (2016) 39577–39586.
[42] C. Duval-Terrié, L. Lebrun, Polymerization and Characterization of PMMA, J. Chem. Educ. 2 (2006) 443–446.
[43] C.J. Brinker, G.W. Scherer, Sol → gel → glass: I. Gelation and gel structure, J. Non. Cryst. Solids. 70 (1985) 301–322.
[44] C.J. Brinker, G.W. Scherer, Sol-Gel Science, The physics and chemistry of sol-gel processing, (1990) 462.
[45] R.F.A.O. Torrico, S.V. Harb, A. Trentin, M.C. Uvida, S.H. Pulcinelli, C.V. Santilli, P. Hammer, Structure and properties of epoxy-siloxane-silica nanocomposite coatings for corrosion protection, J. Colloid Interface Sci. 513 (2018) 617–628.
[46] M.E. Orazem, B. Tribollet, Electrochemical Impedance Spectroscopy, 2008.
[47] B. Hirschorn, M.E. Orazem, B. Tribollet, V. Vivier, I. Frateur, M. Musiani, Constant-Phase-Element Behavior Caused by Resistivity Distributions in Films, J. Electrochem. Soc. 157 (2010) C452–C457.
[48] Y.M. Chen, A.S. Nguyen, M.E. Orazem, B. Tribollet, N. Pébère, M. Musiani, V. Vivier, Identification of Resistivity Distributions in Dielectric Layers by Measurement Model Analysis of Impedance Spectroscopy, Electrochim. Acta. 219 (2016) 312–320.
[49] F. Brusciotti, D.V. Snihirova, H. Xue, M.F. Montemor, S.V. Lamaka, M.G.S. Ferreira, Hybrid epoxy-silane coatings for improved corrosion protection of Mg

alloy, Corros. Sci. 67 (2013) 82–90.
[50] A.S. Nguyen, M. Musiani, M.E. Orazem, N. Pébère, B. Tribollet, V. Vivier, Impedance analysis of the distributed resistivity of coatings in dry and wet conditions, Electrochim. Acta. 179 (2015) 452–459.
[51] L. Young, Anodic Oxide Films, Trans. Faraday Soc. 51 (1955) 1250–1260.
[52] G. Bouvet, D.D. Nguyen, S. Mallarino, S. Touzain, Analysis of the non-ideal capacitive behaviour for high impedance organic coatings, Prog. Org. Coatings. 77 (2014) 2045–2053.
[53] O.M. Magnussen, Corrosion Protection by Inhibition, in: A.J. Bard (Ed.), Encycl. Electrochem., Wiley VCH, Weinheim, 2007: pp. 435–459.
[54] A.J. Aldykewicz, H.S. Isaacs, A.J. Davenport, The Investigation of Cerium as a Cathodic Inhibitor for Aluminum-Copper Alloys, J. Electrochem. Soc. 142 (1995) 3342–3350.
[55] J. Gui, T.M. Devine, Influence of lithium on the corrosion of aluminum, Scr. Metall. 21 (1987) 853–857.
[56] P. Visser, Y. Gonzalez-Garcia, J.M.C. Mol, H. Terryn, Mechanism of Passive Layer Formation on AA2024-T3 from Alkaline Lithium Carbonate Solutions in the Presence of Sodium Chloride, J. Electrochem. Soc. 165 (2018) C60–C70.
[57] F.A. and L. Fedrizzi, Corrosion Inhibitors, in: R.A.E. Hughes, J.M.C. Mol, M.L. Zheludkevich (Eds.), Act. Prot. Coatings New-Generation Coatings Met., Springer Science+Business Media B.V, Dordrecht, 2016: pp. 59–84.
[58] V.S. Sastri, Corrosion Inhibitors: Principles and applications, John Wiley, Ottawa: ON, 1998.
[59] H.H. Uhlig, Corrosion and corrosion control : an introduction to corrosion science and engineering, 3. ed.-, John Wiley & Sons, Inc., New York, 1985.
[60] P.H. Suegama, V.H.V. Sarmento, M.F. Montemor, A. V. Benedetti, H.G. de Melo, I. V. Aoki, C. V. Santilli, Effect of cerium (IV) ions on the anticorrosion properties of siloxane-poly(methyl methacrylate) based film applied on tin coated steel, Electrochim. Acta. 55 (2010) 5100–5109.
[61] J. V. Nardeli, C.S. Fugivara, M. Taryba, E.R.P. Pinto, M.F. Montemor, A. V. Benedetti, Tannin: A natural corrosion inhibitor for aluminum alloys, Prog. Org. Coatings. 135 (2019) 368–381.
[62] P. Visser, K. Marcoen, G.F. Trindade, M.L. Abel, J.F. Watts, T. Hauffman, J.M.C. Mol, H. Terryn, The chemical throwing power of lithium-based inhibitors from organic coatings on AA2024-T3, Corros. Sci. 150 (2019) 194–206.
[63] M. Schem, T. Schmidt, J. Gerwann, M. Wittmar, M. Veith, G.E. Thompson, I.S. Molchan, T. Hashimoto, P. Skeldon, A.R. Phani, S. Santucci, M.L. Zheludkevich, CeO2-filled sol-gel coatings for corrosion protection of AA2024-T3 aluminium alloy, Corros. Sci. 51 (2009) 2304–2315.
[64] D. Snihirova, S. V. Lamaka, M.F. Montemor, “SMART” protective ability of water based epoxy coatings loaded with CaCO3microbeads impregnated with corrosion inhibitors applied on AA2024 substrates, Electrochim. Acta. 83 (2012) 439–447.
[65] C.D. Dieleman, P.J. Denissen, S.J. Garcia, Long-Term Active Corrosion Protection of Damaged Coated-AA2024-T3 by Embedded Electrospun Inhibiting Nanonetworks, Adv. Mater. Interfaces. 5 (2018) 1–10.
[66] L.B. Coelho, D. Cossement, M.G. Olivier, Benzotriazole and cerium chloride as

corrosion inhibitors for AA2024-T3: An EIS investigation supported by SVET and ToF-SIMS analysis, Corros. Sci. 130 (2018) 177–189.
[67] M. Bethencourt, F.J. Botana, J.J. Calvino, M. Marcos, M.A. Rodriguez-Chacon, Lanthanide compounds as environmentally-friendly corrosion inhibitors of aluminium alloys: A review, Corros. Sci. 40 (1998) 1803–1819.
[68] K.A. Yasakau, M.L. Zheludkevich, O. V. Karavai, M.G.S. Ferreira, Influence of inhibitor addition on the corrosion protection performance of sol-gel coatings on AA2024, Prog. Org. Coatings. 63 (2008) 352–361.
[69] U. Tiringer, A. Duran, Y. Castro, I. Milosev, Self-healing effect of hybrid sol-gel coatings based on GPTMS, TEOS, SiO2 nanoparticles and Ce(NO3)3 applied on aluminum alloy 7075-T6, J. OfThe Electrochem. Soc. 165 (2018) C312–C225.
[70] M. Druart, I. Recloux, T.T. Thai, S. Ershov, R. Snyders, M. Olivier, Impact of the addition of cerium salts (Ce(III) and Ce(IV)) on formation and ageing of a silica sol-gel layer, Surf. Coat. Technol. 304 (2016) 40–50.
[71] L.M. Calado, M.G. Taryba, M.J. Carmezim, M.F. Montemor, Self-healing ceria-modified coating for corrosion protection of AZ31 magnesium alloy, Corros. Sci. 142 (2018) 12–21.
[72] P. Yu, S.A. Hayes, T.J. O'Keefe, M.J. O'Keefe, J.O. Stoffer, The phase stability of cerium species in aqueous systems, J. Electrochem. Soc. 153 (2006) 74–79.
[73] P. Visser, Y. Liu, H. Terryn, J.M.C. Mol, Lithium salts as leachable corrosion inhibitors and potential replacement for hexavalent chromium in organic coatings for the protection of aluminum alloys, J. Coatings Technol. Res. 13 (2016) 557–566.
[74] P. Visser, H. Terryn, J.M.C. Mol, On the importance of irreversibility of corrosion inhibitors for active coating protection of AA2024-T3, Corros. Sci. 140 (2018) 272–285.
[75] P. Visser, H. Terryn, J.M.C. Mol, Active corrosion protection of various aluminium alloys by lithium-leaching coatings, Surf. Interface Anal. 51 (2019) 1–12.
[76] K. Marcoen, P. Visser, G.F. Trindade, M.L. Abel, J.F. Watts, J.M.C. Mol, H. Terryn, T. Hauffman, Compositional study of a corrosion protective layer formed by leachable lithium salts in a coating defect on AA2024-T3 aluminium alloys, Prog. Org. Coatings. 119 (2018) 65–75.
[77] A. Boag, R.J. Taylor, T.H. Muster, N. Goodman, D. McCulloch, C. Ryan, B. Rout, D. Jamieson, A.E. Hughes, Stable pit formation on AA2024-T3 in a NaCl environment, Corros. Sci. 52 (2010) 90–103.
[78] P. Visser, A. Lutz, J.M.C. Mol, H. Terryn, Study of the formation of a protective layer in a defect from lithium-leaching organic coatings, Prog. Org. Coatings. 99 (2016) 80–90.
[79] R.G. Buchheit, M.D. Bode, G.E. Stoner, Corrosion-Resistant, Chromate-Free Talc Coatings for Aluminum, Corros. 50 (1993) 205–214.
[80] C.M. Rangel, M.A. Travassos, Li-based conversion coatings on aluminium: An electrochemical study of coating formation and growth, Surf. Coatings Technol. 200 (2006) 5823–5828.
[81] A.T. Tran, F. Huet, K. Ngo, P. Rousseau, Artefacts in electrochemical impedance measurement in electrolytic solutions due to the reference electrode, Electrochim. Acta. 56 (2011) 8034–8039.

[82] G. Guinier, C. Fournet, C.B. Walker, K.L. Yudovitch, Small Angle Scattering of Xrays, Freeman, New York, 1955.
[83] B. Hammouda, A new Guinier-Porod model, J. Appl. Crystallogr. 43 (2010) 716–719.
[84] C. V Santilli, V.H. V Sarmento, K. Dahmouche, S.H. Pulcinelli, A.F. Craievich, Effects of Synthesis Conditions on the Nanostructure of Hybrid Sols Produced by the Hydrolytic Condensation of (3-Methacryloxypropyl)trimethoxysilane, J. Phys. Chem. C. 113 (2009) 14708–14714.
[85] G. Beaucage, T.A. Ulibarri, E.P. Black, D.W. Schaefer, Multiple Size Scale Structures in Silica-Siloxane Composites Studied by Small-Angle Scattering, in: J.E. Mark, C.Y.C. Lee, P.A. Bianconi (Eds.), Hybrid Org. Compos., ACS sympos, American Chemical Society, Washington, DC, 1995: pp. 97–111.
[86] F.W. Billmeyer Jr, Radical chain (addition) polymerization, in: Textb. Polym. Sci., Wiley-Interscience, Singapore, 1984: pp. 49–77.
[87] H.A. Willis, V.J.I. Zichy, P.J. Hendra, The laser-Raman and infrared spectra of poly(methyl methacrylate), Polymer (Guildf). 10 (1969) 737–746.
[88] H.G.M. Edwards, K.S. Johal, A.F. Johnson, FT-Raman spectroscopic monitoring of the group-transfer polymerisation of methyl methacrylate, Vib. Spectrosc. 41 (2006) 160–169.
[89] C.J.T. Landry, B.K. Coltrain, J.A. Wesson, N. Zumbulyadis, J.L. Lippert, In situ polymerization of tetraethoxysilane in polymers: chemical nature of the interactions, Polymer (Guildf). 33 (1992) 1496–1506.
[90] G. delC. Pizarro, O.G. Marambio, M. Jeria-Orell, C.M. González-Henríquez, M. Sarabia-Vallejos, K.E. Geckeler, Effect of annealing and UV-radiation time over micropore architecture of self-assembled block copolymer thin film, Express Polym. Lett. 9 (2015) 525–535.
[91] L.E. Manring, Thermal Degradation of Poly(methyl methacrylate). 2. Vinyl-Terminated Polymer, Macromolecules. 22 (1989) 2673–2677.
[92] T. Kashiwagi, A. Inaba, J.E. Brown, K. Hatada, T. Kitayama, E. Masuda, Effects of Weak Linkages on the Thermal and Oxidative Degradation of Poly(methyl methacrylates), Macromolecules. 19 (1986) 2160–2168.
[93] A.V. Naumkin, A. Kraut-Vass, S.W. Gaarenstroom, C.J. Powell, NIST X-ray Photoelectron Spectroscopy Database, NIST Stand. Ref. Database 20. (2012).
[94] Z. Sassi, J.C. Bureau, A. Bakkali, Spectroscopic study of TMOS-TMSM-MMA gels Previously identification of the networks inside the hybrid material, Vib. Spectrosc. 28 (2002) 299–318.
[95] S. V. Lamaka, H.B. Xue, N.N.A.H. Meis, A.C.C. Esteves, M.G.S. Ferreira, Fault-tolerant hybrid epoxy-silane coating for corrosion protection of magnesium alloy AZ31, Prog. Org. Coatings. 80 (2015) 98–105.
[96] R. Suleiman, H. Dafalla, B. El Ali, Novel hybrid epoxy silicone materials as efficient anticorrosive coatings for mild steel, RSC Adv. 5 (2015) 39155–39167.
[97] A.H. Najafabadi, R. Mozaffarinia, H. Rahimi, R.S. Razavi, E. Paimozd, Sol-gel processing of hybrid nanocomposite protective coatings using experimental design, Prog. Org. Coatings. 76 (2013) 293–301.
[98] G.P. Bierwagen, L. He, J. Li, L. Ellingson, D.E. Tallman, Studies of a new accelerated evaluation method for coating corrosion resistance - thermal cycling testing, Prog. Org. Coatings. 39 (2000) 67–78.

[99] S. Ammar, K. Ramesh, B. Vengadaesvaran, S. Ramesh, A.K. Arof, A novel coating material that uses nano-sized SiO2particles to intensify hydrophobicity and corrosion protection properties, Electrochim. Acta. 220 (2016) 417–426.
[100] M. Echeverría, C.M. Abreu, K. Lau, C.A. Echeverría, Viability of epoxy-siloxane hybrid coatings for preventing steel corrosion, Prog. Org. Coatings. 92 (2016) 29–43.
[101] S. Qiu, C. Chen, W. Zheng, W. Li, H. Zhao, L. Wang, Long-term corrosion protection of mild steel by epoxy coating containing self-doped polyaniline nanofiber, Synth. Met. 229 (2017) 39–46.
[102] M. Abdolah Zadeh, S. Van Der Zwaag, S.J. Garcia, Adhesion and Long-Term Barrier Restoration of Intrinsic Self-Healing Hybrid Sol-Gel Coatings, ACS Appl. Mater. Interfaces. 8 (2016) 4126–4136.
[103] M.C.L. de Oliveira, R.A. Antunes, I. Costa, Effect of the NCO/OH molar ratio on the physical aging and on the electrochemical behavior of polyurethane-urea hybrid coatings, Int. J. Electrochem. Sci. 8 (2013) 4679–4689.
[104] S. Ashhari, A.A. Sarabi, S.M. Kasiriha, D. Zaarei, Aliphatic Polyurethane-Montmorillonite Nanocomposite Coatings: Preparation, Characterization, and Anticorrosive Properties, J. Appl. Polym. Sci. 119 (2011) 523–529.
[105] D.M. Brasher, A.H. Kingsbury, Electrical Measurements in the Study of Immersed Paint Coatings on Metal. 1. Comparison between Capacitance and Gravimetric Methods of Estimating Water-Uptake, J. Appl. Chem. 4 (1954) 62–72.
[106] M.E. Orazem, B. Tribollet, Electrochemical Impedance Spectroscopy, John Wiley & Sons, New Jersey, 2008.
[107] M.E. Orazem, I. Frateur, B. Tribollet, V. Vivier, S. Marcelin, N. Pebere, A.L. Bunge, E.A. White, D.P. Riemer, M. Musiani, Dielectric properties of materials showing constant-phase-element (CPE) impedance response, J. Electrochem. Soc. 160 (2013) 215–225.
[108] B.R. Hinderliter, S.G. Croll, D.E. Tallman, Q. Su, G.P. Bierwagen, Interpretation of EIS data from accelerated exposure of coated metals based on modeling of coating physical properties, Electrochim. Acta. 51 (2006) 4505–4515.
[109] S. Ammar, K. Ramesh, B. Vengadaesvaran, S. Ramesh, A.K. Arof, Amelioration of anticorrosion and hydrophobic properties of epoxy/PDMS composite coatings containing nano ZnO particles, Prog. Org. Coatings. 92 (2016) 54–65.
[110] M. Musiani, M.E. Orazem, N. Pébère, B. Tribollet, V. Vivier, Determination of resistivity profiles in anti-corrosion coatings from constant-phase-element parameters, Prog. Org. Coatings. 77 (2014) 2076–2083.
[111] C. Moreno, S. Hernández, J.J. Santana, J. González-Guzmán, R.M. Souto, S. González, Characterization of water uptake by organic coatings used for the corrosion protection of steel as determined from capacitance measurements, Int. J. Electrochem. Sci. 7 (2012) 8444–8457.
[112] S. Amand, M. Musiani, M.E. Orazem, N. Pébère, B. Tribollet, V. Vivier, Constant-phase-element behavior caused by inhomogeneous water uptake in anti-corrosion coatings, Electrochim. Acta. 87 (2013) 693–700.
[113] V. Nguyen, Anh Son Musiani, Marco Orazem, Mark E. Pébère, Nadine Tribollet, Bernard Vivier, Impedance study of the influence of chromates on the properties of waterborne coatings deposited on 2024 aluminium alloy, Corros. Sci. 109

(2016) 174–181.
[114] Y.L. Spirin, A.A. Arest-Yakubovich, D.K. Polyakov, A.R. Gantmakher, S.S. Medvedev, Polymerization Catalyzed by Lithium and Lithium Alkyl, J. Polym. Sci. 58 (1962) 1181–1189.
[115] A.L.B. Maçon, M. Jacquemin, S.J. Page, S. Li, S. Bertazzo, M.M. Stevens, J. V. Hanna, J.R. Jones, Lithium-silicate sol-gel bioactive glass and the effect of lithium precursor on structure-property relationships, J. Sol-Gel Sci. Technol. 81 (2017) 84–94.
[116] S. Ammar, K. Ramesh, B. Vengadaesvaran, S. Ramesh, A.K. Arof, Formulation and characterization of hybrid polymeric/ZnO nanocomposite coatings with remarkable anti-corrosion and hydrophobic characteristics, J. Coatings Technol. Res. 13 (2016) 921–930.
[117] M.L. Zheludkevich, S.K. Poznyak, L.M. Rodrigues, D. Raps, T. Hack, L.F. Dick, T. Nunes, M.G.S. Ferreira, Active protection coatings with layered double hydroxide nanocontainers of corrosion inhibitor, Corros. Sci. 52 (2010) 602–611.
[118] M. Frenkel, A. Glasner, S. Sarig, Crystal modification of freshly precipitated aluminum hydroxide by lithium ion intercalation, J. Phys. Chem. 84 (1980) 507–510.
[119] A.E. Hughes, A. Trinchi, F.F. Chen, Y.S. Yang, I.S. Cole, S. Sellaiyan, J. Carr, P.D. Lee, G.E. Thompson, T.Q. Xiao, The application of multiscale quasi 4D CT to the study of SrCrO4 distributions and the development of porous networks in epoxy-based primer coatings, Prog. Org. Coatings. 77 (2014) 1946–1956.
[120] V.P. Isupov, Intercalation Compounds of Aluminum Hydroxide, J. Struct. Chem. 40 (1999) 672–682.
[121] D. Snihirova, S. V. Lamaka, P. Taheri, J.M.C. Mol, M.F. Montemor, Comparison of the synergistic effects of inhibitor mixtures tailored for enhanced corrosion protection of bare and coated AA2024-T3, Surf. Coatings Technol. 303 (2016) 342–351.
[122] I. Danaee, E. Darmiani, G.R. Rashed, D. Zaarei, Self-healing and anticorrosive properties of Ce(III)/Ce(IV) in nanoclay-epoxy coatings, Iran. Polym. J. 23 (2014) 891–898.
[123] K.A. Yasakau, J. Carneiro, M.L. Zheludkevich, M.G.S. Ferreira, Influence of sol-gel process parameters on the protection properties of sol-gel coatings applied on AA2024, Surf. Coatings Technol. 246 (2014) 6–16.
[124] M.F. Montemor, R. Pinto, M.G.S. Ferreira, Chemical composition and corrosion protection of silane films modified with CeO2 nanoparticles, Electrochim. Acta. 54 (2009) 5179–5189.
[125] T. Wang, L. Tan, C. Ding, M. Wang, J. Xu, J. Fu, Redox-triggered controlled release systems-based bi-layered nanocomposite coating with synergistic self-healing property, J. Mater. Chem. A. 5 (2017) 1756–1768.
[126] Z. Assefa, R.G. Haire, D.L. Caulder, D.K. Shuh, Correlation of the oxidation state of cerium in sol-gel glasses as a function of thermal treatment via optical spectroscopy and XANES studies, Spectrochim. Acta - Part A Mol. Biomol. Spectrosc. 60 (2004) 1873–1881.
[127] M.G. Schiavetto, P. Hammer, C.V. Santilli, S.H. Pulcinelli, F.C. dos Santos, A.V. Benedetti, Improvement of the corrosion resistance of polysiloxane hybrid coatings by cerium doping, J. Non. Cryst. Solids. 356 (2010) 2606–2612.

[128] R.F. Storey, L.J. Goff, Ceric Ion Initiation of Vinylidene Chloride from Poly(vinyl alcohol), Macromolecules. 22 (1989) 1058–1064.
[129] H. Arslan, B. Hazer, Ceric ion initiation of methyl methacrylate using polytetrahydrofuran diol and polycaprolactone diol, Eur. Polym. J. 35 (1999) 1451–1455.
[130] T. Ozturk, I. Cakmak, Synthesis of block copolymers via redox polymerization process: A critical review, Iran. Polym. J. (English Ed. 16 (2007) 561–581.